AMERICAN UNIVERSITY OF BEIRUT

DESIGN OF A MICROWAVE SENSOR FOR NON-INVASIVE BLOOD GLUCOSE MONITORING

by
MOUSSA SEMAAN BTEICH

A thesis
submitted in partial fulfillment of the requirements
for the degree of Master of Engineering
to the Department of Electrical and Computer Engineering
of the Maroun Semaan Faculty of Engineering and Architecture
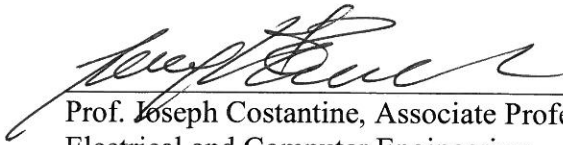at the American University of Beirut

Beirut, Lebanon
April 2019

AMERICAN UNIVERSITY OF BEIRUT

DESIGN OF A MICROWAVE SENSOR FOR NON-INVASIVE BLOOD GLUCOSE MONITORING
by
MOUSSA SEMAAN BTEICH

Approved by:

_____   Advisor
Prof. Joseph Costantine, Associate Professor
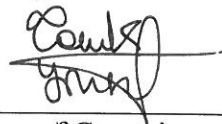Electrical and Computer Engineering

_____   Co-Advisor
Prof. Rouwaida Kanj, Assistant Professor
Electrical and Computer Engineering

_____   Member of Committee
Prof. Zaher Dawy, Professor
Electrical and Computer Engineering

_____   Member of Committee
Prof. Youssef Tawk, Assistant Professor
Electrical and Computer Engineering

_____   Member of Committee
Prof. Assaad Eid, Associate Professor
Anatomy, Cell Biology and Physiological Sciences

_____   Member of Committee
Prof. Ali Ramadan, Assistant Professor
Electrical Engineering,
Fahad Bin Sultan University, Tabuk, KSA

Date of thesis defense: April 23, 2019

AMERICAN UNIVERSITY OF BEIRUT

THESIS, DISSERTATION, PROJECT RELEASE FORM

Student Name: Bteich Moussa Semaan

	Last	First
Middle		

☑ Master's Thesis ⬤ Master's Project ⬤ Doctoral Dissertation

☐   I authorize the American University of Beirut to: (a) reproduce hard or electronic copies of my thesis, dissertation, or project; (b) include such copies in the archives and digital repositories of the University; and (c) make freely available such copies to third parties for research or educational purposes.

☑   I authorize the American University of Beirut, to: (a) reproduce hard or electronic copies of it; (b) include such copies in the archives and digital repositories of the University; and (c) make freely available such copies to third parties for research or educational purposes after:
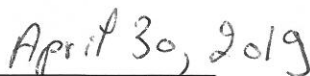
      One ---- year from the date of submission of my thesis, dissertation, or project.
      Two ---- years from the date of submission of my thesis, dissertation, or project.
      Three ---- years from the date of submission of my thesis, dissertation, or project.

[signature]   April 30, 2019

Signature   Date

ACKNOWLEDGMENTS

I would like to genuinely acknowledge my thesis advisors Dr. Joseph Costantine and Dr. Rouwaida Kanj for their support, advice, and encouragement to complete my thesis. I recognize Dr. Joseph for helping me to improve my research skills during my work on this thesis. I thank Dr. Rouwaida Kanj for her contribution to the data analytic part.

I would like to thank Dr. Assad Eid, Dr. Ali Ramadan and Dr. Youssef Tawk for their continuous input and for being on my thesis committee. I would also like to thank Dr. Zaher Dawy for being on my thesis committee.

I would like to thank my colleagues for their help and support during my research work.

Finally, I would like to thank my parents, brother, sister, and friends for supporting and encouraging me during my studies.

AN ABSTRACT OF THE THESIS OF

Moussa Semaan Bteich   for   <u>Master of Engineering</u>
                                             <u>Major</u>: Electrical and Computer Engineering

Title: <u>Design of a Microwave Sensor for Non-Invasive Blood Glucose Monitoring</u>

Diabetes is one of the most prevalent chronic diseases. The exponential rate of increase in the number of diabetics urged researchers to search for new methods of measuring blood glucose continuously and non-invasively. The ability of microwave devices to extract the electrical parameters of material accurately and without direct contact, makes them ideal for measuring glucose concentrations non-invasively. Therefore, since the past decade, a lot of research work has focused on designing microwave sensors that are capable of sensing the variation of glucose in blood. Although some of the proposed devices have shown good sensitivity, however none of them is accurate enough to replace the currently used glucometers.

This thesis addresses the design of non-invasive glucose sensors by relying on microwave based components. Hence, the design of various types of radio frequency (RF) circuits is presented to tackle this challenge. The behavior of the proposed RF circuits as glucose sensing systems is tested using simulation in addition to in-vitro, ex-vivo and in-vivo studies. A good correlation between the scattering parameters of proposed sensors and the variations in glucose levels is attained. Several regression models are also developed and applied on the collected data, where a selection of the optimal model with the least prediction error is identified. Examined results using the Clarke error grid demonstrate that 100% of the predicted glucose levels lie within the clinically acceptable regions for the various proposed sensors.

CONTENTS

7. SIMULATION AND MEASUREMENT OF THE PROPOSED EM-BASED GLUCOSE SENSORS

8. DEVELOPMENT OF A REGRESSION MODEL

ILLUSTRATIONS

xiii

xiv

TABLES

CHAPTER 1

INTRODUCTION

1.1. Background

During the past few decades, changes in lifestyle and nutrition made diabetes one of the most prominent diseases among chronic conditions. By 2014, the number of people diagnosed with diabetes reached 422 million worldwide. This number is expected to increase dramatically in the upcoming years due to the exponential growth of this disease [1]. In fact, diabetes is considered one of the most common metabolic diseases. There are two main types of diabetes: type 1 and type 2, with type 1 being the most serious condition. For patients with type 1 diabetes, the auto-immune system destroys the cells that produce insulin. Consequently, the production of insulin decreases or stops completely and hence the blood glucose level (BGL) increases. Only 10% of diabetics are diagnosed with type 1. Around 90% are diagnosed with type 2 diabetes, and they suffer from a slow production rate of insulin in the body, which in turn decreases the effects of insulin resulting in chronic hyperglycemia [2].

Although the causes of these two categories are different, however their consequences are dangerous and much alike. In fact, advanced stages of both types of diabetes are associated with several complications such as kidney failure, blindness and limb amputation. In addition, diabetes increases the risk of stroke and coronary heart disease. In 2015, around 1.6 million deaths were caused directly by this condition. An additional 3 million deaths were caused by the complications of the disease [1].

For treatment, accurate determination of BGL is a necessity. Currently, BGL is measured using a glucometer. Although this device is highly accurate, however, it is invasive. In fact, the patient has to prick a finger each time a glucose measurement is required. This process is painful for diabetics especially with the need to measure glucose levels several times during the day. In the long term, this method increases the risk of infection and may damage the underlying tissue. Additionally, this measurement technique does not provide continuous monitoring, which can result in missing serious hypo/hyper-glycemic incidents that can happen between two measurements [3].

In the past decade, several new blood glucose measurement techniques have been investigated, which fall within one of the two categories: minimally invasive and non-invasive. In [4] and [5], a review of the most popular non-invasive techniques is presented. This review includes infrared spectroscopy, excreted physiological fluid analysis, electrodes, microcalorimetry and optical sensors. Additionally, minimally invasive methods for BGL monitoring such as sonophoresis and iontophoresis aim to extract the level of glucose from the skin [3]. All the proposed sensors have failed to replace the current measurement method as they lacked accuracy. More recently, alternative solutions are developed using electromagnetic measurement techniques, as a mean to provide continuous and non-invasive monitoring of BGLs. These methods rely on coupling EM waves on precise spots of the human body. The reflected waves are collected back and monitored, as they include information concerning the electrical properties of the underlying biological layers. Any variations in the collected waves

directly relates to parameters of blood. This information can be used to provide non-invasive and continuous monitoring of BGLs [6].

The ability of EM-based devices to extract parameters accurately, without perturbing the MUT, makes them ideal for measurements that require no direct contact with the material. The robustness and accuracy of these devices have encouraged researchers to investigate the possibility of designing microwave sensors for biomedical applications. Consequently, multiple wearable devices are developed that are capable of monitoring cardiac and respiratory activities [7], sensing bodies' abnormalities and disease prediction [8][9].

1.2. Project Motivation

In this research, we propose the design of three microwave sensors to detect variations in BG. These sensors are designed and tested in several in vivo and in vitro studies. A comparative study is also established to associate the performance of the different devices. A regression model is finally built in the aim of predicting glucose levels.

1.3. Thesis Structure

This thesis is divided into eight chapters. Chapter one includes an introduction. Chapter two provides a literature review that presents the most recent research work on non-invasive glucose monitoring. Chapter three discusses the electrical properties of different human tissues and the corresponding safe absorption rates of electromagnetic

(EM) energy. Chapter four presents a theoretical background on the electrical properties of lossy material. Chapter five discusses material characterization techniques that are developed in literature. Chapter six presents the proposed sensors. Chapter seven discusses all the conducted in vivo and in vitro studies. Chapter eight presents the established regression model. Chapter nine concludes this work and presents future research steps.

CHAPTER 2

LITERATURE REVIEW

2.1. Introduction

Throughout the last decade, research effort has focused on proposing microwave devices that can be employed for the monitoring of blood glucose concentrations in a continuous and non-invasive manner. These approaches include EM based waveguides, antennas and resonators operating at different frequencies. In the following, a literature review is provided. Topics associated to finding a relation between BGL and the electrical parameters, in addition to investigating the sensitivity of several microwave devices in sensing the BGL are covered in this section.

2.2. Three Dimensional Measurements

2.2.1. Waveguides

Using the setup in Fig. 1, a correlation between BGL and the electrical properties of tissues is presented in [10] and [11]. This relation is generated based on the fact that the relative permittivity of blood is directly related to the concentration of glucose. In these experiments, electromagnetic waves operating at 30 GHz are incident on body tissue. By monitoring the reflected waves from the tissue, it is shown that the dielectric constant of blood is altered for various BGLs. The variation in the dielectric constant are noted as a shift in frequency operation of the reflection coefficient.
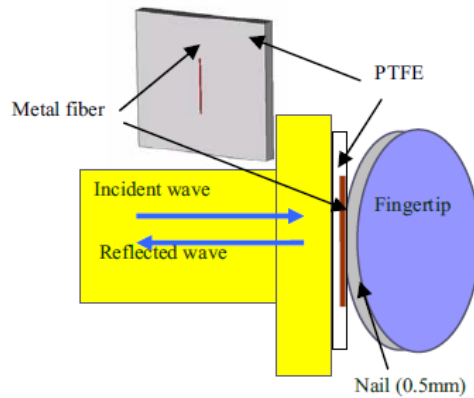
Figure 1: MMW measurement setup [10].

Two rectangular waveguides operating between 50 – 75 GHz are designed and tested in [12] using water-salt-glucose solutions as shown in Fig. 2. Glucose concentrations as small as 0.025 (wt%) are detected with an accuracy of 0.22 dB per wt%. The sensitivity of the system varies for different frequencies, and the best results are reached at two different bands between 59-64 GHz and between 69-73 GHz.
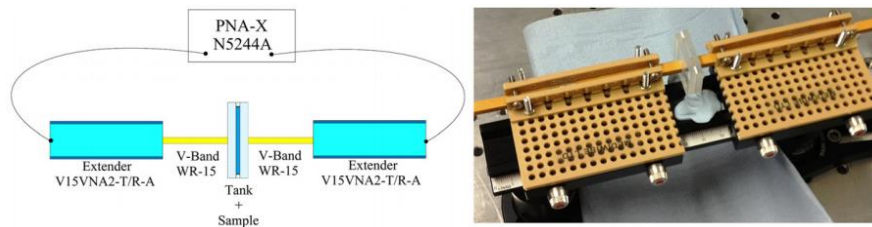
Figure 2: Proposed waveguides and measurement setup [12].

Real-time direct correlative measurements of the blood glucose concentration is performed using commercial blood test strips and millimeter-wave absorption for several injections of glucose, insulin, and saline in a live anesthetized animal [13]. The results of this work (Fig. 3) show an increase in the wave transmission after glucose injection, and a decrease in transmission after insulin injection. The relatively slow time

for the observed changes (10-15 minutes for glucose and 20-40 minutes for insulin)

correlates well with the expected speed of glucose and insulin metabolism. The lack of

significant changes in MMW transmission upon injection of saline indicates the

selectivity of mm-wave absorption to the tissue concentration of glucose.
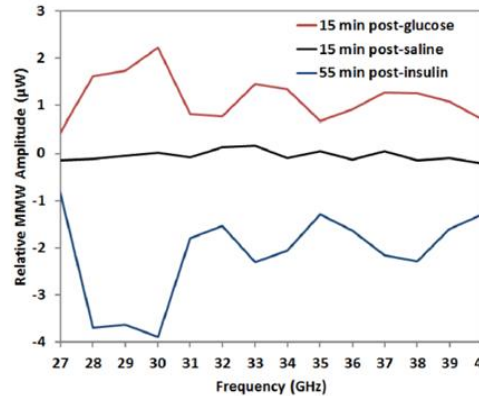
Figure 3: Transmission variations with time [13].

2.2.2. Antennas

A device is developed in which two antennas operating within the V-band are

placed around a pig's ears as shown in Fig. 4 [14]. Transmission and reflection

parameters are measured using a Vector Network Analyzer (VNA). The frequency

range of interest is between 58.5 GHz and 61.5 GHz. It is reported that the best results

are obtained when the antennas are closest to the tissues and are placed in an area rich

with veins. Furthermore, results demonstrate that an increase in glucose concentration

produces an increase in transmission at specific frequencies.

Following the integration of temperature and motion sensors, the patch is tested

using a water-glucose phantoms. The proposed system is able to detect changes in

7

glucose as low as 24 mg/dl. Furthermore, the system is tested on 10 healthy male subjects in [15]. These experiments verified its ability to successfully detect glucose spikes.

Figure 4: Tx and Rx antennas placed around pig's ear [14].

2.2.3. Resonators

The use of split ring resonators for glucose monitoring is examined in [16]. The system consists of two rings operating at 1.4 GHz as shown in Fig. 5. One ring is used for sensing and is placed at close proximity to the skin. The second one is placed far away and is considered as a reference to regulate the temperature effect. Both in-vitro and in-vivo measurements are carried out on one healthy patient and the results reached are comparable to those attained by the commercial glucometer. Furthermore, the proposed sensor is verified to be extremely selective, as it offers high sensitivity to glucose variations, limited sensitivity to other sugars and no sensitivity to vitamins [17]. The device is then clinically tested on 24 volunteers. Promising results are reached as 210 of 214 data points lay in the clinically acceptable regions [18].
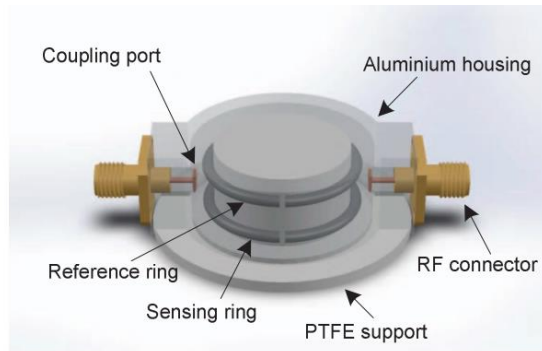
Figure 5: Double ring resonators system [16].

2.3. Planar Microwave Circuits

Planar circuits are also discussed in the literature. These structures offer a considerable reduction in size compared to the previously discussed three dimensional systems.

2.3.1. Antennas

One suggested system for planar circuits consists of implementing microstrip antennas as in [19], [20]. Several types of planar antennas including spirals, serpentines and dipoles are designed and tested in order to assess their ability to sense variations in glucose levels. In one embodiment, the reflection coefficient of the proposed antennas is monitored by placing the device near several glucose/water solutions of different concentrations. This experiment proved the ability of the antennas to sense variations in glucose concentration interpreted as shifts in the resonance frequency within the reflection coefficient. It is also reported that the dipole outclassed the remaining types of antennas. In another embodiment, the suggested device is mounted on the hand of a

diabetic patient and the volunteer's glucose levels are monitored as shown in Fig. 6. A good correlation is noted between the resonance frequency of the antenna and the reference BGLs measured with a traditional glucometer. A sensitivity of 1 MHz per 14.62mg/dl is also reported. Another observation made relates to the high dependency of the antenna's response on the biological variables of each subject such as metabolism, skin color, BMI and other elements.
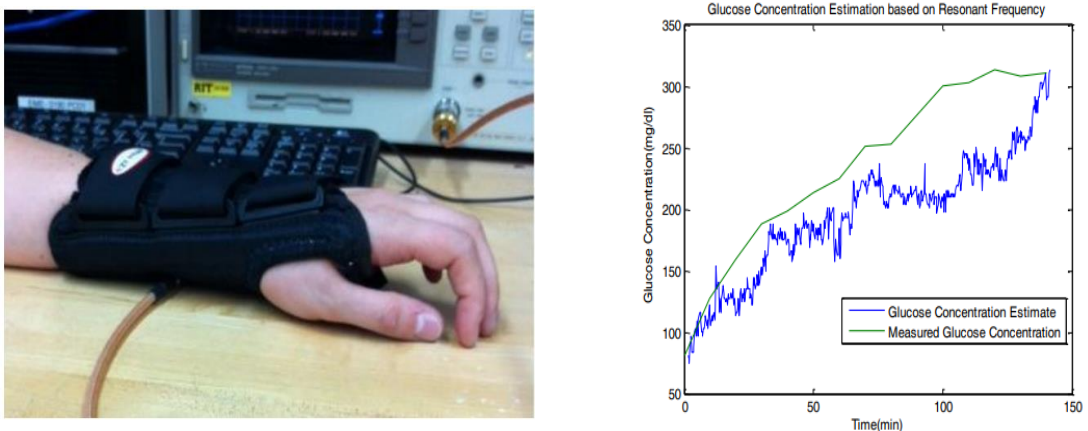
Figure 6: a) Antenna wrapped around subject's hand, and b) reference and estimated glucose variations with time [20].

The design of two ultra-wideband slot antennas of bandwidth equal to 12.5 GHz is also considered in [21]. The proposed sensing structures are envisioned to be placed around human's earlobe to continuously monitor BGLs. Testing the suggested antennas on glucose-water phantoms showed a linear correlation between the antenna parameters and various glucose levels. Note that the range considered for glucose concentrations is quite high (0-4000 mg/dl).

2.3.2. Resonators

A spiral sensor is presented in [22] to determine the BGL non-invasively (Fig. 7). In this research study, the relative permittivity of blood is investigated at different frequencies between 0 and 2 GHz. One volunteer performed a soda test by fasting for over eight hours before placing the device on his wrist. Then, the subject consumed a sugared soft drink. Results show that variations in glucose levels caused shifts in the resonance frequency of the sensor (Fig. 8). The fact that the shifts in frequency are not linear over the whole range implies that some frequencies may be more sensitive to the changes in BGL.

Another research is performed on the spiral sensor in [23]. In this experiment, the concentration of sugar in water is varied by adding sugar into the solution. Results of this work prove that the permittivity of the water decreases while adding sugar as displayed in Fig. 8.

Figure 7: Spiral resonator sensor [22].
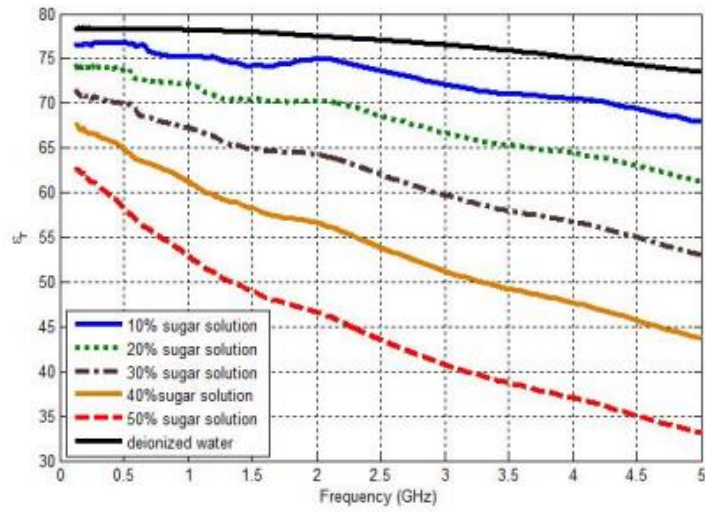
Figure 8: Relation between permittivity and glucose concentrations in function of frequency [23].

A half-wavelength resonator operating at 2 GHz is designed in [24] to sense the changes of glucose levels in water as shown in Fig. 9. By varying the concentrations of glucose from 0 to 300 mg/dl, the magnitude and phase of the reflection and transmission coefficients are recorded.
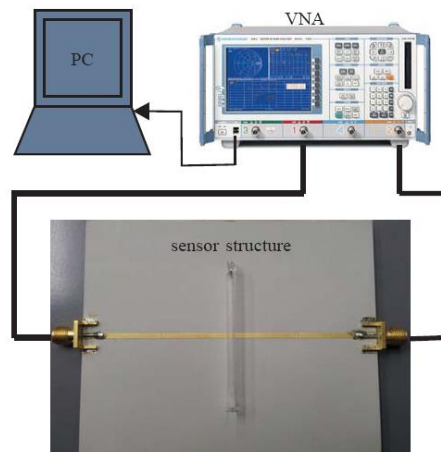
Figure 9: Sensor structure embedded in the measurement setup [24].

Fig. 10 presents the magnitude and phase of the S21 parameter for the various concentrations of glucose. It is clear that the proposed structure is capable of detecting changes in the concentrations of glucose with an accuracy in the range of 50 mg/dl.
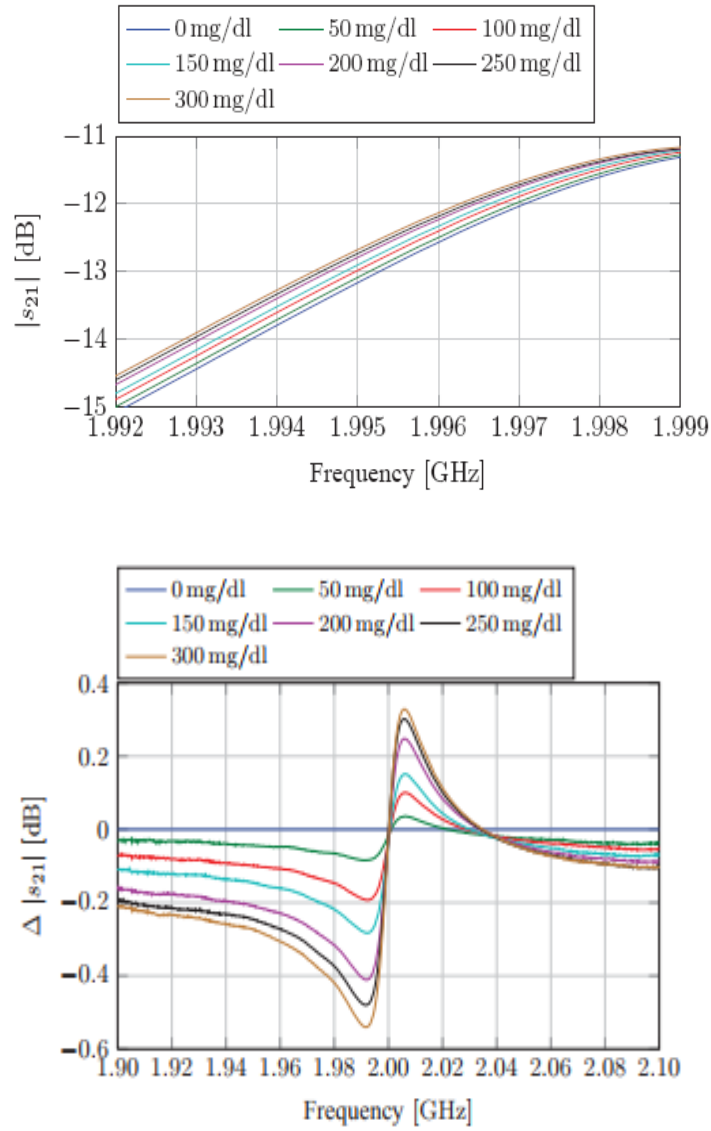
Figure 10: S21 magnitude and phase responses for different glucose concentrations [24].

13

2.3.3. Filters

A planar BPF is also proposed and is illustrated in Fig. 11 [25]. Parameters of this structure such as resonant frequency and insertion loss are sensitive to the dielectric constant of the superstrate. When contacted by a thumb, results show that the response of the sensor changes.

Figure 11: Prototype of the designed filter loaded by a human thumb [25].

An experiment is conducted on the suggested sensor in which a volunteer consumes sugar water with a high concentrations of glucose. Measurements show that the permittivity of blood decreased continuously, which causes an increase in the resonant frequency of the BPF (Fig. 12). After 600 seconds, a stable state is detected. It is important to indicate that a linear operation is reported between 1.5 and 2 GHz.
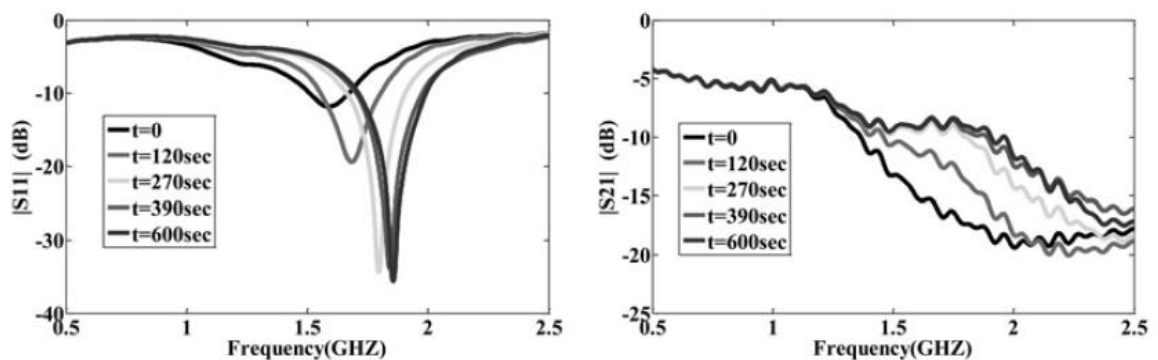
Figure 12: S11 and S21 parameters variations with time [25].

CHAPTER 3

THE CORRELATION BETWEEN MICROWAVE AND BIOLOGICAL TISSUES

3.1 Introduction

This chapter includes two main sections that illustrate the relation between electromagnetic waves and human science. The first section addresses the safe levels of human exposure to EM energy. The second section discusses the electrical properties of the biological tissues, and the response of these tissues when excited with EM energy.

3.2. Human Safety from Exposure to Electromagnetic Waves

From a physiological point of view, concerns about the exposure of the human body to electromagnetic waves have risen recently due to the abundance of such waves within the ambient environment. In fact, nowadays, multiple EM sources such as cell phones, routers and satellites are widely used. As a result, the human body is exposed abundantly and more frequently to such radiation. In fact, several standards and protocols are developed, by many researchers and health experts to limit as well as control the exposure of the human body to EM waves.

The safe exposure standards are set by the Institute of Electrical and Electronics Engineers (IEEE). According to the standard 'C95.1-2005', the specific absorption rate is defined as "the time derivative of the incremental energy (dW) absorbed by an incremental mass (dm) contained in a volume element (dV) of given density (ρ)" as demonstrated in Eq. 1 [26].

$$\text{SAR} = \frac{d}{dt}\left(\frac{dW}{\rho dV}\right) (W/Kg) \ (1)$$

Also, a relation between the absorption rate and the electric field at a specific

point is presented in Eq. 2, where σ and ρ are the conductivity (S/m) and mass density

(kg/m^3) of the tissues and E represents the rms value of the electric field strength in the

tissues (V/m).

$$\text{SAR} = \frac{\sigma |E|^2}{\rho} (W/Kg) \ (2)$$

Accordingly, the safe levels of human exposure to RF fields in the spectrum

ranging between 3 kHz and 300 GHz are measured and tabulated in the standard [26].

Table 1 summarizes the SAR limits for several body parts, in both public and controlled

environments. Note that the SAR values in Table 1 are restricted for frequencies below

3 GHz. For higher frequencies, these values may differ and are beyond the scope of this

thesis work.

Table 1: Standards values of specific absorption rate [26].

Exposure	Frequency Range	Whole-Body (W/Kg)	Partial-Body (W/Kg)	Hands, Wrists, Ankles and Feet (W/Kg)
Controlled Environment	100 KHz - 3 GHz	0.4	10	20
General Public	100 KHz - 3 GHz	0.08	2	4

3.3. Dielectric Properties of Tissues

Understanding the behavior of human tissue when exposed to EM energy is of great importance for several areas of investigation such as electrical impedance imaging, microwave hyperthermia and radiofrequency to name a few. Accordingly, many researchers have focused on deriving a relation between the electrical properties of the human tissues over a wide range of frequencies. In this process, it has been noted that water is the major component of biological materials. Consequently, when considering any part of the human body, water represents the main contributor to permittivity. However, since biological materials are complex mixtures, therefore their electrical response is not limited to only one component. In fact, each tissue has its own contribution depending on the electrical properties and thickness of the layer.

In this section, the concepts of electrical polarization and dispersion for biological tissues are presented, in addition to tables that summarize the dielectric constants and thickness of several biological tissues.

3.3.1. Polarization and Relaxation

An induced electric field applied on biological tissues disturb the distribution charges. This effect is known as electric polarization. The relation for the polarization density in terms of the electric field and the dielectric constants of the material is given by Eq. 3, where E is the induced electric field, P the dielectric polarization density, ε_0 the permittivity of free space and χ_e the susceptibility of the tissues [27].

$$P = \varepsilon_0 \chi_e E \quad (3)$$

17

When an electric field is applied on a structure, several non-idealities cause a deferral between the polarization and the variations in the electric field. This delay is recognized as a dielectric relaxation. To measure the relaxation time of a system, an excitation should be applied on the structure. Then the relaxation time towards reaching a new equilibrium is recorded [27].

3.3.2. Dispersion

Dielectric dispersion is the dependence of the permittivity of a structure on the frequency of an applied electric field. Consequently, the dielectric constant value of a given material is not fixed, but rather frequency dependent. For biological tissues, dispersions are apparent. In [28] the electrical properties of human tissues are categorized by three main dispersions: (1) the low frequency α-dispersion that is linked with ionic diffusion processes, (2) the β-dispersion for radio frequencies, associated with the polarization of cellular membranes, proteins and additional organic macromolecules, and (3) the ϒ-dispersion for microwave frequencies, produced by the polarization of water molecules. Additional dispersions may exist such as the δ-dispersion which is a subset of β-dispersion (Fig. 13). Another observation from Fig. 13 concludes that biological tissues exhibit a relatively high dielectric constant at low frequencies, and these values decrease at higher frequencies.
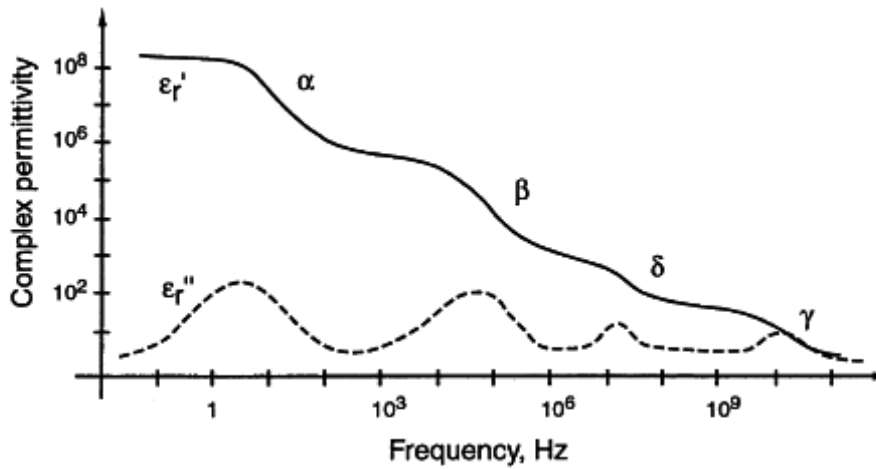
Figure 13: Dispersion of biological tissues [28].

3.3.3. Dielectric Constants of Biological Tissues

For glucose sensing, the objective is to detect the variations in blood glucose while suppressing the effects of minerals in the blood as well as minimizing the influence of the tissues surrounding the arteries and veins. Therefore, understanding the characteristics and behavior of tissues such as skin, fat, blood, bones and muscle is of great importance.

3.3.3.1. Experimental extraction of dielectric constants

Several researchers have investigated the extraction of the dielectric constants of biological tissues in function of frequency. At first, experiments are conducted on animals. In Fig. 14 for instance, the relative dielectric constants for rat muscle, rat brain and canine fat with respect to frequency are shown [29]. For these tissues, the

permittivity of fat is the most consistent along the spectrum. However for the brain and muscles, the values of permittivity dropped noticeably.
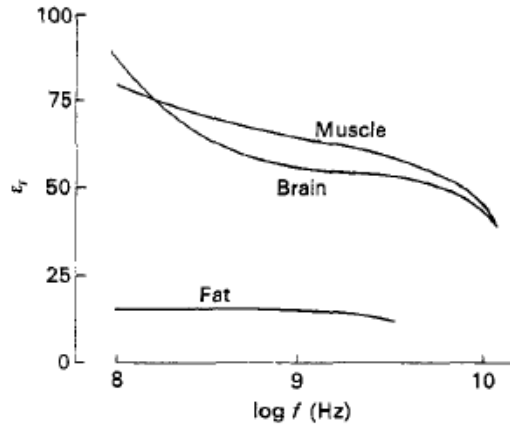
Figure 14: Permittivity of muscle, fat and brain of rats in function of frequency [29].

Later on, using advanced imaging techniques, researchers have been able to characterize the dielectric constants of humans. Tables 2 and 3 summarize the values of permittivity and conductivity for several biological tissues of the human body [30]. These values are collected from the most advanced researches in the field. From table 2, it is again clear that permittivity drops at high frequencies.

Table 2: Permittivity of human biological tissues at specific frequencies [30].

Tissue	$f = 433$ MHz	$f = 915$ MHz	$f = 2.45$ GHz
Skin	47	45	44
Fat	15	15	12
Blood	66	62	60
Muscle	57	55.4	49.6
Artery	-	-	43

Table 3: Conductivity (S/m) of human biological tissues at specific frequencies [30].

Tissue	$f = 433$ MHz	$f = 915$ MHz	$f = 2.45$ GHz
Skin	0.84	0.97	-
Fat	0.26	0.35	0.82
Blood	1.27	1.41	2.04
Muscle	1.12	1.45	2.56
Artery	-	-	1.85

Several other researchers have worked on modeling the human tissues at pre-defined locations in the body such as the neck, the ear, the leg and the arm. This methodology is employed in order to improve the accuracy of the results [31], [32].

3.3.3.2. Mathematical extraction of dielectric constants

In addition to experiments, mathematical models are also developed to predict the variation of the tissues' permittivity as a function of frequency. The Cole-Cole model is perhaps the most known model for dielectric relaxation. Using the Cole-Cole as shown in Eq. 4, and with the appropriate choice of parameters for the tissue, the dielectric behavior can be predicted over the desired frequency range.

$$\varepsilon = \varepsilon_c^{'}(w) - j\varepsilon_c^{''}(w) = \varepsilon_\infty + \sum \frac{\Delta\varepsilon_n}{1+(jw\tau_n)^{(1-\alpha_n)}} + \frac{\sigma_i}{jw\varepsilon_0} \quad (4)$$

ω: Angular frequency.

$\varepsilon_c^{'}(w)$: Frequency-dependent dielectric constant.

$\varepsilon_c^{''}(w)$: Frequency-dependent dielectric loss.

n: Order of model.

21

ε_∞: High frequency permittivity.

$\Delta\varepsilon_n$:Dispersion magnitude

τ_n: Relaxation time constant,

α_n: Dispersion broadening parameter.

σ_i: Static ionic conductivity.

The values of ε_∞, $\Delta\varepsilon_n$, τ_n, α_n, σ_i for the first four orders of the model are summarized in [33]. In this reference, a study is conducted in order to build a relation between the electrical properties and the BGLs. Measurements on blood samples are performed using a dielectric probe kit and a vector network analyzer (Fig. 15). The measurements are implemented at frequencies between 500 MHz and 20 GHz.
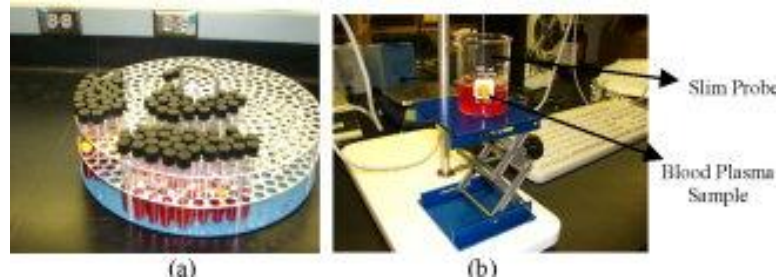
Figure 15: Measurement setup [33].

The glucose levels of the samples are varied between eight different glucose concentrations, ranging from 0 mg/dl to 16,000 mg/dl. The resultant dielectric constant and conductivity in function of frequency are presented in Fig. 16. Results show that the real part of the permittivity in blood decreases for high concentrations of glucose. On the other hand, the conductivity does not vary much between 0.5 GHz and 9 GHz. However, for higher frequencies, small deviations are noticed.

The collected data is then fitted into the Cole–Cole model in order to build a relation between the electrical properties of the blood and the glucose concentration. The formulated model is able to successfully predict the dielectric properties in function of frequency. Consequently, this work prove that the Cole-Cole model is a powerful mathematical tool that can be used to extract the dielectric constants of the blood.
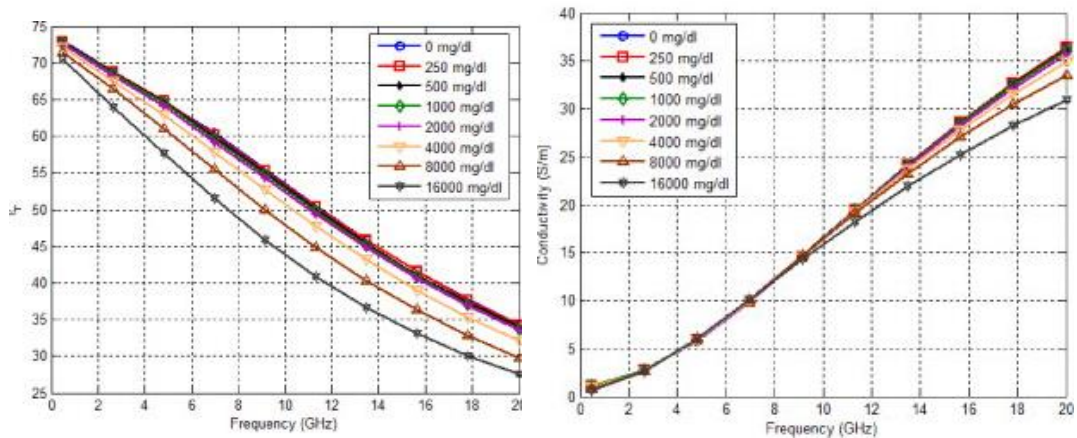
Figure 16: Dielectric properties of blood for different concentrations of glucose [33].

3.3.3.3. Thickness of biological layers

Concerning the thickness of the layers, it is hard to create a general relation that includes all the population. In fact tissues such as fat and muscles are highly dependent on age, gender and lifestyle. However, some approximations may be found in [34]. Also, a summary of the work developed in this process can be found in [35]. Table 4 presents the tissue layers' thicknesses for some body parts. All the values are in millimeters.

Table 4: Thickness of some biological tissues [34].

Tissue	Limb	Thorax	Forehead	Abdomen
Skin	2.5	2	2	2.5
Fat	8	-	2	10
Muscle	25	3	-	20
Bone	-	10	7	-

3.4. Discussion

This chapter addressed the electrical properties of the biological tissues, and the response of these tissues when excited with EM energy, evaluated using both experimentations and mathematical equations such as the Cole-Cole model. These procedures shows that the electrical properties of the biological tissues highly depend on the frequency in addition to the physical and physiological conditions of the subject. Accordingly, the design of any RF glucose sensor must account for these variations, while respecting the standard safe absorption rates set by IEEE.

CHAPTER 4

HIGH LOSS MATERIAL

4.1. Introduction

Chapter 3 demonstrates that biological tissues have the characteristics of lossy materials due to their relatively high permittivity. This chapter provides an overview on high loss materials, which are defined by their complex permittivity. Furthermore, the effect of having multi-layered high loss materials is considered.

4.2. Complex Permittivity

In a lossy media, the effective complex permittivity is given in Eq. 5 where ε'_r is the real permittivity that signifies the stored electric field energy, ε''_r is the imaginary permittivity that accounts for the losses in the medium and $\tan\delta$ is the loss tangent of the medium expressed in Eq. 6.

$$\varepsilon_{eff} = \varepsilon'_r - j\varepsilon''_r(1 - j\tan\delta) \quad (5)$$

$$\tan\delta = \frac{\varepsilon''_r}{\varepsilon'_r} \quad (6)$$

At resonance, the electric and magnetic field energy stored in any resonant structure must be equal. When a material perturbs the stored energy, the field distribution is perturbed and hence the resonance frequency shifts. This shift in the resonance frequency is related to the properties of the sample based on Eq. 7.

$$\frac{\Delta f_r}{f_r} = \frac{\int (\Delta\varepsilon E_1 . E_0 + \Delta\mu H_1 . H_0) dv}{\int (\varepsilon_0 . |E_0|^2 + \mu_0 . |H_0|^2) dv} \quad (7)$$

f_r and Δf_r are the resonance frequency and the shift in the resonance frequency respectively, $\Delta\varepsilon$ and $\Delta\mu$ represent the change in the permittivity and permeability. E_0 and H_0 represent the field distributions in free space and E_1 and H_1 are the field distributions with the perturbation of the MUT [36].

4.3. Extraction of the Real Permittivity ε'_r

The resonant frequency is related to the structure's properties using Eq. 8.

$$f_r = \frac{1}{2\pi\sqrt{L(C_{Subtrate}+C_{SUT})}} \quad (8)$$

Where L is the total inductance, $C_{Subtrate}$ is the substrate capacitance, and C_{SUT} is the capacitance of the sample under test. The only unknown in this equation is the capacitance of the sample under test which is directly proportional to its real permittivity ε'_r according to Eq. 9. Consequently a relation between ε'_r and f_r can be generated. The generated relation allows the characterization of the permittivity based on the shifts in the resonant frequency [37].

$$C = \frac{\varepsilon'_r d}{A} \quad (9)$$

4.4. Extraction of the Imaginary Permittivity ε''_r

The quality factor Q is related to the loss resistance using Eq. 10.

$$Q = \frac{R}{2\pi f_r L} \quad (10)$$

The variable in this case is the loss resistance of the sample under test R which is directly proportional to its loss tangent $\tan\delta$ according to Eq. 11. Consequently a relation between ε''_r, f_r and the S-parameters can be generated [37].

$$\tan\delta = \frac{2\pi f_r L}{R} \ (11)$$

4.5. Effective Dielectric Permittivity

For a stacked multi-layered structure (Fig. 16), the relative permittivity 'ε_r' of each layer is unique ($\varepsilon_r = \varepsilon_{Material}$). However, the effective permittivity 'ε_{eff}' of the whole structure depends on the permittivity and thickness of each layer. Eq. 12 was developed to compute the effective dielectric constant of multilayered structures with thickness $h \cong \lambda/10$ [38].

$$\varepsilon_{eff} = \frac{|d_1|+|d_2|+\cdots+|d_n|}{\left|\frac{d_1}{\varepsilon_1}\right|+\left|\frac{d_2}{\varepsilon_2}\right|+\cdots+\left|\frac{d_n}{\varepsilon_n}\right|} \ (12)$$

With ε_n being the dielectric constant of the top layer. d_n is calculated using Eq. 13, k_n is given in Eq. 14 and $\frac{K(k_n)}{K'(k_n)}$ in Eq. 15. h_n refers to the thickness of the top layer [38].

$$d_n = \frac{K(k_n)}{K'(k_n)} - \frac{K(k_{n-1})}{K'(k_{n-1})} - \frac{K(k_1)}{K'(k_1)} \ (13)$$

$$k_n = \frac{1}{\cosh\left(\frac{\pi w}{4(h_n+h_{n-1}+\cdots+h_1)}\right)} \ (14)$$

$$\frac{K(k_n)}{K'(k_n)} = \frac{1}{\pi}\ln\left(2\frac{1+\sqrt{kn}}{1-\sqrt{kn}}\right) \text{ for } 0.7 \leq kn \leq 1 \ (15)$$

4.6. Discussion

This chapter presented, from an EM perspective, the equations that define high loss materials and their effect on any EM wave. Furthermore, it assessed the effect of placing several high loss layers on waves' propagation.

CHAPTER 5

MATERIAL CHARACTERIZATION

5.1. Introduction

Material characterization signifies measuring the structure and electrical properties of a material under test (MUT). In Applied electromagnetics and RF systems, two techniques are developed for material characterization purposes. The two techniques are divided as: the resonant and non-resonant methods. These methods are applied using waveguides or using planar circuit boards. However, since the objective is to design a wearable device for BGL monitoring, the device must be as small as possible. Consequently, it is essential to use printed circuit boards' techniques in order to decrease both the size and cost of the device [39].

The most known and used planar method relies on microstrip technology. This chapter presents this approach and provides a review on the most common material characterization methods using microstrips.

5.2. Microstrip Lines

Microstrip lines are planar transmission lines that are easy to manufacture and integrate on low cost substrates. Fig. 17 shows the geometry of a microstrip line. The conductor of width (W), is printed on the substrate of thickness (d) and dielectric constant (ϵ_r) [36].
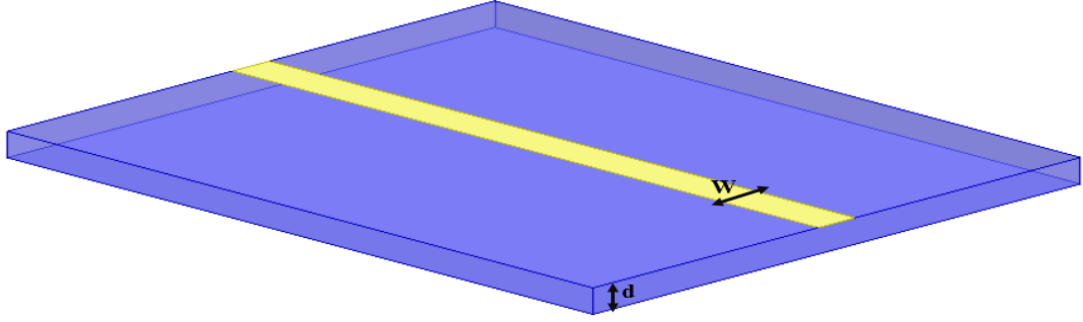
Figure 17: The geometry of microstrip transmission line.

The effective dielectric constant of a microstrip line depends on the conductor width and the thickness of the substrate as in Eq. 16 [36].

$$\varepsilon_e = \frac{\varepsilon_r+1}{2} + \frac{\varepsilon_r-1}{2} \times \frac{1}{\sqrt{1+12d/W}} \quad (16)$$

The characteristic impedance of a microstrip line depends on the substrate thickness and dielectric constant and the conductor width. It is calculated using Eq. 17 [36].

$$Z_0 = \begin{cases} \frac{60}{\sqrt{\varepsilon_e}} \ln\left(\frac{8d}{W} + \frac{W}{4d}\right) & \text{for } \frac{w}{d} \le 1 \\ \frac{120\pi}{\sqrt{\varepsilon_e} \left[\frac{W}{d}+1.393+0.667 \ln\left(\frac{W}{d}+1.444\right)\right]} & \text{for } \frac{w}{d} \ge 1 \end{cases} \quad (17)$$

The width to depth ratio is computed as shown in Eq. 18, and the parameters A and B are provided in Eq. 19 and Eq. 20 respectively [36].

$$\frac{W}{d} = \begin{cases} \frac{8e^A}{e^{2A}-2} \text{ for } \frac{w}{d} < 2 \\ \frac{2}{\pi}\left[B - 1 - \ln(2B-1) + \frac{\varepsilon_r-1}{2\varepsilon_r}\left\{\ln(B-1) + 0.39 - \frac{0.61}{\varepsilon_r}\right\}\right] \text{ for } \frac{w}{d} > 2 \end{cases} \quad (18)$$

$$A = \frac{Zo}{60}\sqrt{\frac{\varepsilon_r+1}{2}} + \frac{\varepsilon_r-1}{\varepsilon_r+1}\left(0.23 + \frac{0.11}{\varepsilon_r}\right) \quad (19)$$

$$B = \frac{377\pi}{2Zo\sqrt{\varepsilon_r}} \quad (20)$$

30

5.3. Characterization Methods

5.3.1. Non-Resonant Methods

Non-resonant characterization methods provide a general knowledge of EM properties over a wide range of frequencies. For that, either the reflection or the reflection/transmission parameters are used to extract either one or two EM properties of the MUT [39].

5.3.1.1. Reflection method

This method uses a planar transmission line built on a substrate filled with the MUT (Fig. 18). The EM properties of the sample are extracted from the S parameters. The disadvantage of this method lies in the fact that it cannot be used for samples of different thicknesses.
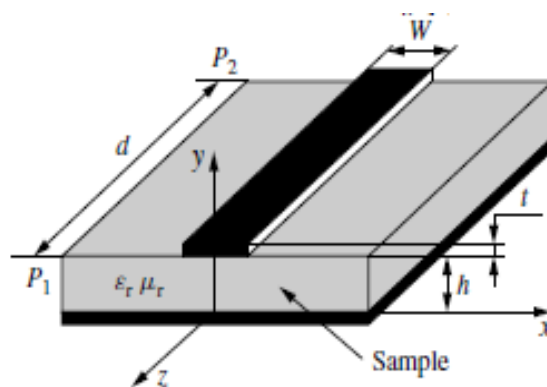
Figure 18: Transmission line setup [39].

5.3.1.2. Transmission/reflection method

This is another non resonant technique that is adequate for all the samples regardless of the thickness. The determination of the complex permittivity and

permeability requires the measurement of the S11 and S12 parameters. During

measurement, the microstrip line is loaded by a film and its support (Fig. 19). The film

occupies a part of the cross section of the microstrip line. After determining the S11 and

S12 parameters, the transmission and reflection coefficients are calculated from Eq. 21

and Eq. 22. Consequently ε_r and μ_r can be extracted [39].

$S11 = S22 = r_1 \exp(-2j\gamma olo)$ (21), where r_1 is the reflection coefficient.

$S21 = S12 = t_1 \exp(-2j\gamma olo)$ (22), where t_1 is the transmission coefficient.
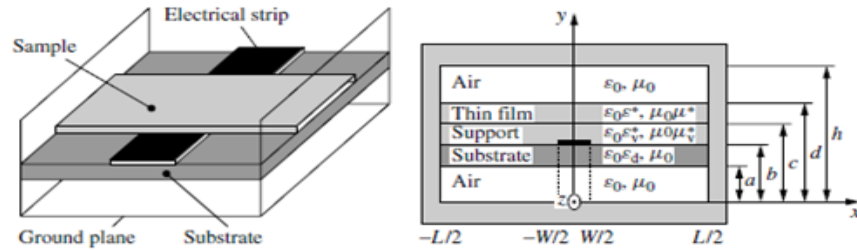
Figure 19: Transmission/Reflection setup [39].

5.3.2. Resonant Methods

Resonant methods provide accurate knowledge of the EM properties over one or

multiple discrete frequencies. Two techniques lie within the resonant methods, these

techniques are known as: the resonator and the resonant perturbation method.

5.3.2.1. Resonator method

The resonator method is used to extract the permittivity and the loss tangent

values based on the measurements of the resonant frequency and the quality factor. It

consists of placing the MUT between two conducting plates of a resonator. This technique is highly accurate for only low loss dielectrics. For high dielectric constants' materials, the resonant perturbation method is the most preferred.

5.3.2.2. The resonant perturbation method

This method consists of placing a dielectric MUT near a resonator, which causes a shift in frequency and quality factor. Based on this shift the EM properties of the material can be extracted. The sensitivity of this technique is highly dependent on the type of resonator used. Several planar resonators are discussed in the following section [39].

5.4. Planar Resonators

In microstrip technology, multiple resonators are used for material characterization such as the straight ribbon, the T resonator and the ring resonator.

5.4.1. Straight Ribbon Resonator

The straight ribbon resonator (Fig. 20.a) is an open ended line of length $l = n \times \frac{\lambda}{2}$, n=1,2… The fields in a straight ribbon resonator extend beyond the ends of the line causing radiation losses (fringing effect). This effect is modeled as a grounding capacitance or consequently as a transmission line. As a result, the quality factor of such

type of resonators is relatively low. The ribbon resonator can be adjusted, as shown in

Fig. 20, to increase the quality factor [40].
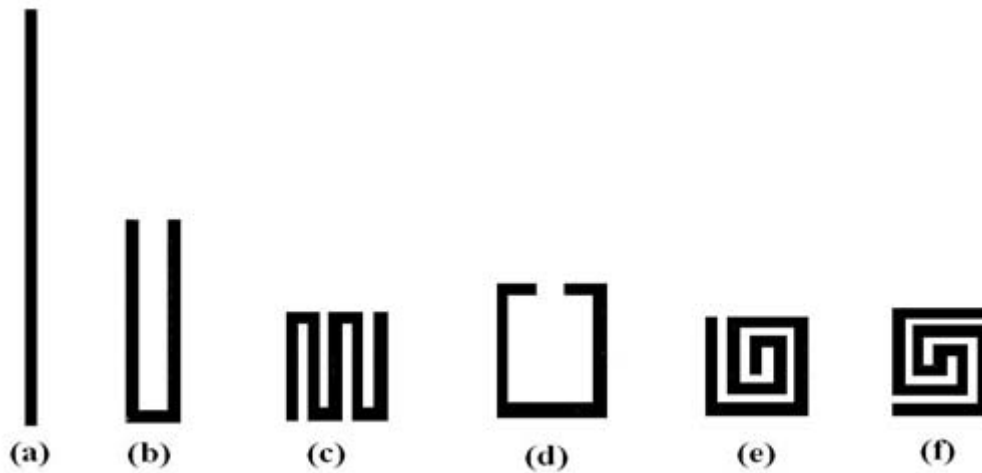
Figure 20: Typical one-dimensional microstrip resonators: a) half-wave length line resonator, b) hairpin resonator, and c) to f) other open loop resonators. [40].

5.4.2. T- Resonator

The T-resonator method is introduced as a technique that enhances the

transmission line characterization, reduces the radiation losses, and decreases the size of

the device. A T-resonator is a quarter wave long transmission line shown in Fig. 21.

The T pattern is an open-end transmission stub that resonates at odd integer multiples of

$\lambda/4$. By coupling the structure directly to the transmission line, and by having only one

open end, inaccuracies of the gaps are eliminated and the radiation and discontinuity

losses are reduced.
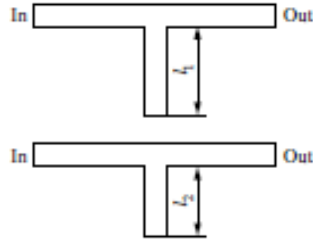
Figure 21: T-resonator [39].

Using this resonator, ε_{reff} is determined from f_r using $\varepsilon_{reff} = \left(\frac{nc}{4fr(l+lc)}\right)$ with $n = 1,3,5 \dots$ and hence the permittivity of the material is determined.

The loss tangent is also determined from the quality factor using $\tan\delta = \frac{\varepsilon_{reff}(\varepsilon_r - 1)}{Qd\varepsilon_r(\varepsilon_{reff} - 1)}$ with $Q_d = \frac{QQc}{Qc - Q}$, Q being the measured quality factor and Q_c the calculated quality factor.

5.4.3. Ring Resonator

The ring resonator, shown in Fig. 22, does not have open ends, which decreases its radiation loss and enhances its quality factor even more. This fact made the ring resonator one of the most accurate and sensitive planar resonators in material characterization. The resonant condition for the first resonant mode is given by Eq. 23, where r is the ring's mean radius [39]. Therefore for a given radius of the ring, the wavelength that produces the first resonant mode can be determined.

$$2\pi r = \lambda_g \ (23)$$
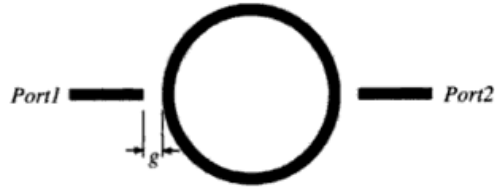
Figure 22: Ring resonator [41].

When loaded by a material with a specific dielectric constant, the resonant frequency of the ring, where the peak occurs, decreases [41]. The larger the dielectric values the higher is the shift. This behavior is due to the fact that the energy coupled into the ring splits equally over the top and bottom sections of the ring. Therefore, a standing wave will develop in a way such that when the ring is in resonance, the maxima occur at the coupling gaps and the nulls are noticed at the top and bottom of the ring [41].

To determine the properties of a sample, a single layer substrate can be used in which the MUT is used as the substrate. Another possibility is multi-layer substrate in which the ring acts as a measurement device and the MUT is placed as a cover on top of the circuit. A PTFE block can be used to eliminate the air gap between the circuit and the MUT. For the setup in Fig. 23, the permittivity ε_1 and the thickness h of the substrate are known. With no loading, $\varepsilon_2 = \varepsilon_3 = 1$. Therefore f_0 can be measured and $\varepsilon_{\text{reff},0}$ is calculated from the substrate properties. With loading ε_3 is known and ε_2 must be determined. To determine ε_2, $\varepsilon_{\text{reff},1}$ is calculated using Eq. 24 and f_1 is calculated using Eq. 25 [39].

$$\varepsilon_{\text{reff},1} = \varepsilon_{\text{reff},0} \left(\frac{f_0}{f_1} \right)^2 (24)$$

36

$$\pi D = \frac{nc}{fo\sqrt{\varepsilon_{reff,0}}} = \frac{nc}{f1\sqrt{\varepsilon_{reff,1}}} \quad (25)$$
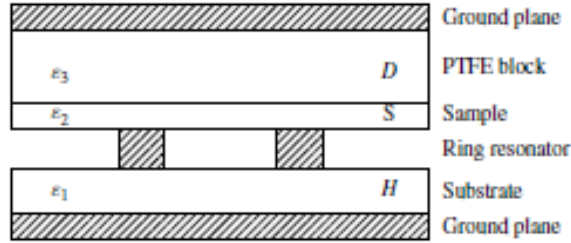
Figure 23: Ring resonator measurement setup [39].

Several resonator-based sensors are proposed in literature as highly sensitive

sensors for the aim of characterizing materials' dielectric constant variations. The focus

has always been on designing narrow-band sensors with a high quality factor as in [42].

Such response increases the intensity of electric fields. The use of complementary split

ring resonators (CSRRs) with narrow responses has been examined in [42], and [43].

The proposed resonators are able to sense and predict the dielectric constant values of

low loss substrates with a percentage error that does not exceed 10% [42]. Also, by

increasing the number of resonators from two to three, the sensor is able to predict both

the dielectric constant and thickness of the substrates with lower error [43], compared to

[42].

5.5. Discussion

This chapter addressed several planar methods for materials characterization.

The resonant perturbation technique has the advantage of extracting the electrical

properties without perturbing the MUT. Its sensitivity however is highly dependent on

the type of resonator employed. Accordingly, several resonators are also presented in this chapter, such as the open loop and ring resonators. Modified versions of these two structures are considered in this thesis as discussed in the following chapter.

CHAPTER 6

DESIGN OF EM-BASED GLUCOSE SENSORS

6.1. Introduction

In this chapter, several two port RF filters that act as glucose sensors are designed and tested. The performance of a narrow band SRR based band-pass filter is initially evaluated. Also two novel broad-band and tunable octa-band reject filters are proposed. The narrowband BPF operates at 2.4GHz. The broad-band reject filter covers the whole frequency range between 1.25 GHz and 2.25 GHz. Finally, the tunable octa-band reject filter covers multiple bands ranging between 1.5 GHz and 2.4 GHz.

The designs characteristics of these filters are discussed in this chapter. The proposed structures are fabricated and tested using different substrates. A comparison between the simulated and the measured results is also presented, and a good agreement is noticed.

6.2. Methodology

The proposed sensors are initially designed, simulated and tested in free space scenarios. To examine the performance of the filters, the scattering parameters, S11, S21, and S22, are selected. S11 and S22 represent the reflection losses at ports 1 and 2, and S21 refers to the insertion loss from port 1 to port 2. From an RF point of view, for the design of a band stop filter, in the operating band, it is desirable to have the

magnitude of |S21| value lower than − 10 dB and a |S11| value near 0 dB. For the case of band pass filters, these requirements are the opposite.

After reaching the required response, the filters' behavior near human tissues was examined. This allows to estimate and compare the performance of these sensors as glucose measurement devices. For this purpose, a model of the human body is considered within the simulator as shown in Fig. 24 [44]. To reduce the simulation time, the human model is dissected into smaller and simpler layers as explained in the following chapter.
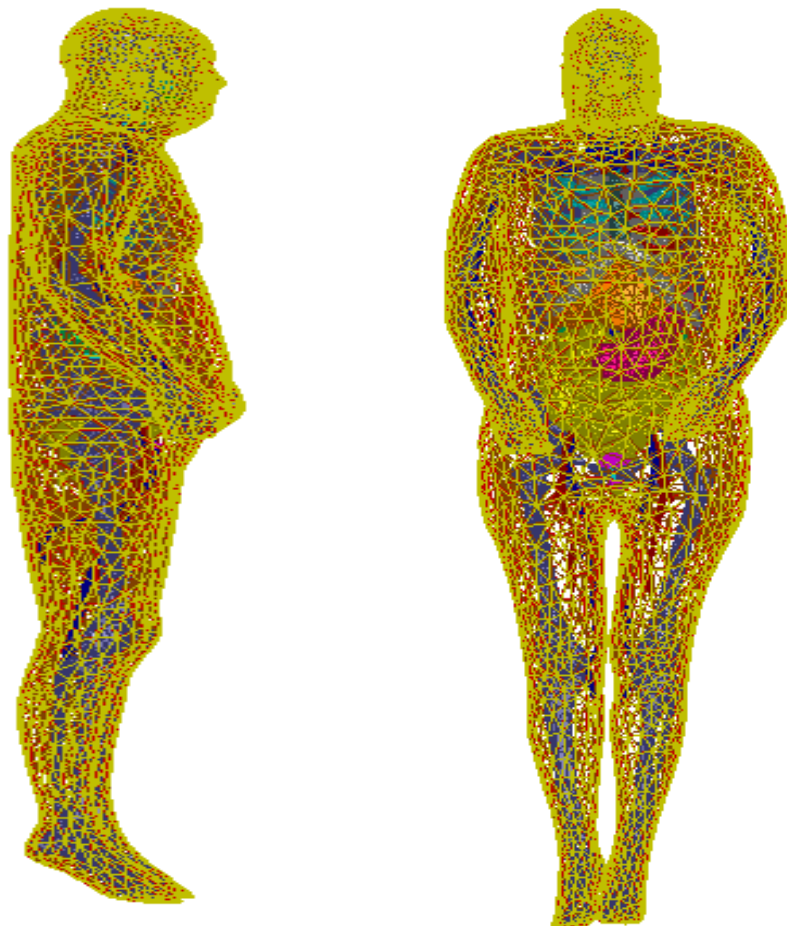
Figure 24: Human model in ANSYS [44].

6.3. Design Considerations

Many challenges need to be addressed, while developing any non-invasive and continuous glucose measurements technique. First, high sensitivity and selectivity to glucose variations is needed; it is essential that the proposed system is capable of sensing and detecting BGLs in spite of possible variations in other biological constituents that may induce undesired effects on the measurements. The sensitivity of the sensors is linked to both distribution and magnitude of the induced electric field across the resonating structure. In fact, better sensitivity is achieved by inducing strengthened fields across the largest possible area [42]. The main target of this research is to maximize the sensitivity of the proposed sensors by increasing the distribution and intensity of the induced electric fields.

The proposed device must also meet the standard accuracy as required by the international organization for standardization (ISO). The most recent version, ISO:15197:2013, specified that for BGLs lower than 100 mg/dL, an accuracy of ± 15 mg/dl should be reached and for BGLs of 100 mg/dL or more, an accuracy of ± 15% is acceptable as shown in Table 5 [45].

Additionally, the suggested device should be compact, light and wearable. Furthermore, several environmental factors must also be considered, including ambient and body temperature, humidity as well as body movements.

Table 5: FDA's accepatable accuracy for glucose measurements devices [45].

	Glucose Concentrations	**Criteria**
Requirements for blood glucose monitoring systems for self-testing	$\geq$ 100 mg/dL	95% within $\pm$ 15%
	< 100 mg/dL	95% within $\pm$ 15 mg/dl
Consensus error grid analysis	Entire Range	99% in Zones A and B

6.4. Proposed Sensor #1

Initially, a narrow band pass filter is designed and tested. This sensor is an SRR-based band pass filter that consists of two gap-coupled split ring resonators. SRRs are left handed metamaterials that exhibit negative values of magnetic permeability and permittivity near the resonant frequency. These resonators are electrically small structures, which means that the ring's perimeter is less than $\lambda/2$ at resonance. For these small quasi-static resonators, resonances are initiated due to a combination of inductances and capacitances [46]. The equivalent circuit of the structure is illustrated in Fig 25. In addition, the resonant frequency is calculated using Eq. 26 [47]. For the proposed design, L_s = 20.6 nH, C_s = 0.21 pF and f = 2.4 GHz.

$$f = \frac{1}{2\pi \times \sqrt{Ls \times Cs}} \quad (26)$$
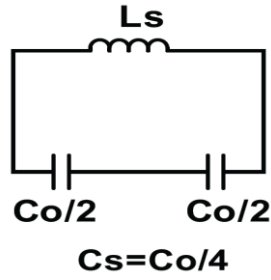
Figure 25: Equivalent circuit model of SRRs [47].

In order to maximize coupling, the gap between the adjacent structures must be minimized. However, due to fabrication constraints, we are restricted to a minimum value of 0.18 mm. To further increase coupling from the transmission line to the largest resonator, an enhanced coupling periphery is considered as shown in Fig. 26. This structure improves coupling by increasing the coverage area between the two entities [41]. The dimensions of proposed design using a 1.6 mm-thick Rogers 5880 substrate are summarized in Table 6. The distribution of the induced fields over the top layer is illustrated in Fig 27. The maximum achieved electric field intensity is $4.85 \times 10^4 \ V/m$.
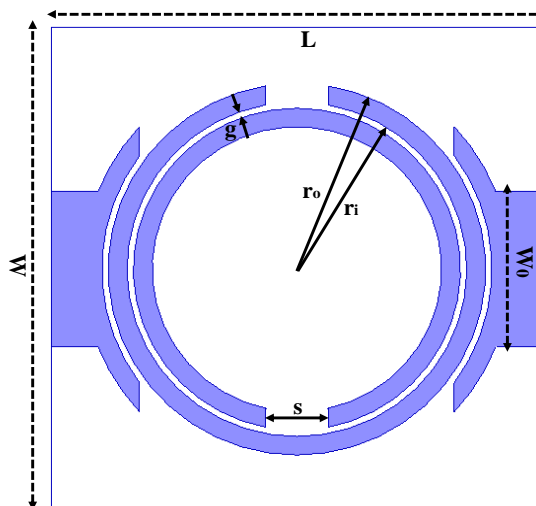
Figure 26: Proposed split ring resonator design with enhanced coupling on periphery. Image obtained from HFSS simulations.

Table 6: Dimensions of the proposed BPF.

Parameter	Dimensions (mm)
L	16
W	16
r_o	5.2
r_i	4.6
g	0.2
s	2
W_o	5
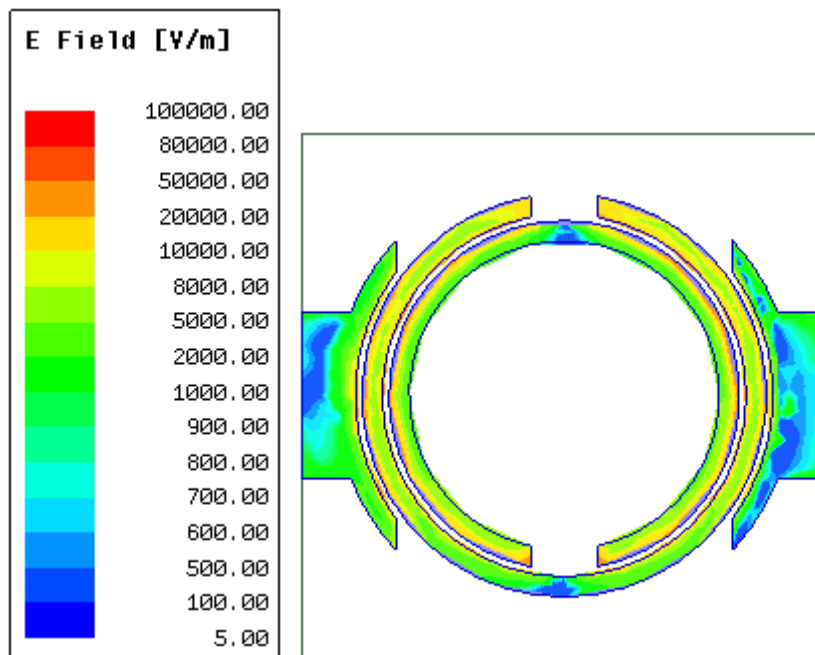
Figure 27: Electric field distribution on the top layer of the proposed SRR-based filter.

A prototype of the SRR-based BPF is realized for verification of the simulated results. The prototype is fabricated through chemical etching technique on a Roger RT/Duroid5880 substrate as shown in Fig. 28. Fig. 29 demonstrates a good agreement

between the simulated and measured results of the transmission and reflection

coefficients.

Figure 28: Fabricated prototype of the SRR-based filter.
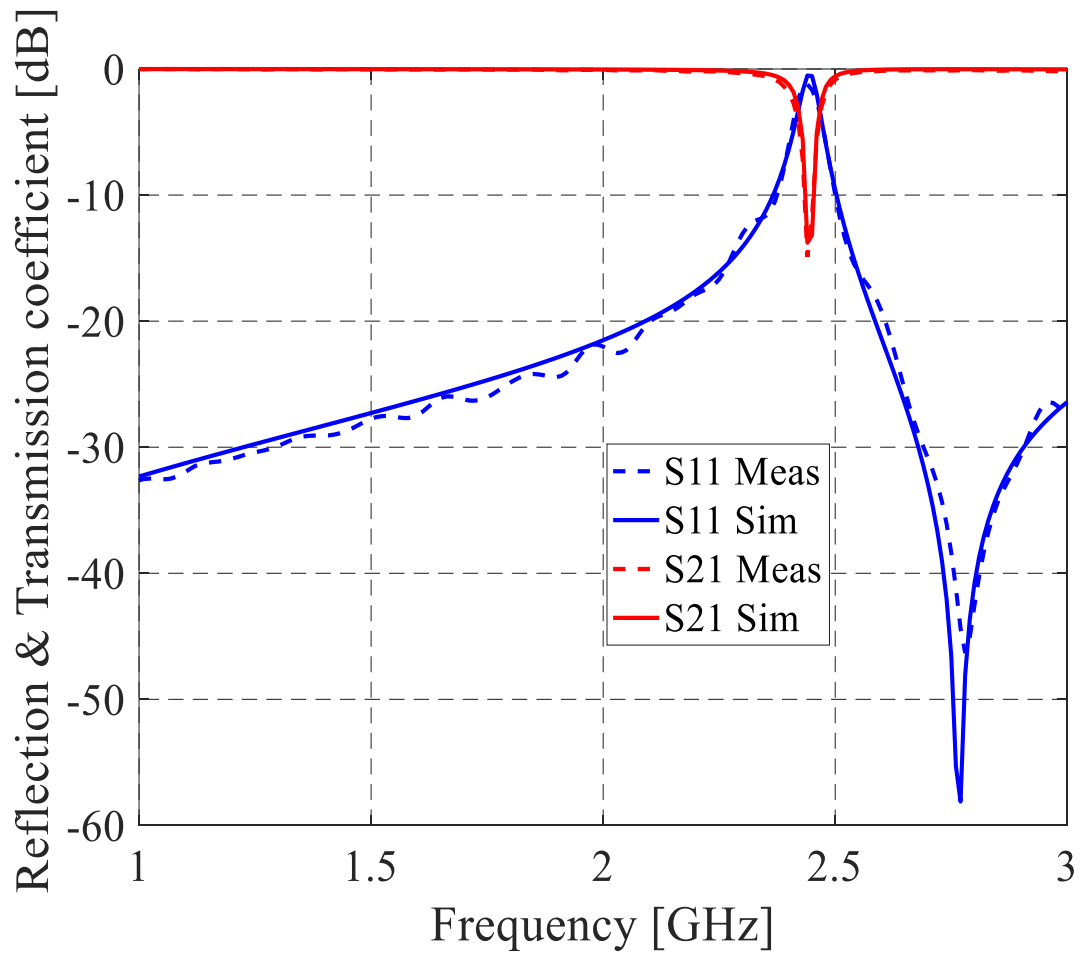
Figure 29: Simulated and measured response of the SRR-based filter.

6.5. Proposed Sensor #2

The second proposed sensor is a novel broad-band reject filter design that employs log-periodic distributed complementary open loop resonators (OLRs). The proposed filter is designed to be implemented as a sensitive, non-destructive and compact sensor for BG monitoring over a broad-band frequency range. It also enables estimating the dielectric constant using multiple features, which leads to a low prediction error.

Log periodic structures are widely used in order to increase the bandwidth of a microwave structure. In the literature, one design that is discussed in [48] resorts to three complementary circular rings that are etched at the top layer in order to produce a broad rejection band. The filter in the corresponding study exhibits a large scaling factor of 0.98, which limits its bandwidth (fractional bandwidth ~ 20%).

6.5.1. Design Structure

The proposed design is a double-sided microstrip structure that operates as a broad-band reject filter. The top and bottom layers of the design are shown in Fig. 30.

6.5.1.1. Top layer

The top layer consists of an exponentially tapered transmission line that couples the magnetic flux density to the underneath resonators. The feed line is optimized based on the tapering techniques discussed by the author in [36] to better

enhance the broad-band operation of the filter based on Eq. 27 and Eq. 28.

$$Z(z) = Zoe^{a \times z} \text{ (27)}$$

$$a = \frac{1}{L} \times \ln(\frac{Z_l}{Z_o}) \text{ (28)}$$

Z_l and Z_o are the impedances to be matched and L is the length of the line. By setting $Z_l = 100$ ohms, $Z_o = 50$ ohms and $L = 3$cm, the impedance and width of the line at a specific position can be calculated. The values of Z and W for some positions along the line are shown in Table 7. The width is computed based on Eq. 18.
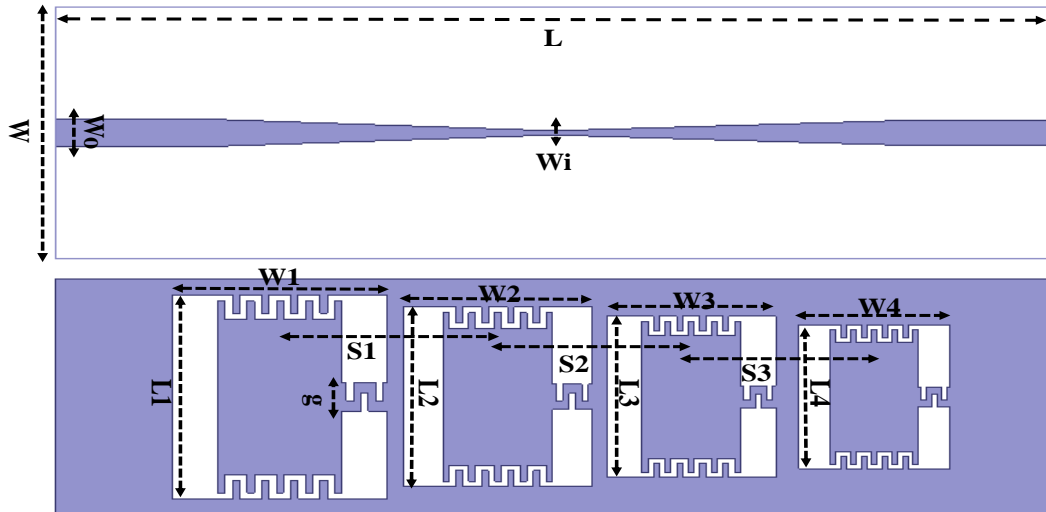
Figure 30: Proposed log-periodic broad-band reject filter.

Table 7: Dimensions of the designed tapered line.

L (cm)	Z (ohms)	W (mm)
0	50	1.88
1	63	1.208
2	79.37	0.709
3	100	0.367

6.5.1.2. Bottom layer

The bottom layer of the filter is a defected ground plane (DGS) that includes four complementary OLRs. A DGS has a defect integrated in the ground plane which alters the uniformity of the plane. This defect manifested as a slot disturbs the shielding current distribution, which increases the inductance and capacitance of the line. The circuit area of DGS is relatively small compared to other structures. DGS provides sharp selectivity at cutoff frequencies with excellent rejection in the stop band and minimum ripples in the pass band. The stop band response can be further enhanced by increasing the number of cells (slots). In this design the number of cells is equal to four. DGS is modeled as RLC equivalent components in series with the transmission line to which it is coupled as demonstrated in Fig. 31. The input and output impedances are those of the line section, and the values of the RLC model are determined by the dimensions of the introduced slots as well as their positions relative to the transmission line. The LC components determine the resonant frequency of the structure.
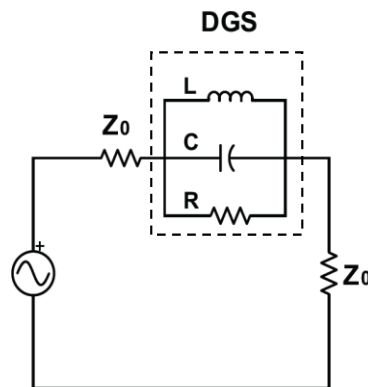
Figure 31: Equivalent model of a defected ground structure.

In the proposed design, the dimensions and spacing of the OLRs follow a log-periodic distribution as given in Eq. 29, where τ is a scaling factor that affects the desired impedance bandwidth B for the four required OLRs in the proposed design [49]. Moreover, the electrical length of the largest OLR is taken to be one-half the wavelength of the lowest desired frequency of operation as shown in Eq. 30. The dimensions of the suggested filter configuration, for $\tau=0.88$, and using a 1.27 mm-thick Rogers 3006 substrate are presented in Table 8.

$$\frac{W_{n+1}}{W_n} = \frac{L_{n+1}}{L_n} = \frac{S_{n+1}}{S_n} = \frac{1}{\tau} \qquad (29)$$

$$L_{max} = \frac{\lambda_{min}}{2} = \frac{v_p}{2 \times f} \qquad (30)$$

Table 8. Dimensions of the proposed log-periodic BRF designed on a 1.27 mm-thick Rogers 3006 substrate.

Parameter	Dimensions (mm)	Parameter	Dimensions (mm)
L	60	W_1	20
W	18	W_2	17.6
W_O	1.9	W_3	15.5
W_I	0.35	W_4	13.6
L_1	14.7	S_1	13.2
L_2	13	S_2	11.6
L_3	11.4	S_3	10.2
L_4	10	g	2

6.5.2. Design Features

6.5.2.1. Electric field distribution

  To upsurge the distribution of fields, the configuration of the embedded resonators is modified as shown in Fig. 32. This helps spread the induced fields across the ground plane, and hence causes a higher interaction with the loading MUT. Furthermore, by perturbing the resonators, the magnitude of the induced fields tends to increase thereby leading to enhanced sensitivity levels. The advantage of the modified OLR in terms of sensitivity is illustrated in Fig. 32, where the maximum attained value of electric fields increased from $8 \times 10^3 \, V/m$ to $5 \times 10^5 \, V/m$.
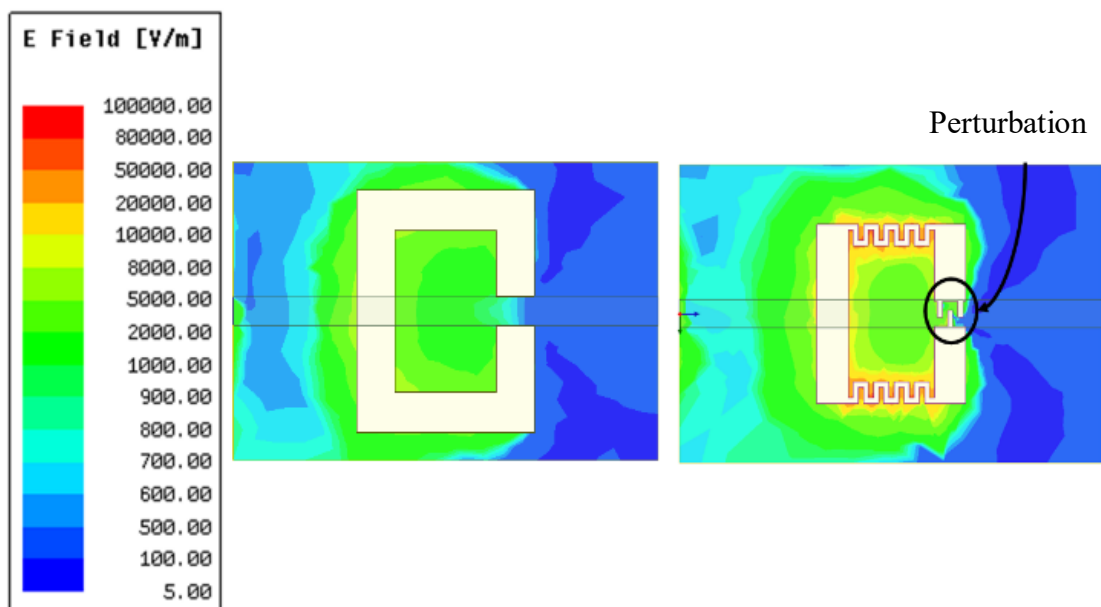
Figure 32: Electric field distribution of the traditional and modified OLR.

Reducing the overall size of the filter requires the implementation of miniaturization techniques such as line meandering. This concept is based on folding a conductor back and forth to have a miniaturized structure. By executing this approach, the wave is not able to cross the specified distance in a straightforward fashion. Instead it must traverse the straight-line several times. This increases the curvature of the lines resulting in an increase in the fringing of fields, which makes the microstrip line appear electrically longer. Therefore, a smaller physical length is required for the same resonant frequency, leading to a smaller, more compact structure. A Meander line includes multiple turns comprising vertical and horizontal sections (Fig. 33). In this design, the proposed resonators consist of eight turns uniform meander lines and the dimensions of the turns are optimized by simulation. The size of the modified OLR is 30 % less than that of the conventional structure at 1.43 GHz. In addition, the relatively high dielectric constant of the substrate reduces further the size of the filter.

Figure 33: Four turns uniform meander line.

6.5.3. Fabrication and Measurements

To validate the performance of the proposed filter in carrying out glucose sensing processes, a prototype is fabricated using the Computer Numerical Control

milling machine on a 1.27 mm-thick Rogers 3006 substrate as shown in Fig. 34. The complete size of the design is 1.8 cm × 6 cm. A good agreement between the simulated and measured S-parameters of the fabricated filter is attained as demonstrated in Fig. 35.

Figure 34: Top and bottom layers of a fabricated prototype of the proposed log-periodic BRF built on a 1.27 mm-thick Rogers 3006 substrate.

Figure 35: Simulated and measured response of the proposed log-periodic BRF built on a 1.27 mm-thick Rogers 3006 substrate.

6.5.4. Alternative Design

The proposed filter is envisioned as a future wearable glucose sensor to be placed on the human body. Although the size of the device is quite compact, however it is interesting to build it on a thinner and more flexible substrate. For this purpose, a modified version of the design was simulated on three different substrates: Rogers 3003, Polyethylene and Polyimide. The properties of these substrates are presented in Table 9. The dielectric constants of the considered substrates are quite similar. However, the properties of these substrates highly differ in terms of thickness and loss tangent. Accordingly, the dimensions of the feeding line and resonators are adjusted and optimized using HFSS in order to achieve a similar response to the one realized with Rogers 3006. It is worthy to mention that for PET and polyimide, silver is used instead of copper to model the conductive traces. This is due to the fact that traditional manufacturing methods cannot be used to etch designs on these substrates. Instead, inkjet printing could be considered as a fabrication method and this process uses silver nanoparticle as a conductive ink. This ink has a lower conductivity ($5 \times 10^6 \, S/m$) compared to copper ($5.8 \times 10^7 \, S/m$).

Table 9: Characteristics of several flexible substrates.

Substrate	Thickness (μm)	Permittivity	Tan (δ)
Rogers 3003	250	3	1e-3
PET	136	2.99	5.7e-3
Polyimide	25	3.5	8e-3

The return loss and insertion loss responses of the filter designed using the three substrates are shown in Fig. 36. The filter designed using the Rogers 3003 substrate provides the best response in terms of bandwidth and return loss levels. This is mainly attributed to the relatively lower loss tangent of the substrate and the high conductivity of copper compared to silver ink.
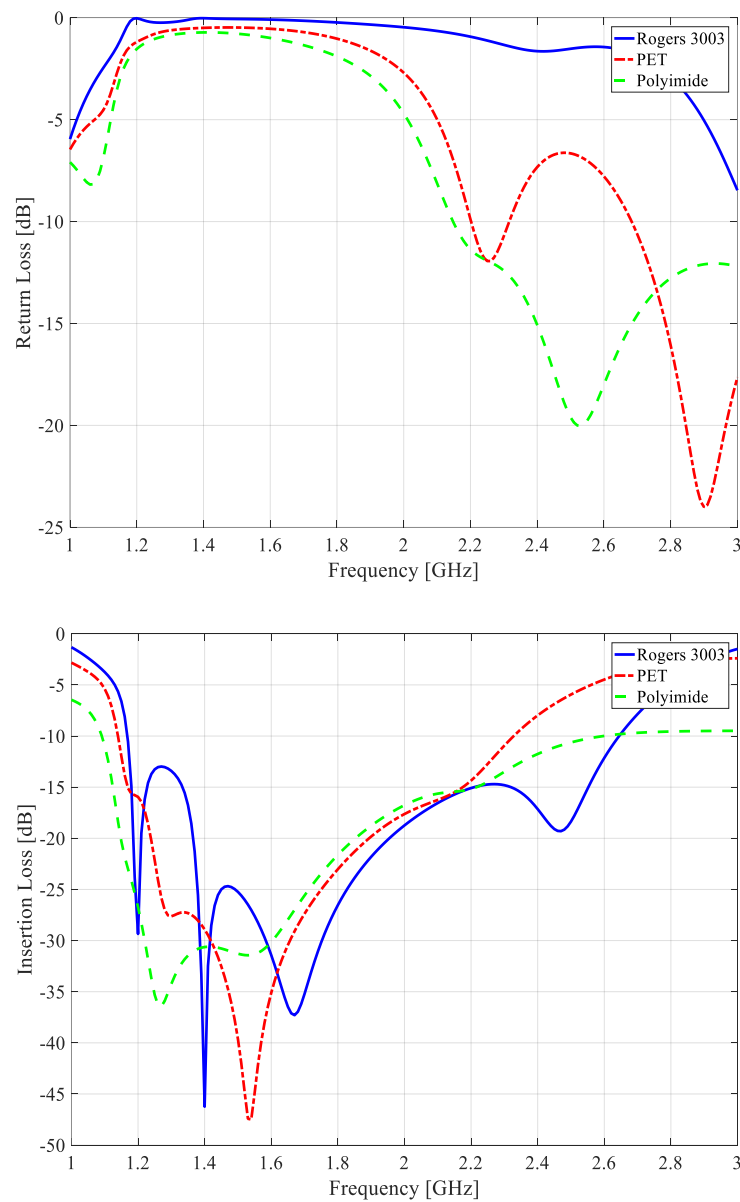
Figure 36: Response of the log-periodic BRF using three flexible substrates.

A prototype of the log-periodic filter is therefore realized on a 0.25 mm-thick Rogers 3003 substrate as shown in Fig. 37. The dimensions of the design are presented in Table 10. A good agreement between the simulated and measured S-parameters of the fabricated filter is attained as illustrated in Fig 38.
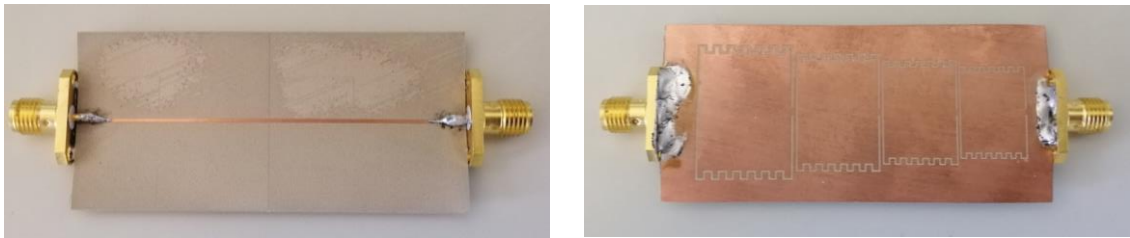
Figure 37: Top and bottom layers of a fabricated prototype of the proposed log-periodic BRF built on a 0.25 mm-thick Rogers 3003 substrate.
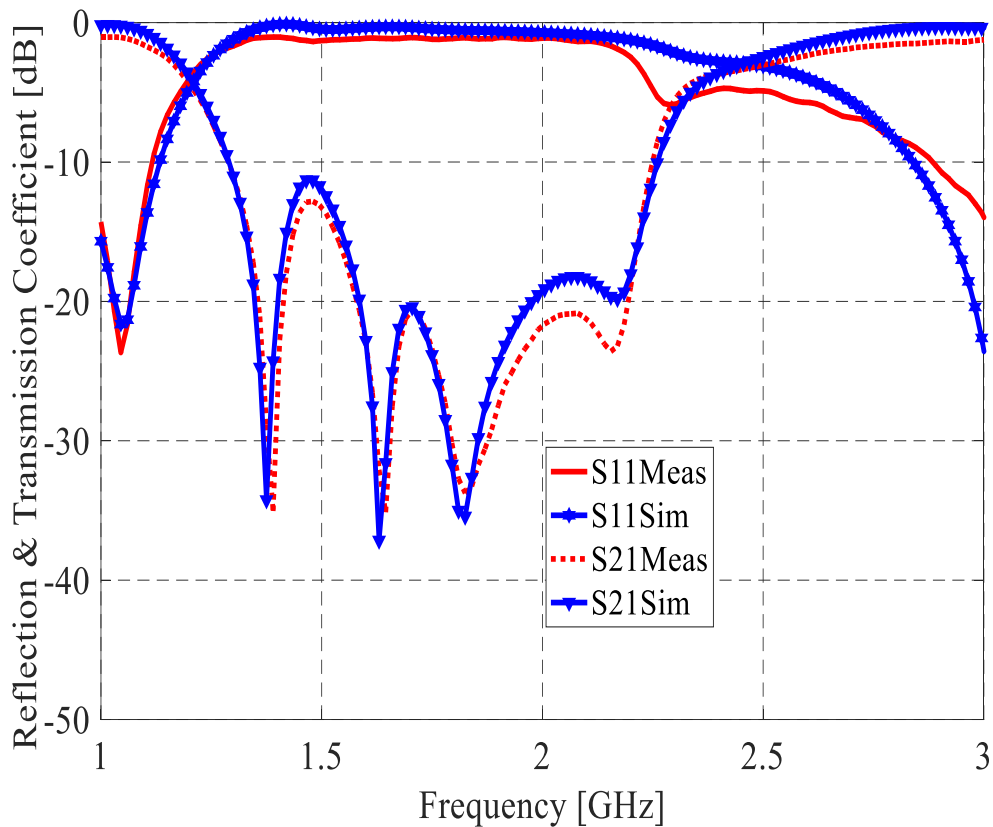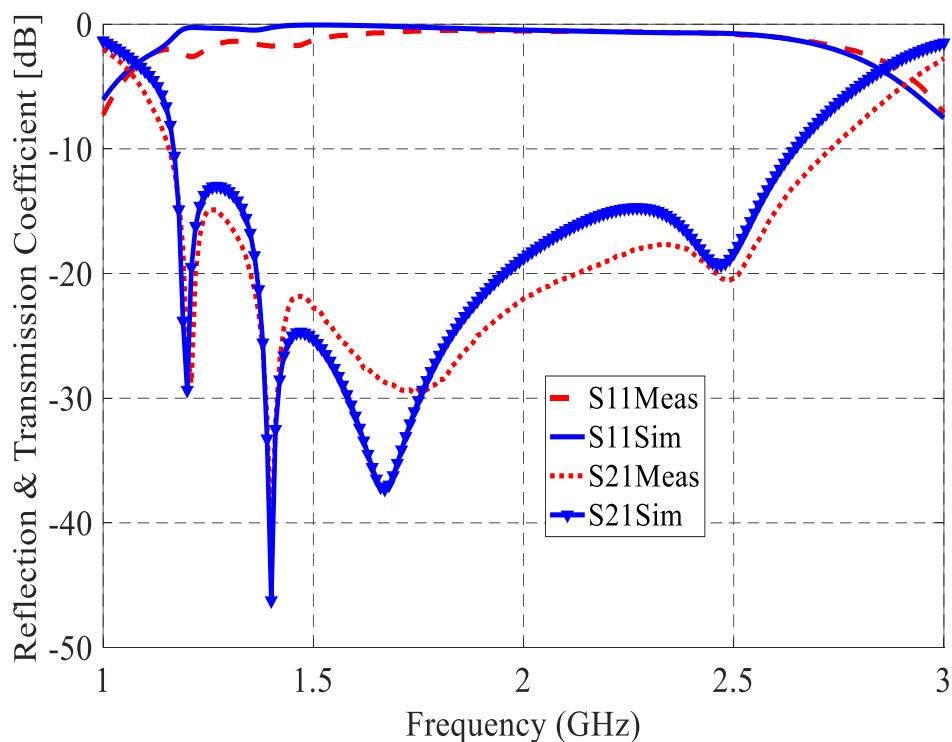

Figure 38: Simulated and measured response of the proposed log-periodic BRF built on a 0.25 mm-thick Rogers 3003substrate.

Table 10: Dimensions of the proposed log-periodic BRF designed on a 0.25 mm-thick Rogers 3003 substrate.

Parameter	Dimensions (mm)	Parameter	Dimensions (mm)
L	65	W_1	16.15
W	30	W_2	14.2
W_O	0.63	W_3	12.5
W_I	0.35	W_4	11
L_1	22.8	S_1	15.7
L_2	20	S_2	13.8
L_3	17.6	S_3	12.15
L_4	15.5	g	1.3

6.6. Proposed Sensor #3

The third sensor proposed in this thesis is a biologically inspired tunable octa-band reject filter which consists of a feed line on the top layer and eight slots embedded in the defect ground plane. These complementary resonators are oriented in such a way to produce multiple narrow bands instead of just one wide band. The eight stop bands are distributed between 1.5 GHz and 2.4 GHz and are separated by seven pass bands. These multiple bands are used to sense glucose variations.

As a first design iteration, only two slots are employed as illustrated in Fig. 39. These slots follow the distribution of the arms' ulnar arteries. Accordingly, the width of each resonating structure must relate to the diameter of the arteries. In [50], a research study conducted on 251 adult patients showed that the average diameter of the ulnar artery is 2.4 ± 0.4 mm for the right arm and 2.3 ± 0.3 mm for the left one. Furthermore,

the minimum diameters encountered for this artery are 1.3 mm and 1.5 mm for the right and left arms respectively. Based on that, the dimensions of the slots are optimized and are presented in Table 11. This structure exhibits a dual-band reject response as illustrated in Fig 40.
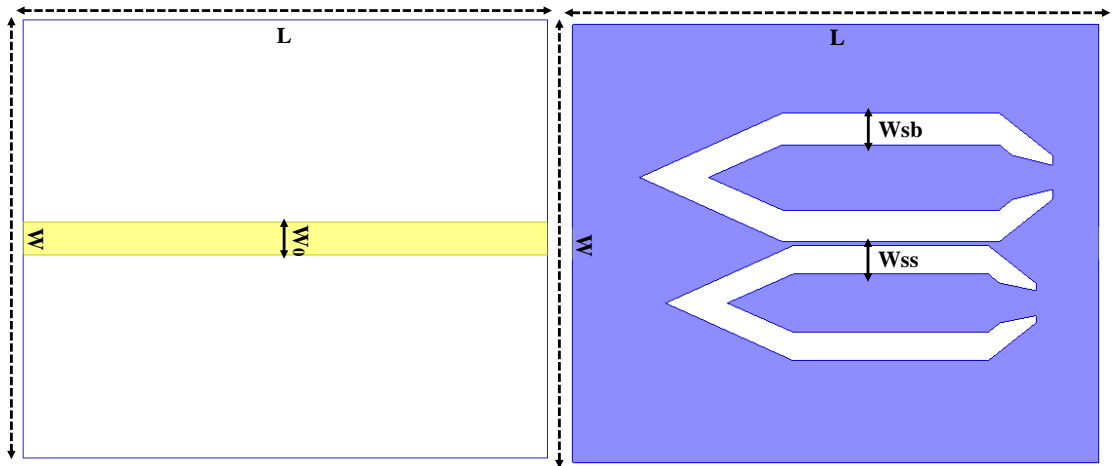
Figure 39: Top and bottom layers of the proposed dual-band reject filter.
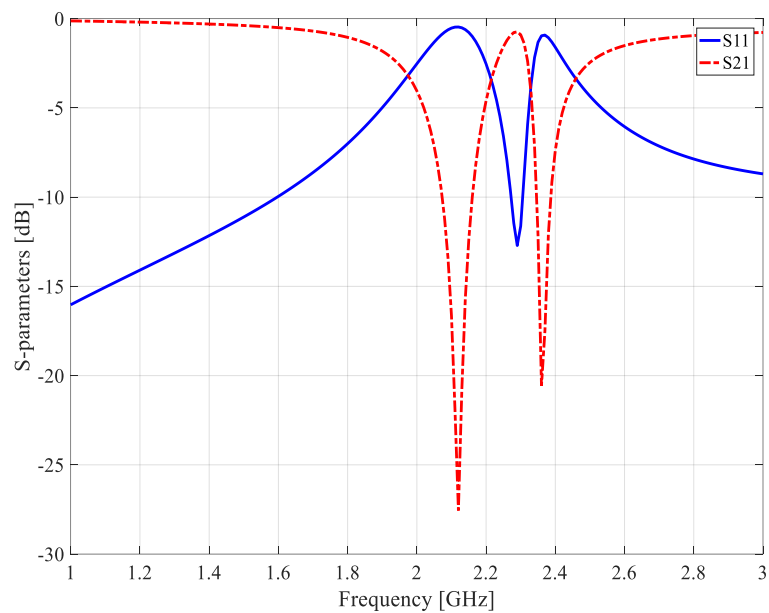
Figure 40: Response of the dual-band reject filter.

Table 11: Dimensions of the dual-band reject filter.

Parameter	Dimensions (mm)
L	30
W	25
W_o	1.9
W_{sb}	1.8
W_{ss}	1.6

6.6.1. Design Structure

To increase the number of bands, each slot is subdivided into four slots of equal width but different lengths. This configuration increases the number of resonances for the same physical size. Further increase in the number of slots within the same space (diameter of veins) would require decreasing the width of the slots below 0.18 mm, which makes the fabrication process quite complex. The length of each resonator is optimized to achieve the target resonant frequency. The modified ground plane structure is presented in Fig. 41. The same structure is superposed with the distribution of arteries of a human arm as shown in Fig. 42.
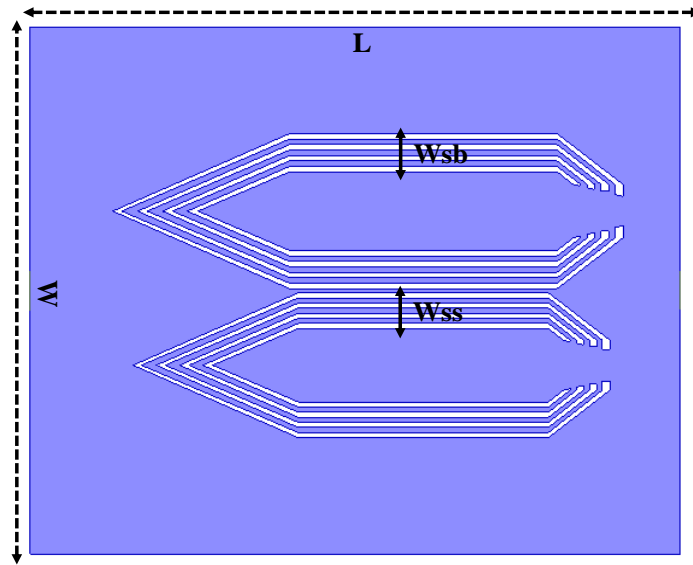
Figure 41: Bottom layer of the proposed octa-band reject filter.
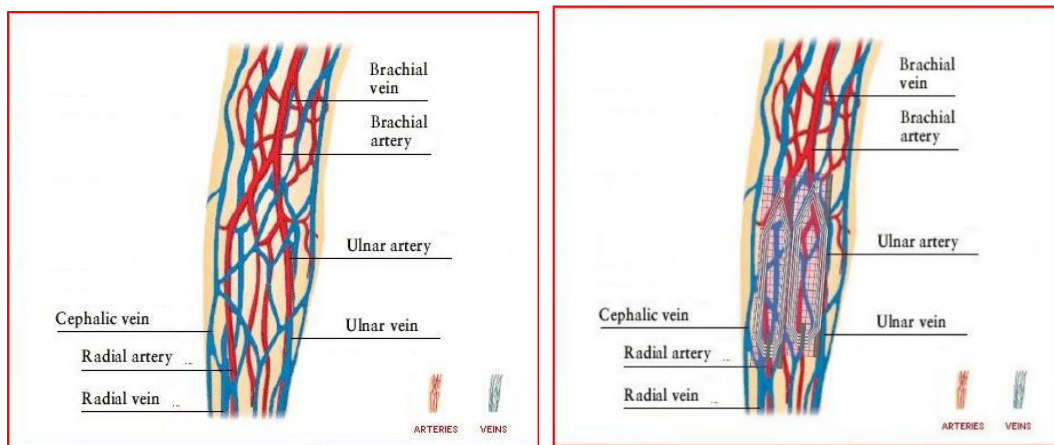
Figure 42: Proposed sensing structure superposed with the topology of the lower human arm.

The simulated response of the proposed structure using the previously used transmission line is shown in Fig. 43. From this figure, it is clear that the S11 level drifted apart from the desired 0 dB level, especially for higher frequencies. This could only mean that the regular 50 ohms transmission line is not suitable to feed the eight

slots. Accordingly, the challenge in this design is to provide a simple structure capable of efficiently feeding the slots in order to enhance the return loss levels. This is addressed by relying on two approaches.
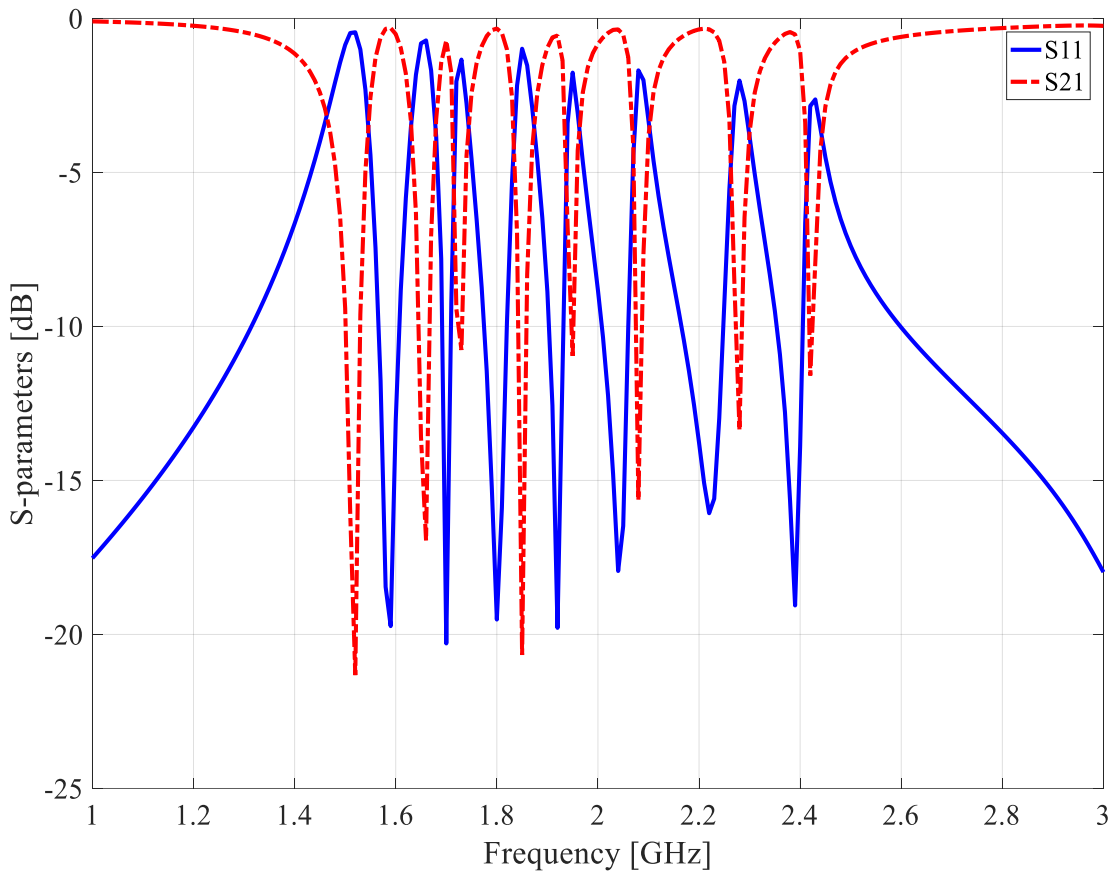
Figure 43: Response of the proposed octa-band filter using a regular 50-ohms transmission line.

The first approach is based on increasing the width of the transmission line from 1.9 mm to 3.4 mm as illustrated in Fig. 44. This is equivalent to decreasing the impedance of the line from 50 ohms to 35 ohm. The dimensions of the proposed structure are presented in Table 12. Using this topology the feedline is able to cover all the slots. This is essential to enhance the levels of the reflection coefficients.
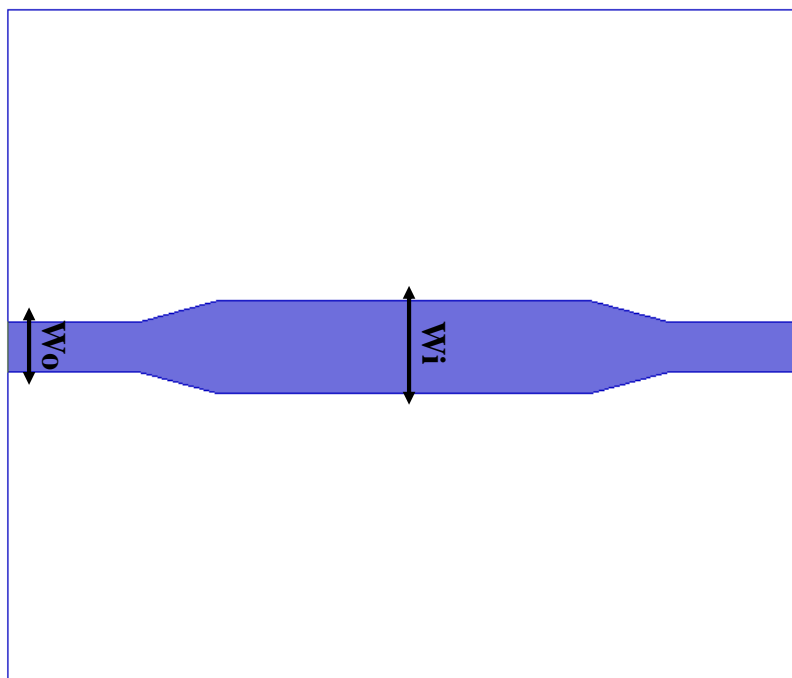
Figure 44: Tapered feeding line topology.

Table 12: Dimensions of the proposed tapered feeding line topology.

Parameter	Dimensions (mm)
W_o	1.9
W_i	3.4

Another topology used to enhance the response of the octa-band filter consists of implementing a rectangular resonator at the top layer near the transmission line as illustrated in Fig. 45. This resonator acts as a relay that receives the electric field from the 50 ohms line in order to feed the eight slots in the ground plane. The dimensions of this feeding network are presented in Table 13.
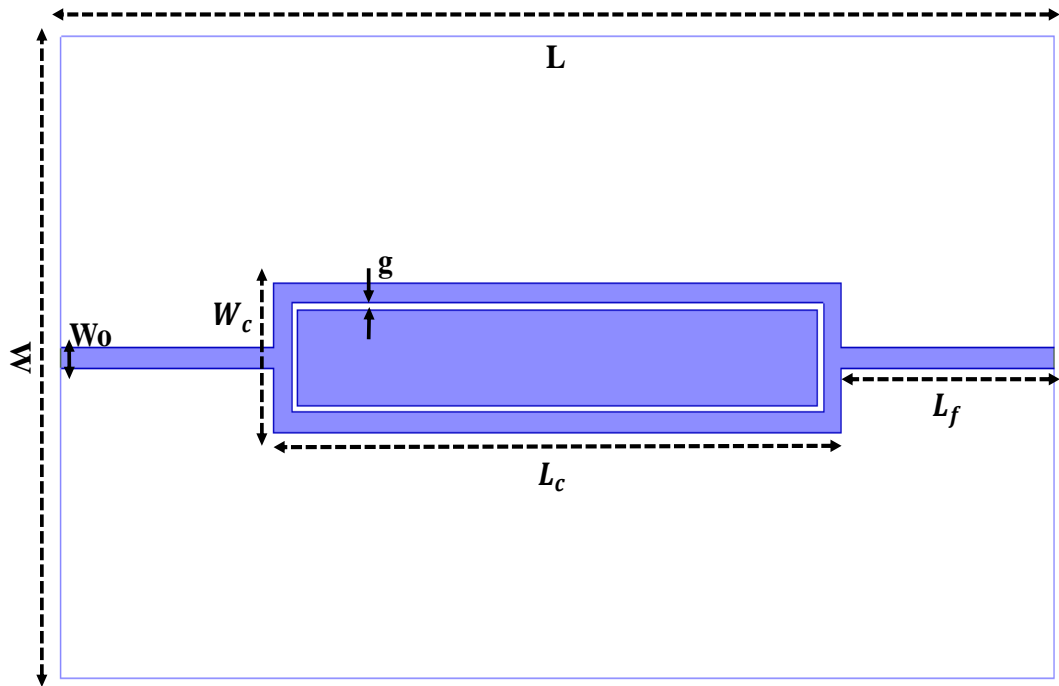
Figure 45: Proposed resonator-based feeding line topology.

Table 13: Dimensions of the proposed resonator-based feeding line topology.

Parameter	Dimensions (mm)
L	35
W	20
L_f	20
L_c	7.5
W_o	0.63
W_c	4.66
g	0.2

6.6.2. Sensitivity

The electric fields distribution of the two-slot structure and the proposed design are illustrated in Fig 46 at several resonant frequencies. This distribution proves that the proposed eight-slot configuration increases the electric field intensity of the structure. This is mainly attributed to the high density of the eight concentrated nested slots. In fact, each slot, on its own, contributes to a high field intensity at a specific frequency band. Some values of the electric field intensity for the octa-band structure are summarized in Table 14.
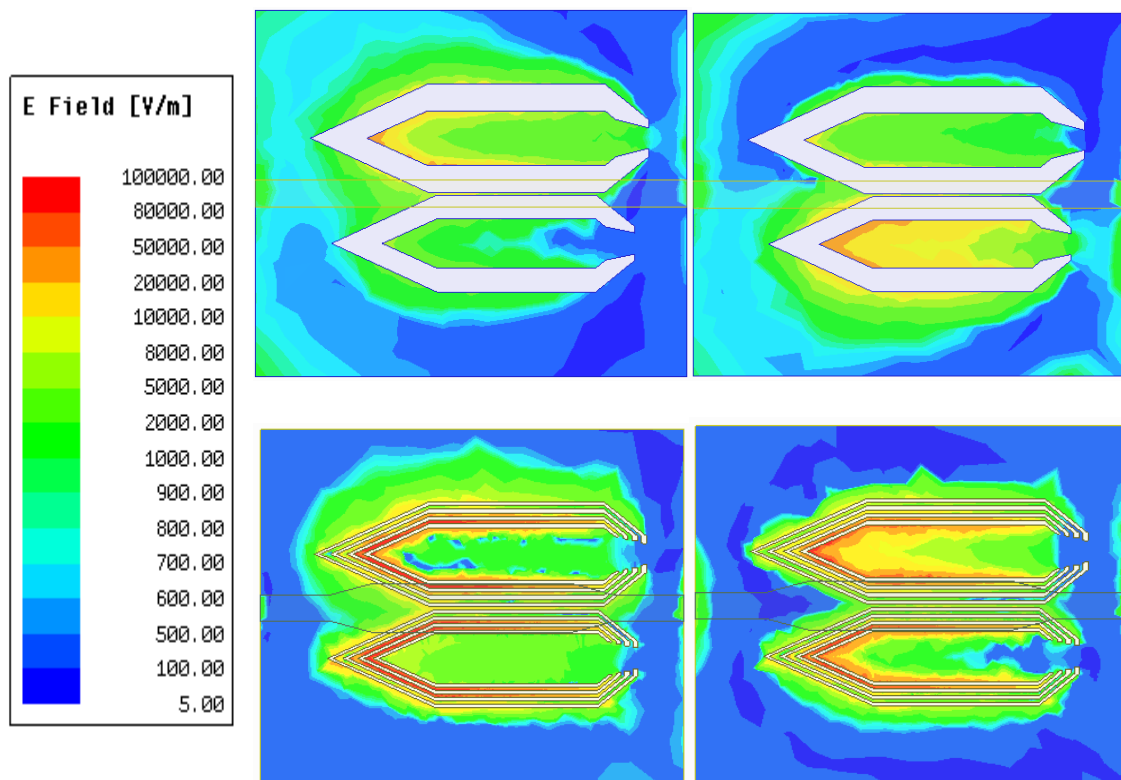
Figure 46: Electric field distribution of the dual-band at f= 2.12 GHz and f= 2.34 GHz and octa-band filters at f=1.8 GHz and 2.2 GHz.

Table 14: Maximum attained electric field intensity for the octa-band filters at different frequencies.

Frequency (GHz)	E-Field (V/m)
1.6	2.79×10^5
1.85	3.76×10^5
2	5.6×10^5
2.1	6.97×10^5
2.25	1×10^5
2.5	1.35×10^5

6.6.3. Performance

From an RF point of view, the performance of the octa-band filter can only be compared with some quint-band and sext-band filters implemented in wireless communication systems. The proposed methods suffer in simultaneously satisfying all the required design conditions. This is mainly attributed to the limited degrees of freedom in the design parameters. In some publications, researchers have worked on enhancing the system performance, but at the expense of large circuit sizes [51], or complex structures [52], [53] and [54] or both [55] as they usually rely on implementing a pair of resonators to generate each band. The characteristics and performance of several multiband filters and our proposed design are summarized in Table 15. Compared to the literature, the design developed in this work provides higher number of bands with comparable levels of S-parameters, using a simple and more compact configuration.

Table 15: Performance of different multi-band filters found in the literature.

	Bands (GHz)	IL (dB)	Bands / Resonator	Size (cm)
[51]	0.6/0.9/1.2/1.5/1.8	2.8/2.9/2.9/2.6/2.3	1	17.1x1.49
[52]	1.5/2.5/3.5/4.5/5.8	1.5/1.8/0.9/1.2/2.5	0.5	3.55x2.52
[53]	0.9/1.2/1.4/1.7/2/2.4	2.3/2/2.3/2.7/2.2/2	0.5	5.1x3.1
[54]	2.1/3/4/4.7/7.2	0.98/1.78/1.22/1.77/2.39	1	2.28x1.07
[55]	0.8/1.2/1.4/1.8/2.2/2.5	2.9/2.34/2.59/2.24/2.67/2.64	0.5	17.1x1.43
Proposed Design	1.55/1.66/1.75/1.84/ 2/2.15/2.3/2.4	<2 dB	1	2x1.5

6.6.4. Fabrication and Measurements

The first feeding topology is used to realize a prototype of the proposed octa-band filter on a 1.27 mm-thick Rogers 3006 substrate as shown in Fig. 47. The second feeding topology is used to realize a prototype of the proposed filter on a 0.25 mm-thick Rogers 3003 substrate as shown in Fig. 48. A good agreement between the simulated and measured scattering parameters is reached as shown in Fig 49 and Fig. 50.
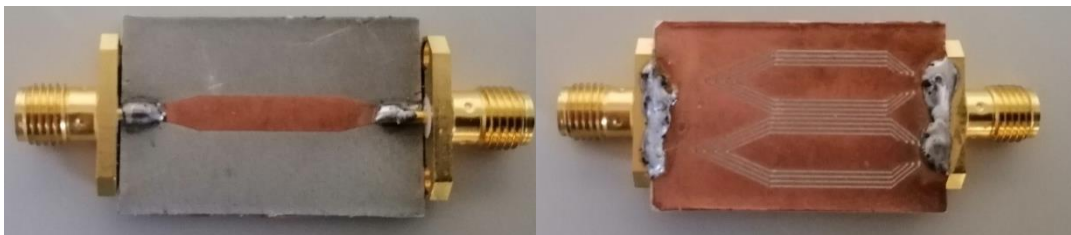
Figure 47: Top and bottom layers of a fabricated prototype of the proposed octa-band filter built on a 1.27 mm-thick Rogers 3006 substrate.
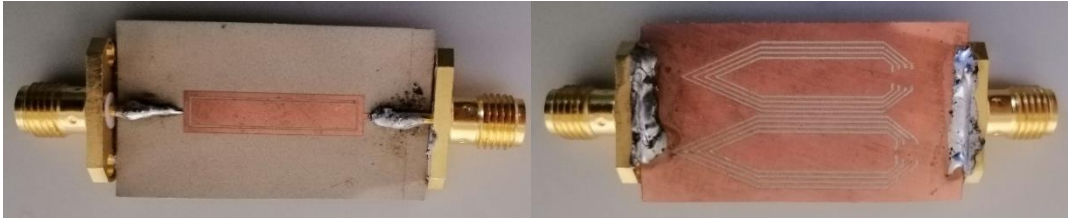
Figure 48: Top and bottom layers of a fabricated prototype of the proposed octa-band filter built on a 0.25 mm-thick Rogers 3003 substrate.

Figure 49: Simulated and measured response of the proposed octa-band reject filter built on a 1.27 mm-thick Rogers 3006 substrate.

Figure 50: Simulated and measured response of the proposed octa-band reject filter built on a 0.25 mm-thick Rogers 3003 substrate.

6.6.5. Tuning and Reconfiguration

The eight bands of the filter are reconfigured by implementing a varactor diode as discussed in this section.

6.6.5.1. Reconfigurable microwave circuits

Reconfigurable microwave circuits are multifunctional devices that have the ability to change their characteristics such as the frequency of operation, and are used in many applications that require agility and dynamic response. Reconfiguration is achieved using electronic components such as PIN diodes, RF- (Micro Electro Mechanical Switches) MEMS and varactors that are connected to the circuitry in order to change the electromagnetic behavior of the device. These electronic components change the electrical length of the RF structure by either redistributing the currents (PIN diode, RF-MEMS) or loading the structure by a variable capacitance (varactor). The change in the electrical length of the RF circuit causes a shift in the frequency of operation. The switch position and the biasing network are critical in order to achieve the best possible tuning.

For the proposed filter design, the equivalent circuit of the bottom layer is a parallel RLC resonator. This suggests that by adding a varactor diode between the internal and external metallic regions of the slots, the equivalent capacitance of the structure can be tuned. In practice this can be better achieved by placing the varactor diode on the top substrate side and connection to the bottom side through metallic vias.

6.6.5.2. Proposed tunable structure circuits

In the proposed design, the SMV 1705-079LF is used to reconfigure the operating frequencies [56]. Fig. 51 shows the spice model of the varactor. The values of the components are $L_s = 0.8$ nH, $R_s = 0.32$ ohms and $C_p = 0.5$ pF. The capacitance

value of the varactor diode C_j can be tuned from 31.5 pF to 5.2 pF, by varying the reverse voltage from 0 to 5 Volts. Biasing the varactor diode requires the use of an 470 nH inductor and a 10 pF capacitor. The basic function of the inductor is to prevent the RF signal from passing to the power supply, and the capacitor is used prevent shorting DC current.
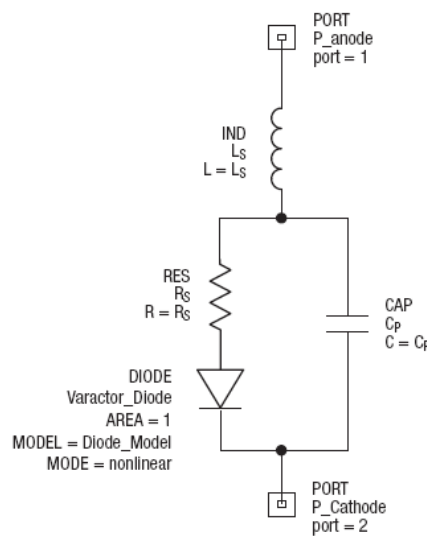
Figure 51: Spice Model of the SMV 1705-079LF [56].

The topology of the proposed tunable filter is represented in Fig. 52. It comprises the previously discussed eight slots etched in the ground plane beneath the feeding line, a varactor diode with a variable capacitance, an RF choke and a lumped capacitance for biasing. All the electrical components are soldered in the upper substrate side to prevent any interference with the sensing area. The varactor diode and the capacitance are connected in parallel and this combination is placed between the internal and external metallic regions of one set of slots using two vias. The Cathode of the varactor is connected to the power supply through the RF choke. The equivalent

circuit of this structure is demonstrated in Fig. 53. The fabricated prototype is presented

in Fig. 54, and the simulated and measured results are presented in Fig. 55.
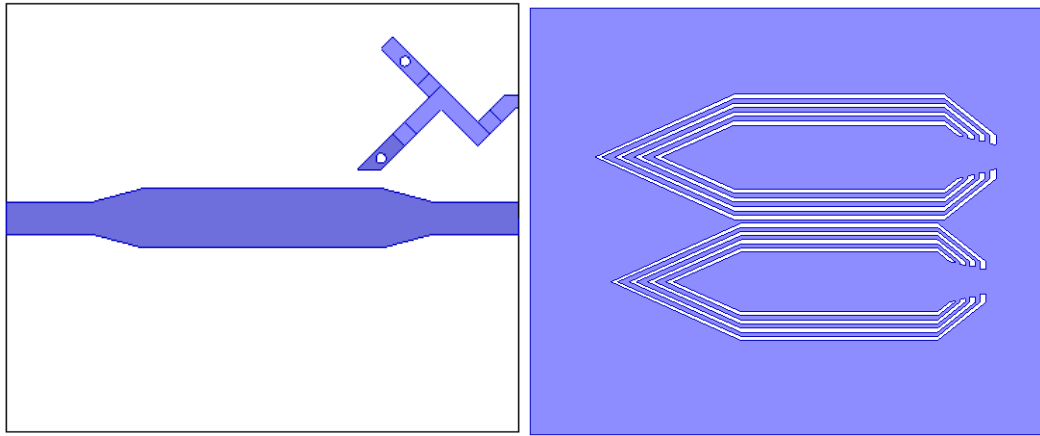
Figure 52: Topology of the proposed tunable filter.
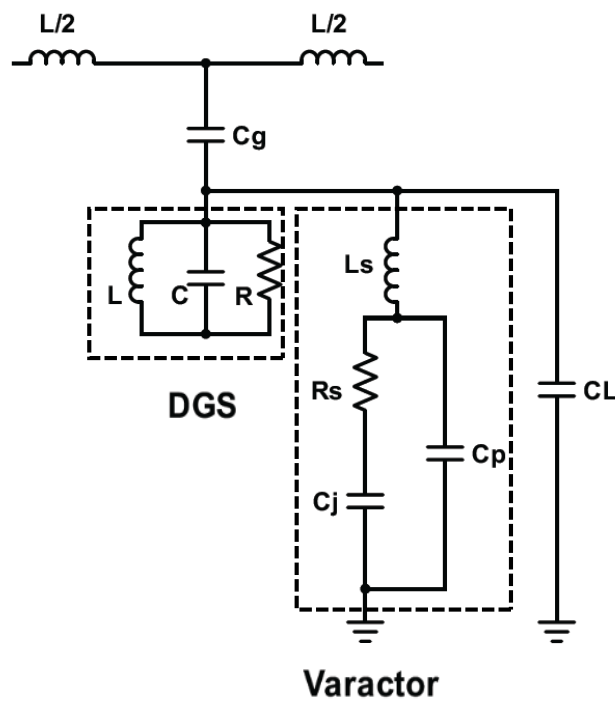
Figure 53: Equivalent circuit of the proposed tunable filter.
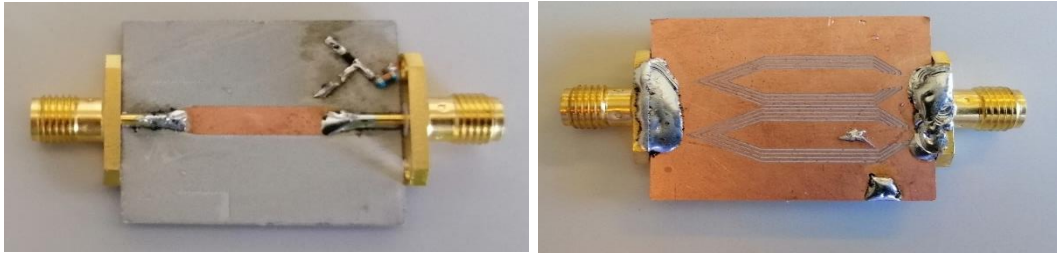
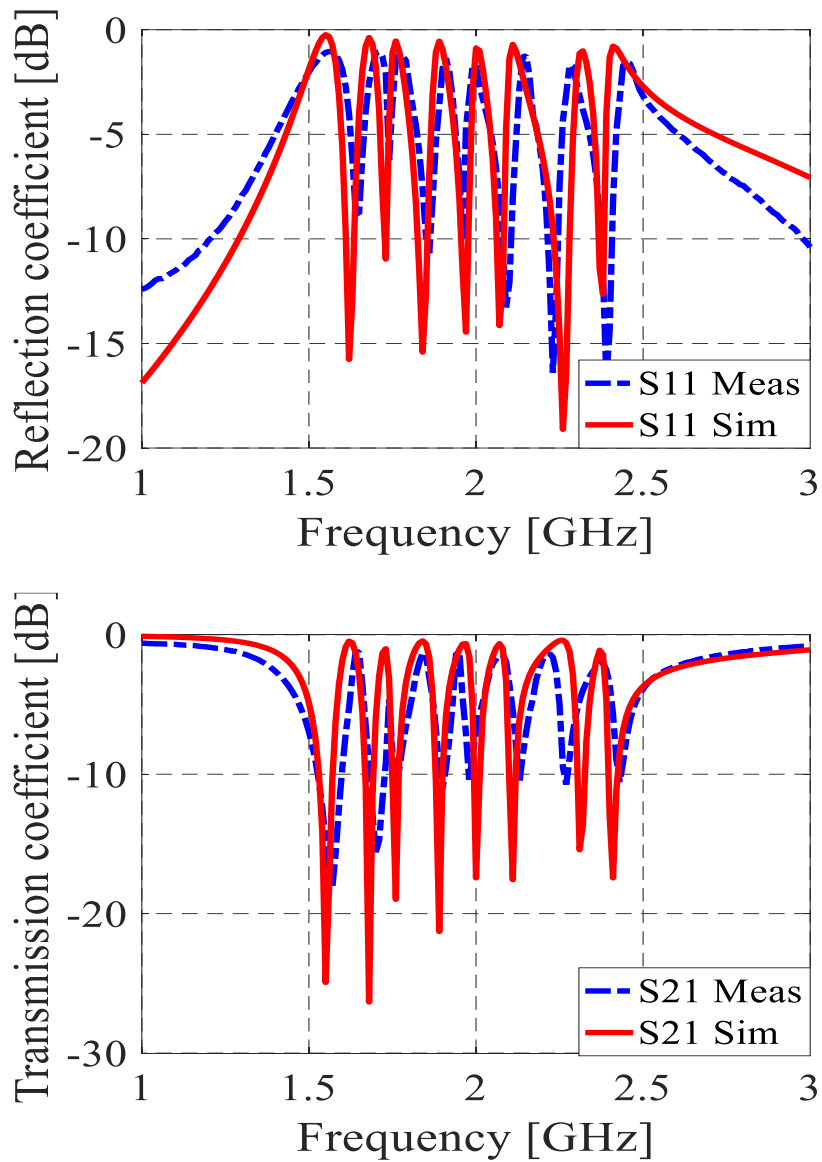Figure 54: Fabricated Prototype of the proposed tunable filter.
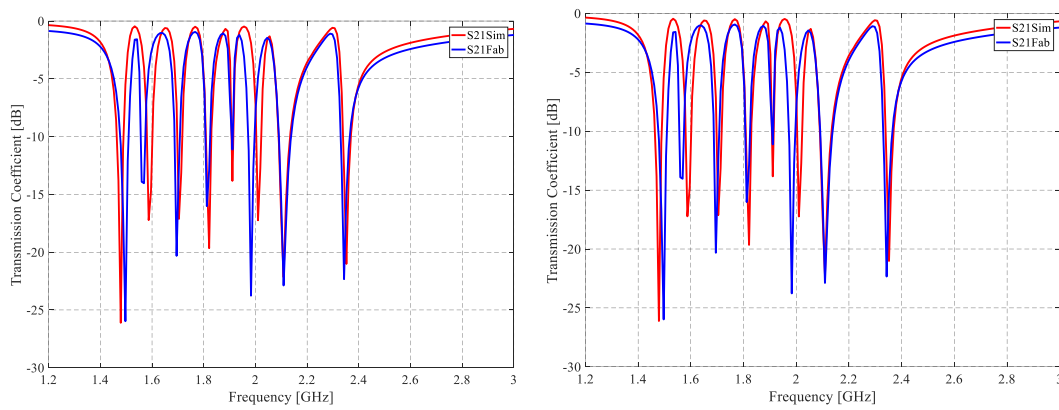
(a)
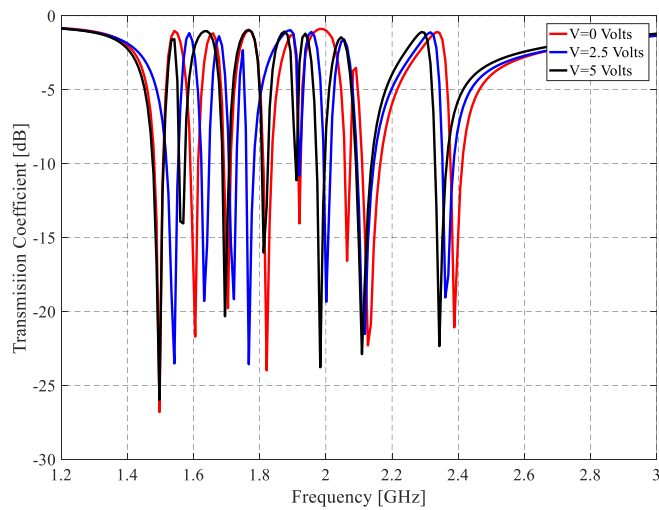
(b)

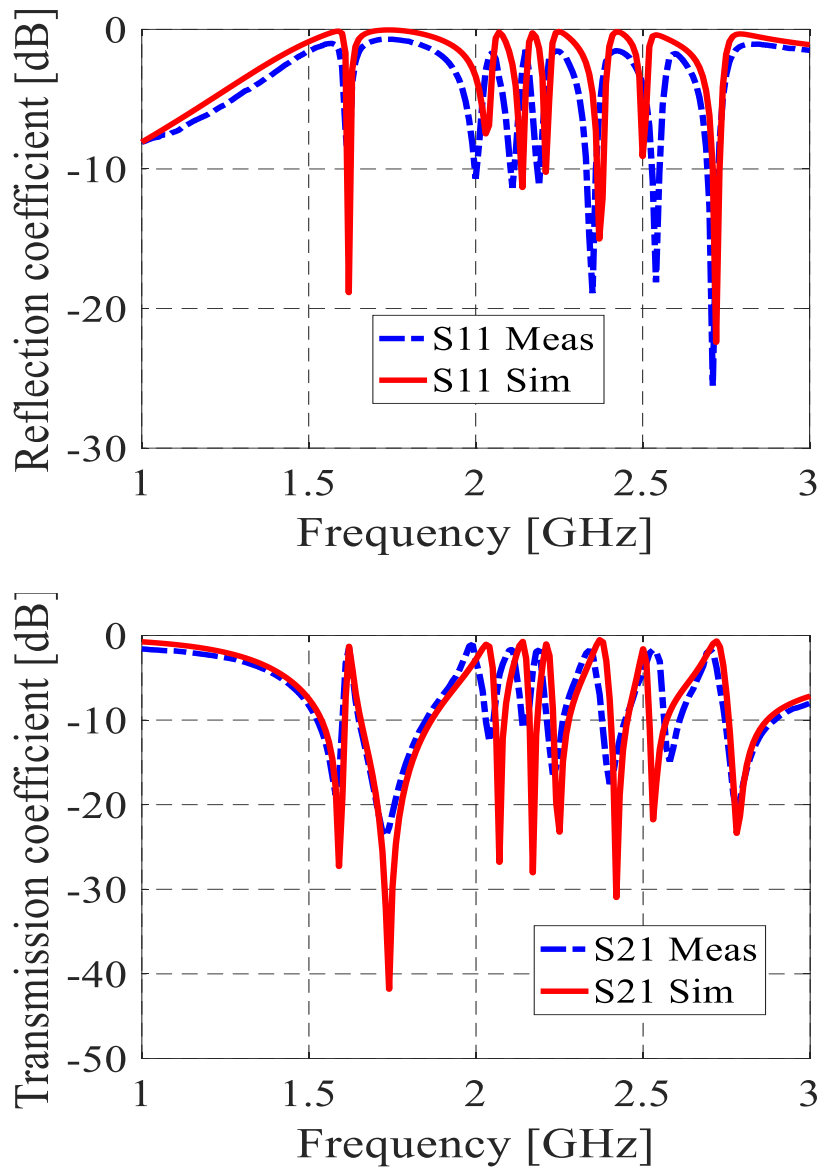Figure 55: Simulated and measured response of the proposed reconfigurable octa-band reject filter built on a 1.27 mm-thick Rogers 3006 substrate. The transmission coefficient is shown for a) V=0 Volts, b) V=5 Volts and c) several voltage values.

6.7. Discussion

This chapter presents the design of three different RF filters. These circuits are initially designed using HFSS and then built on a variety of flexible and rigid substrates. The performance of these filters as glucose sensors is assessed by monitoring their E-field distribution over the sensing area. It was noted that the octa-band filter achieved the highest E-field intensity, followed by the broad-band filter. The reflection and transmission coefficients of the different filters were also validated by measurements.

CHAPTER 7

SIMULATION AND MEASUREMENT OF THE PROPOSED EM-BASED GLUCOSE SENSORS

7.1. Introduction

This chapter presents the simulation results of the proposed RF sensors along with the measurement results for in-vitro and ex-vivo and in-vivo studies. Simulation results include the integration of both a single and multi-layered tissues model. For in-vitro measurements, serum is used to mimic the blood. For ex-vivo studies, rat tissues are placed as a separation between serum and the sensor. Finally, for in-vivo studies, OGTT is performed twice for six different patients.

7.2. Simulation

To investigate the ability of the filters to perform as glucose meters, several human tissue models were considered for analysis. The common act in these simulations is to vary the relative permittivity of the blood layer, so that it corresponds to the change of the BGL. For the simplest single-layered model, blood is modeled as a rectangular box of height h=4mm placed at a distance of 2 mm from the sensing area of the filter. Rectangular shapes are utilized for purposes of reduced simulation time. A more complex model is the one shown in Fig 56. It includes the main biological layers encountered in a human arm: skin, fat, blood, and bones. The thickness of each of these four layers is presented in Table 16. This model was placed 4.4 mm away from the

sensing area of the filter, meaning that the blood layer is distanced by 7.4 mm away

from the sensor.
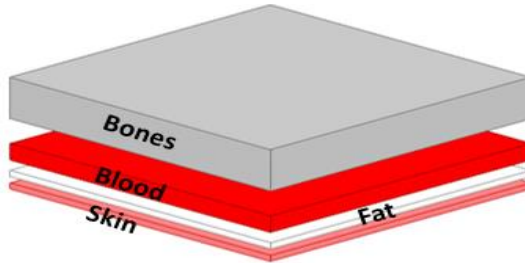
Figure 56: Multi-layered human tissues model.

Table 16: Thickness of the layers used in the model.

Layer	Height (mm)
Skin	1.5
Fat	1.5
Blood	4
Bones	10

Placing these layers as superstrates near the sensors causes a shift in the

operating frequency of the device under test. When analyzing the device response, we

sweep the dielectric constant of the blood layer from 60 to 75 to reflect some variations

in the BGLs. The S21 responses of the sensors for the different values of the dielectric

constant are presented in Fig. 57. These include the results for both cases of the device

loaded by the single-layered and multi-layered models. The S21 phase and magnitude

variations of the proposed sensors, when loaded by the multi-layered model, are

illustrated in Fig 58 at one of the operating frequencies. It is worth noting that similar

trends were obtained at other operating frequencies (not illustrated here).

74

Figure 58 demonstrates a linear and monotonic behavior for the proposed

sensors in response to the variations in relative permittivity; the sensors' responses

exhibit a clear correlation with the material's dielectric constant. For the SRR-based

filter, this behavior is restricted to the narrow operating band. For the broad-band filter,

this linear trend is observed over a wide range of frequencies especially between 1.75

GHz - 2.75 GHz. In the case of the multi-band filters, the linear behavior is observed

around all the resonant frequencies. Based on the observed trends, we find that the

performances of the broad-band and octa-band sensors to be very favorable for purposes

of glucose sensing applications. Furthermore, their sensitivity can be sampled across

several frequencies in comparison to narrowband filters. Accordingly these two sensors

are considered for further analysis as discussed in the following sections.

7.3. Experimental Setup

The proposed broad-band and octa-band sensors are tested in in-vitro, ex-vivo

and in-vivo scenarios. The basic experimental setup consists of three elements, a

portable vector network (VNA, N9914A, Keysight Technologies), RF cables and a

sensor. The VNA applies to the sensor an RF signal whose frequency is swept over a

predefined frequency range with an output power of about -15 dBm. For each

frequency in the specified range, the VNA measures the reflected signal at both ports of

the sensor along with the transmitted signal between the two ports. The changes in the

microwave parameters such as resonance frequency, reflection coefficient and insertion

loss are then tracked using an algorithm. The S-parameters data is represented using smith chart formats, and is collected in Cartesian forms.

(a)

(b)

(c)
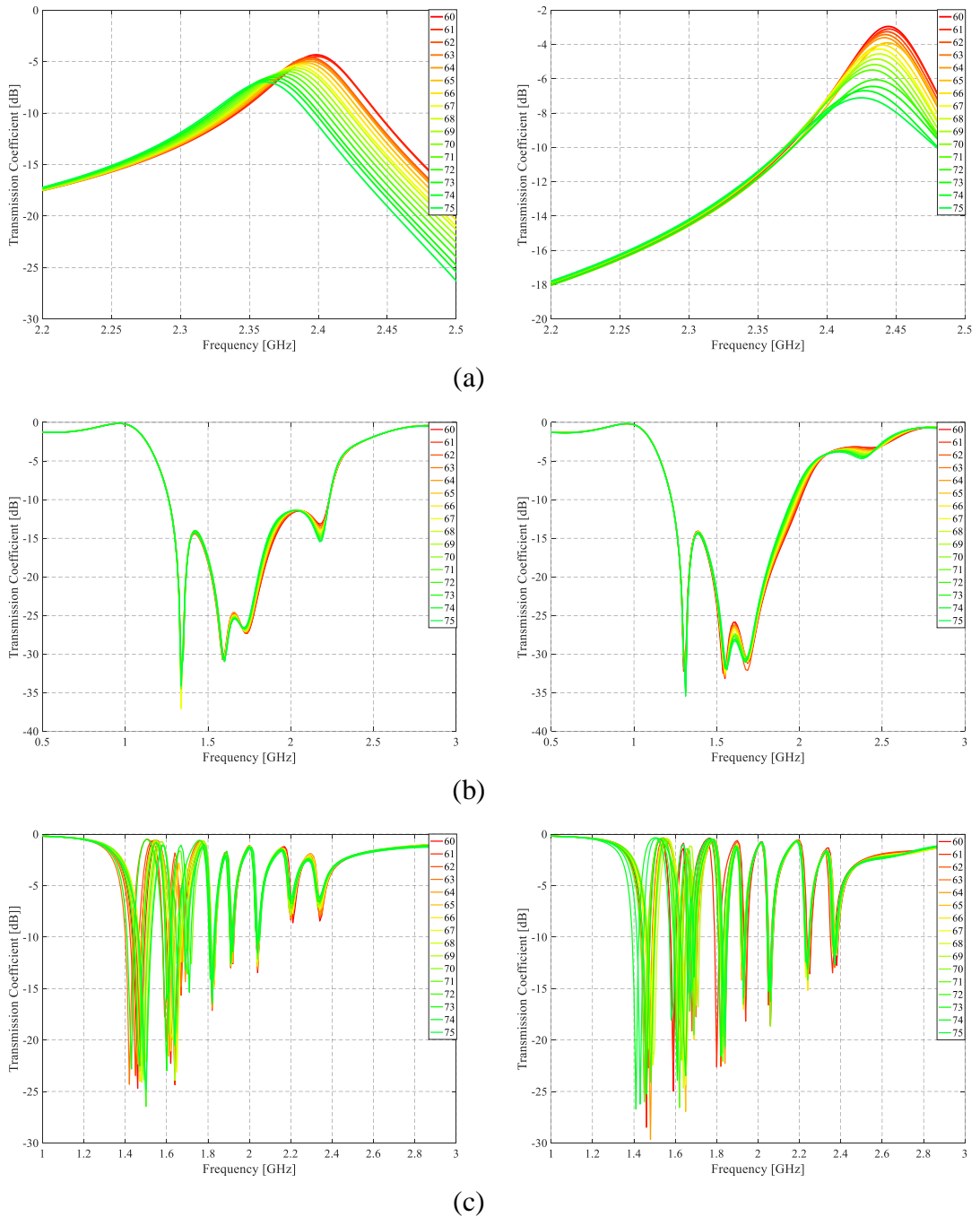
Figure 57: S21 response of the proposed sensors for the single-layered (left) and multi-layered models (right), a. narrowband sensor, b. broad-band sensor, c. octa-band sensor.
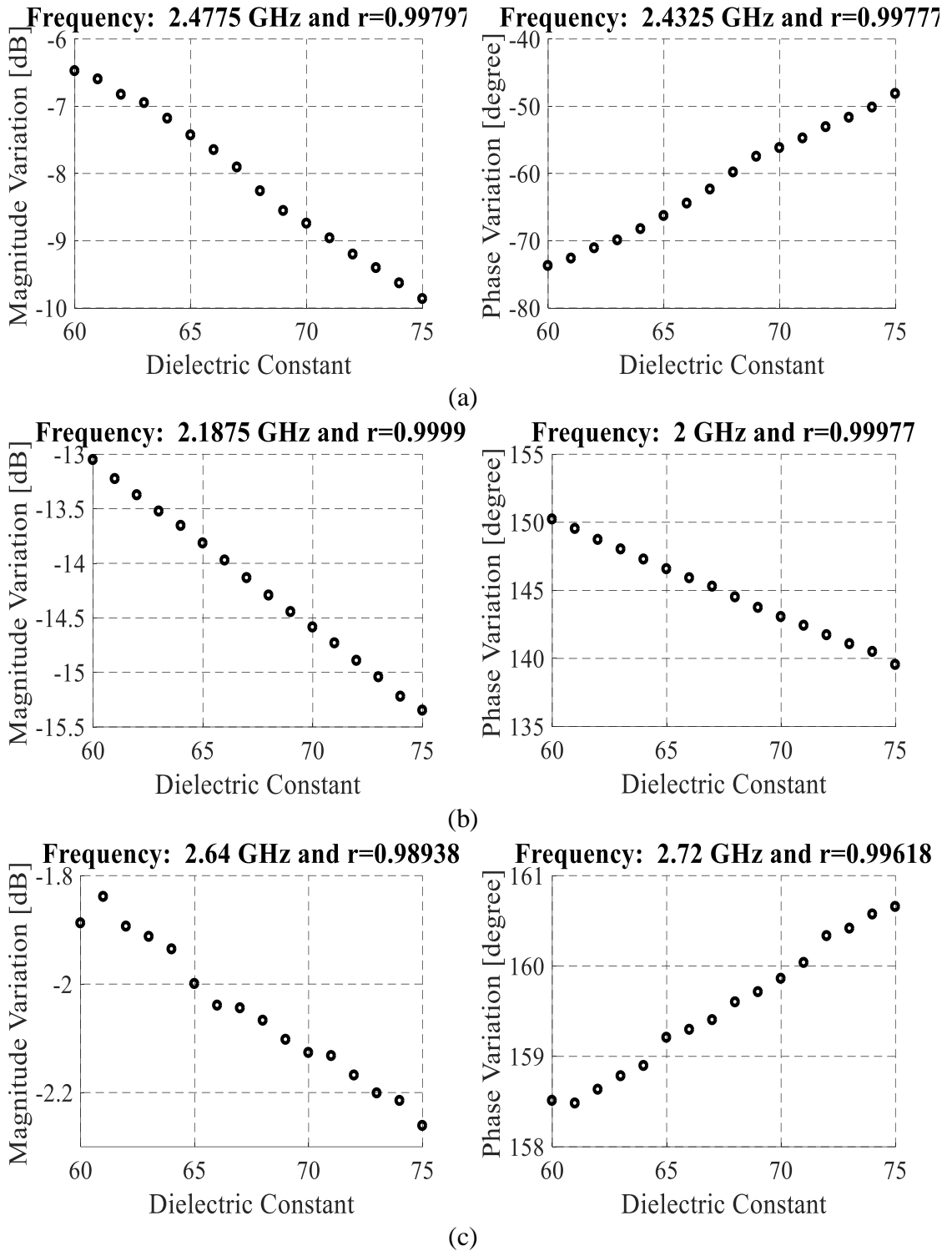
Figure 58: Magnitude and phase variation of the proposed sensors when loaded by the multi-layered model, a) the narrowband sensor, b) the broad-band sensor, and c) the octa-band sensor.

At each frequency, ten different measurements and hence microwave data points are obtained from the VNA and their average is reported in order to minimize noise effects and reduce the randomness in the measurements. The same process was repeated for three different experiments.

- For the first experiment, the sensor is calibrated to monitor variations in glucose inside a foam container filled with 7 mL of serum whose glucose density is being varied gradually.

- In the second experiment we introduced rat tissue as a separation layer between the serum and the sensor.

- Finally, in the third experiment we tested the ability of the sensors to detect variations in human BGLs. This experiment was conducted for six different volunteers.

7.3.1. Serum Measurements

We propose for our setup placing a fixed, serum-filled foam container on top of the sensor as shown in Fig. 59. Serum is a liquid that is similar in composition to the blood plasma; however, it excludes the clotting factors of blood. Dextrose powder is then added to the solution to alter the glucose concentrations. The considered experimental procedure consists of extracting part of the liquid, adding dextrose, applying vortex mixing to accelerate the dissolving process, adding the mixture to the container, manually mixing the whole solution, and finally wait ten minutes to ensure a homogeneous entity before reading the S-parameters. This process ensures that the

setup and volume of the serum remains almost fixed during the whole experiment, while the glucose level is incremented gradually.
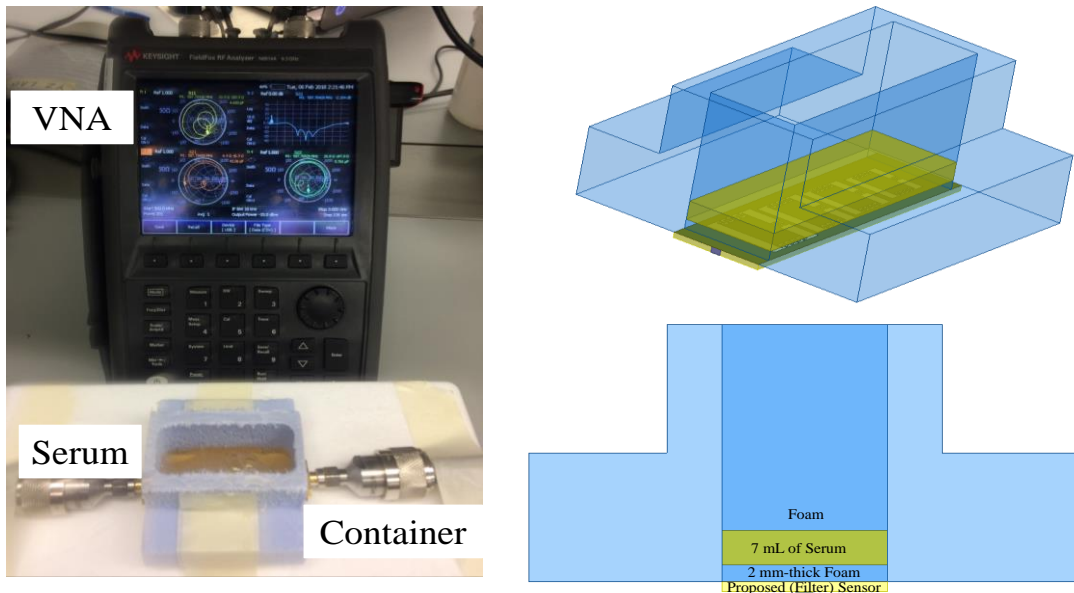
Figure 59: Experimental setup for serum measurements.

As a first test, baseline measurements were performed. This was conducted by measuring the sensors' S-parameters in the absence of the foam container, then by placing an empty container on the sensor, and finally by filling the container with serum. From these measurements, it was verified that the sensors under test maintain their free space responses, with and without the empty foam container. The shift in frequency occurs only when serum is added.

The response of the proposed sensors for different glucose concentrations is shown in Fig. 60. Their response displays a clear correlation with glucose levels at different frequencies as illustrated in Fig. 61 for the broad-band and in Fig. 62 for the octa-band sensors.

79
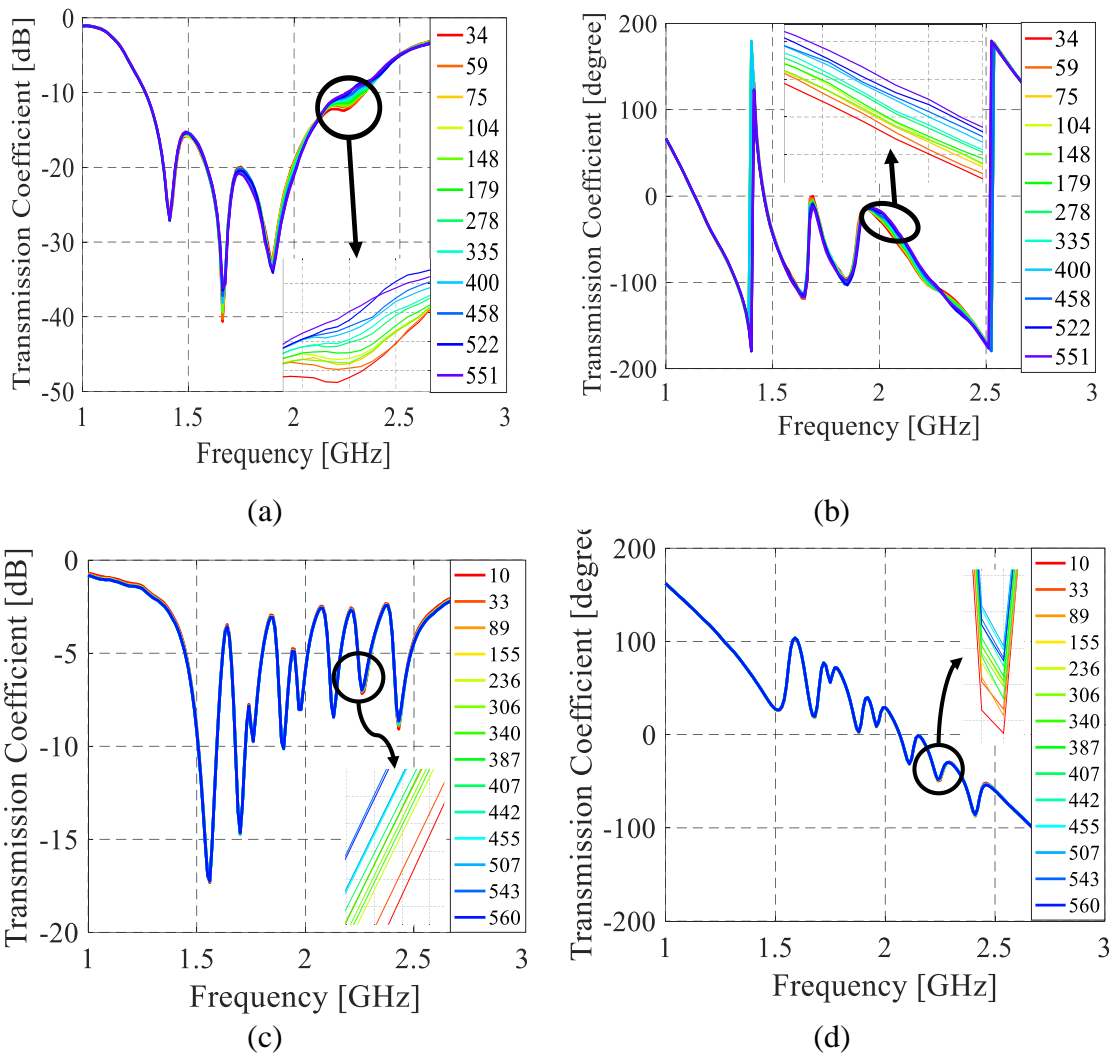
Figure 60: Response of the proposed sensors for different glucose concentrations, a) S21 magnitude of the broad-band sensor, b) S21 phase of the broad-band sensor, c) S21 magnitude of the octa-band sensor, d) S21 phase of the octa-band sensor.

Figure 61: Correlation between the response of the broad-band sensor and the glucose concentrations at different frequencies.
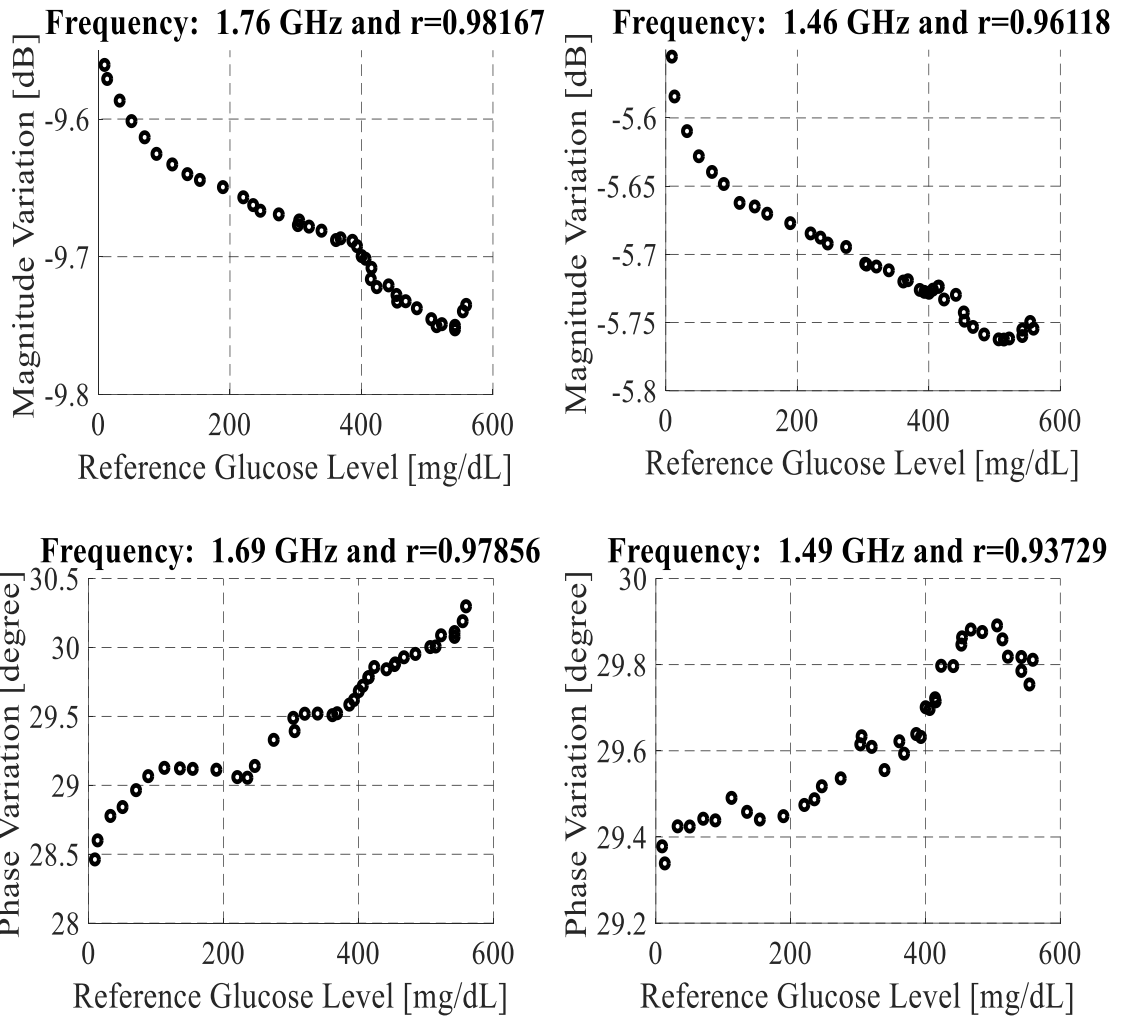
Figure 62: Correlation between the response of the octa-band sensor and the glucose concentrations at different frequencies.

7.3.2. Animal Tissues and Serum Measurements

The setup of this experiment is almost identical to the one presented in the previous section. The same foam container was considered, and glucose levels were varied in the exact fashion. The only difference is that now the serum-glucose solution is being tested in a multi-layer setup, where the animal tissues separate the sensor from

the liquid. The magnitude and phase variations are shown in Fig. 63, and it's clear that

the linear correlation is still maintained.
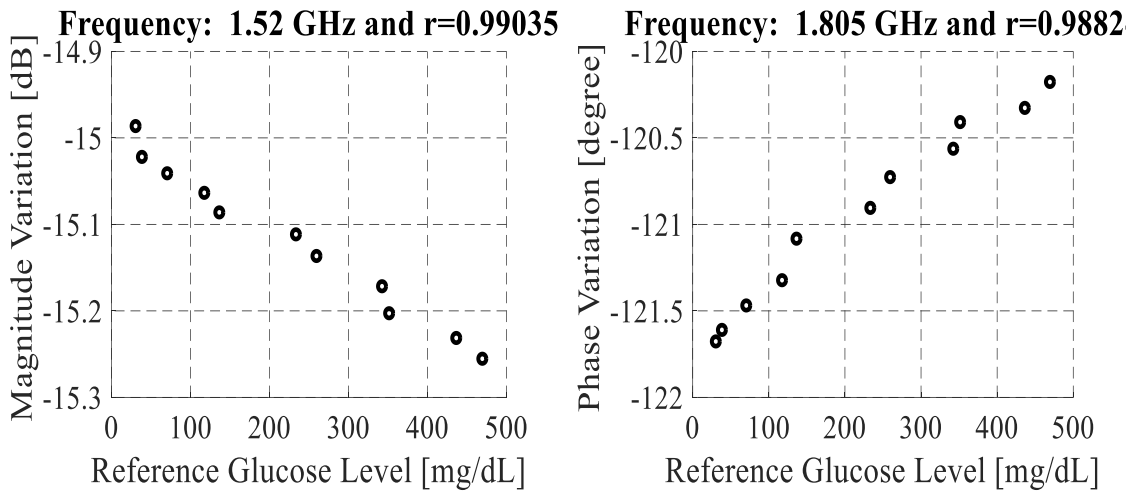
(a)
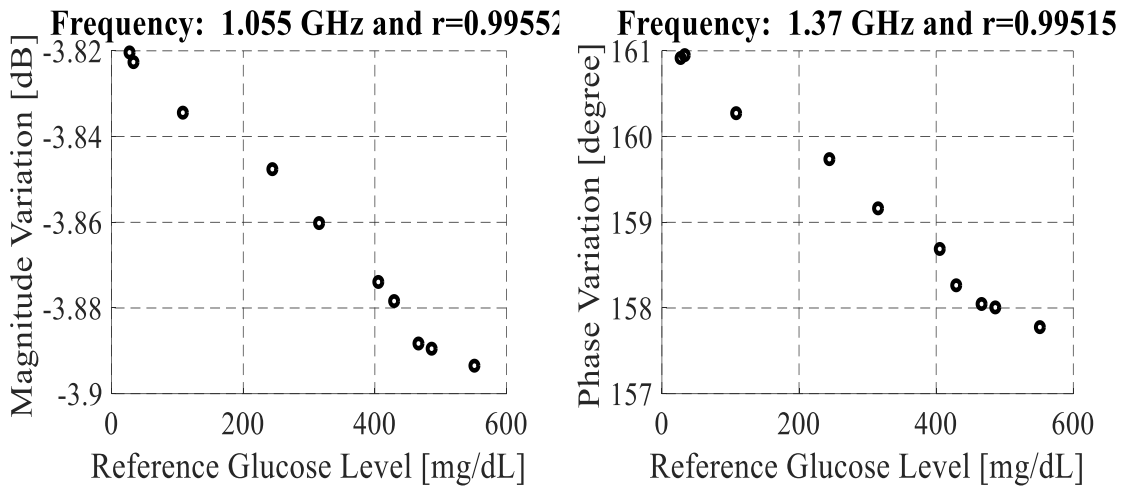
(b)

Figure 63: Magnitude and phase variations of a) broad-band, and b) octa-band sensors.

7.3.3. Clinical Measurements

7.3.3.1. Study design

Subjects were recruited to participate in the clinical trial after signing a consent form, previously approved by the Institutional Review Board.

7.3.3.2. Study subject

Subjects were considered eligible for the study if they were between 18 and 70 years of age, and able to provide informed consent. There were no restrictions on either race, sex or ethnicity. Substance abuse, lactation, pregnancy, and being part of an interventional trial were the exclusives criteria. In phase one of the study, only healthy subjects with HbA1c levels less than 6%, normal blood pressure and no sign of dyslipidemia were included.

7.3.3.3. Procedure

The patients arrived to the clinical study unit in the morning after fasting for at least 8 hours. Measurement of the blood glucose levels was initially performed using the standard techniques that assess glycemia, using a glucometer of ACCU-Check. Afterwards, the sensor under test was attached to the lower arm of the volunteer as illustrated in Fig. 64. Subsequently, glucose was orally ingested as a concentrated glucose drink that contains 75 g glucose dissolved in 200 mL of water. This induces a hyperglycemic excursion to a target BGL of 170 -220 mg/dL. These levels are expected to fall back within 2 hours. Readings from the sensor were collected each 5 min, and

reference BGLs were measured at intervals of 15 minutes using the glucometer. During the process, patients were asked to stay tranquil and with no physical movements. The room temperature was 23 ± 0.5 ∘C.
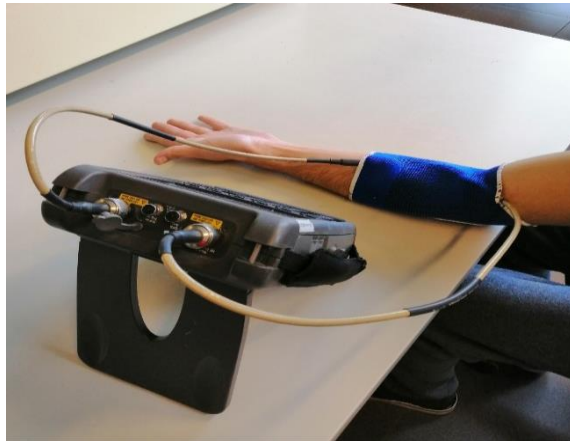
Figure 64: Clinical trials setup.

7.3.3.4. Results

The response of the proposed sensors showed a clear correlation with the BGLs as demonstrated in Fig. 65 and Fig. 66 for all the patients. The solid red line represents the reference glucose levels, and the dashed blue line represents the normalized response of the sensor at one frequency. Moreover, we note that for a given patient there was a clear correlation between the response at some specific frequencies and the glucose levels not only for the first OGTT but also for the second test as demonstrated in Fig 67.

Furthermore, a statistical prediction model was generated on the basis of the sensor signals collected during the two visits of the volunteers and is discussed in the next chapter.
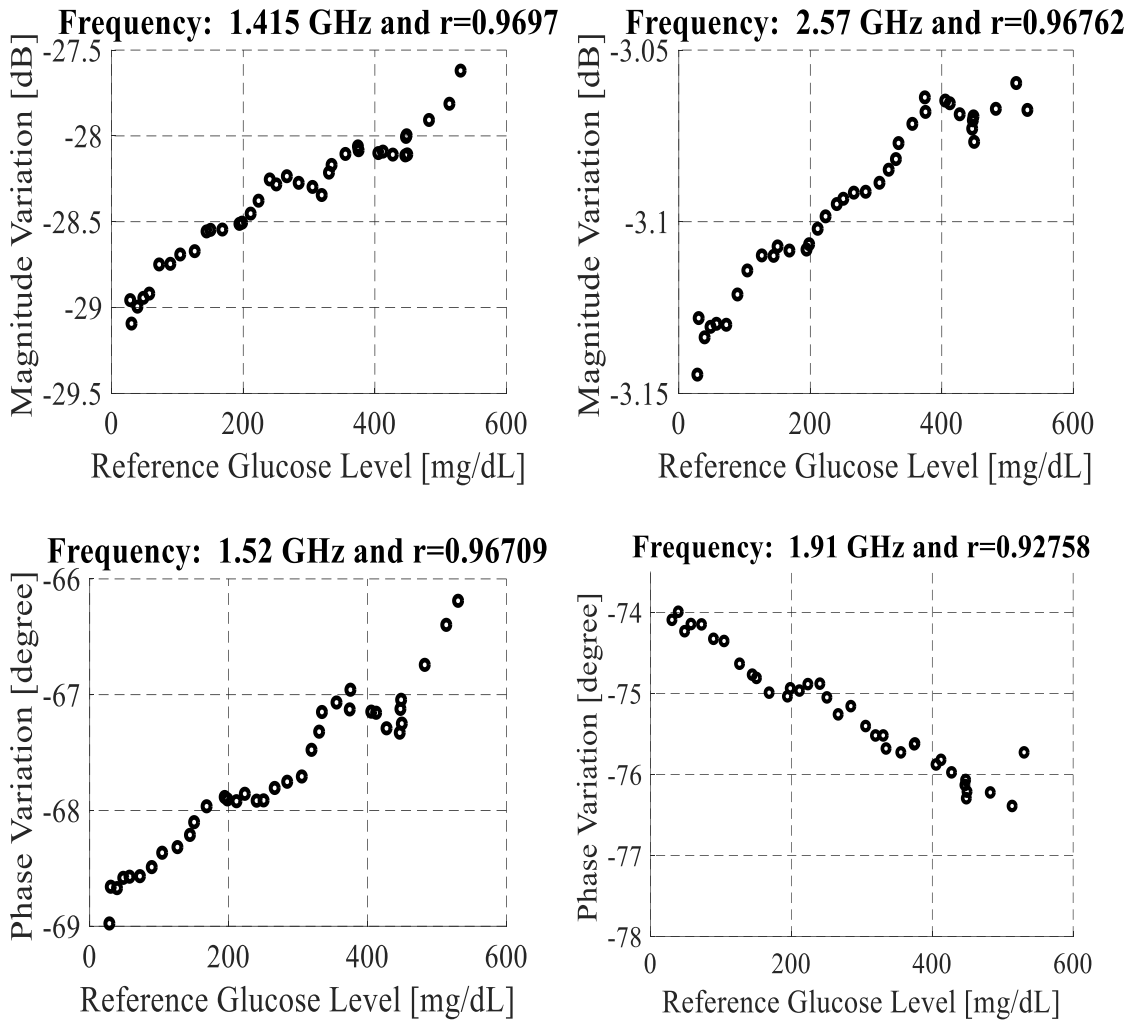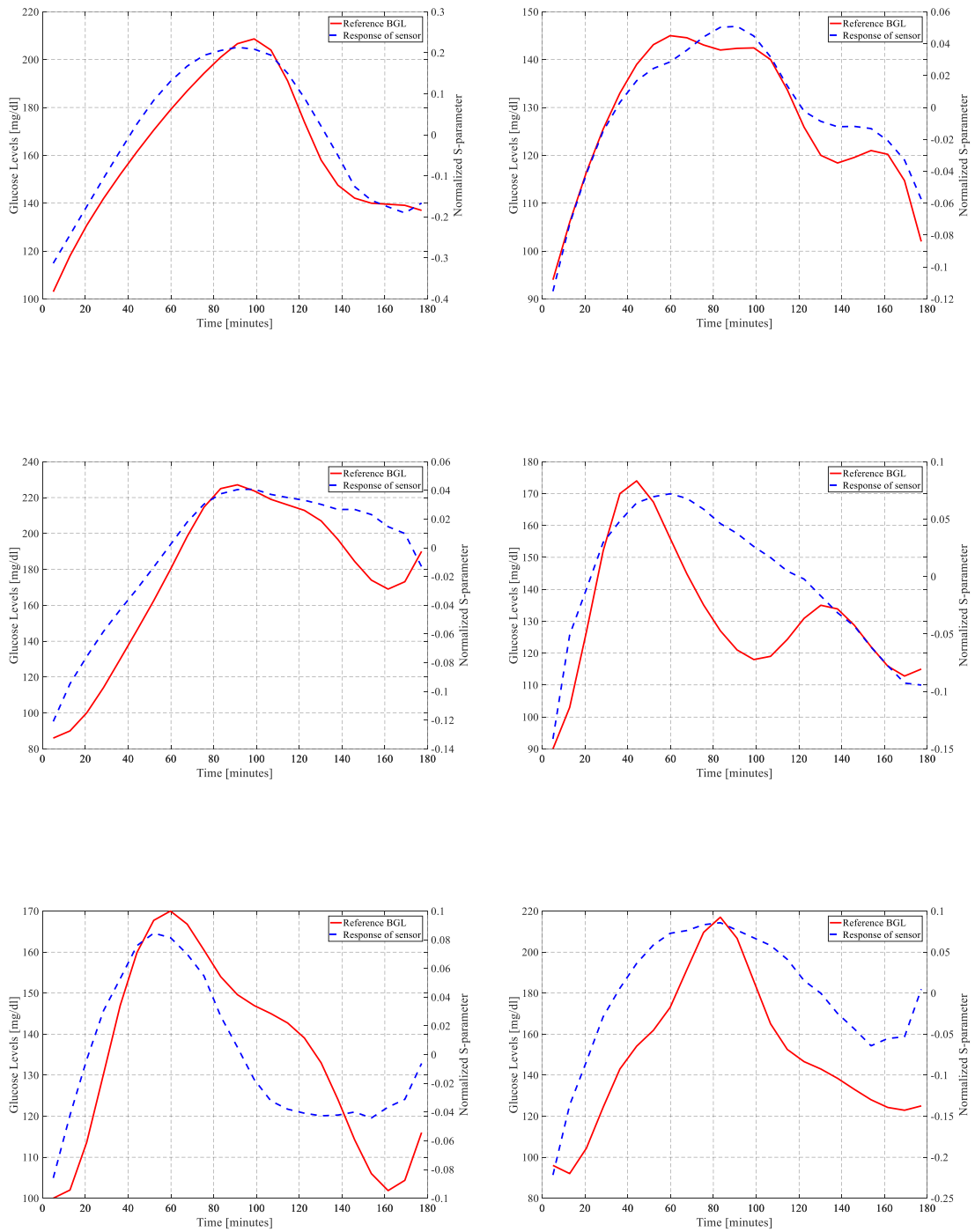
Figure 65: Correlation between the response of the broad-band sensor and the blood glucose concentrations.
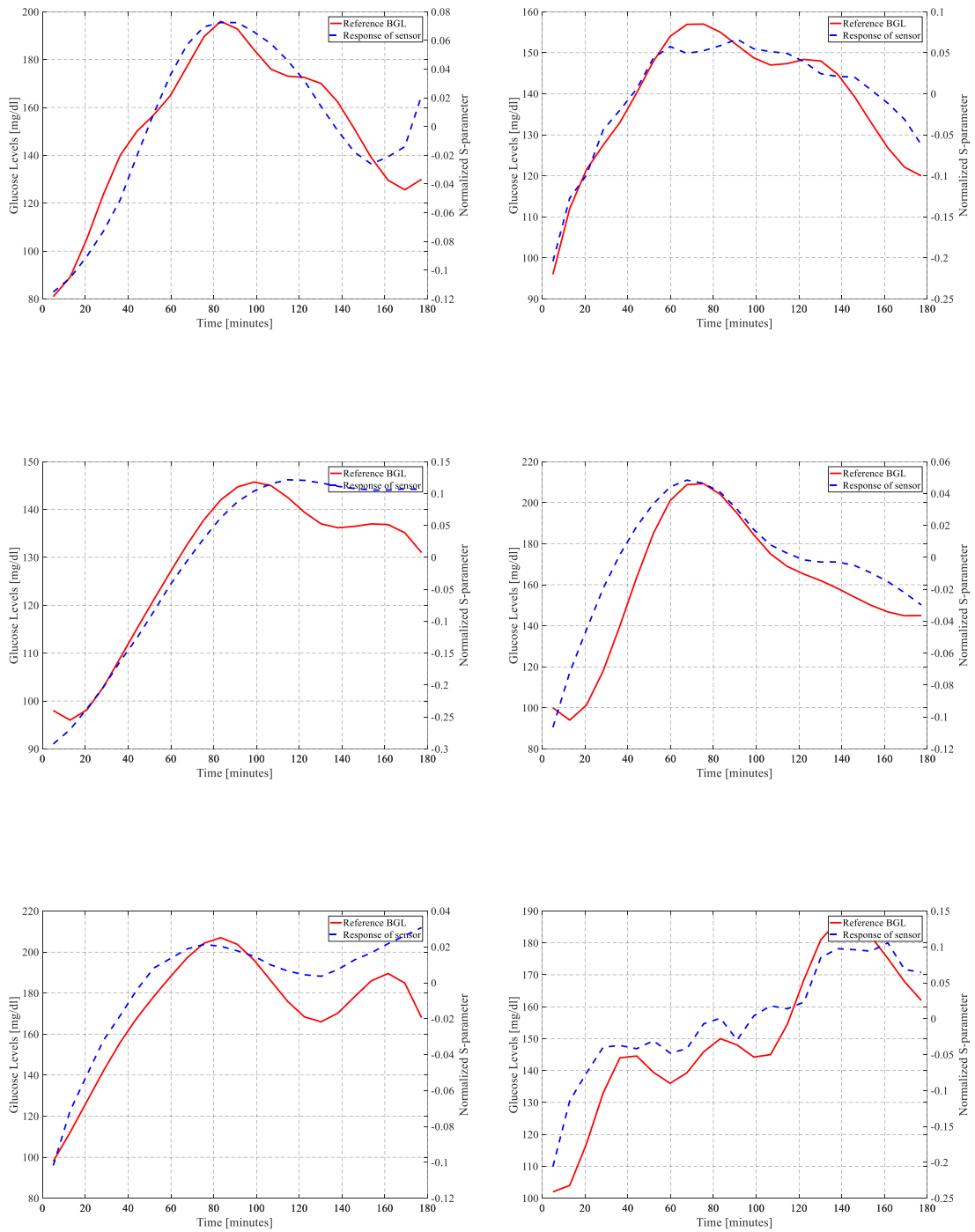
Figure 66: Correlation between the response of the octa-band sensor and the blood glucose concentrations
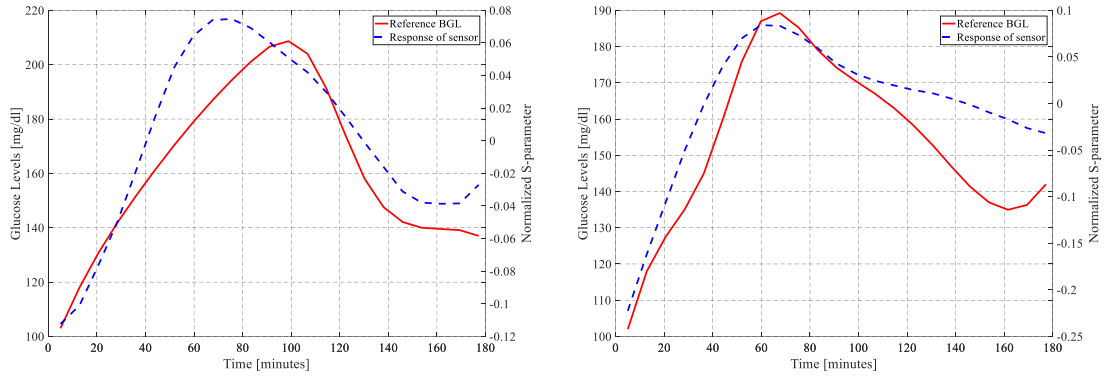
(a)
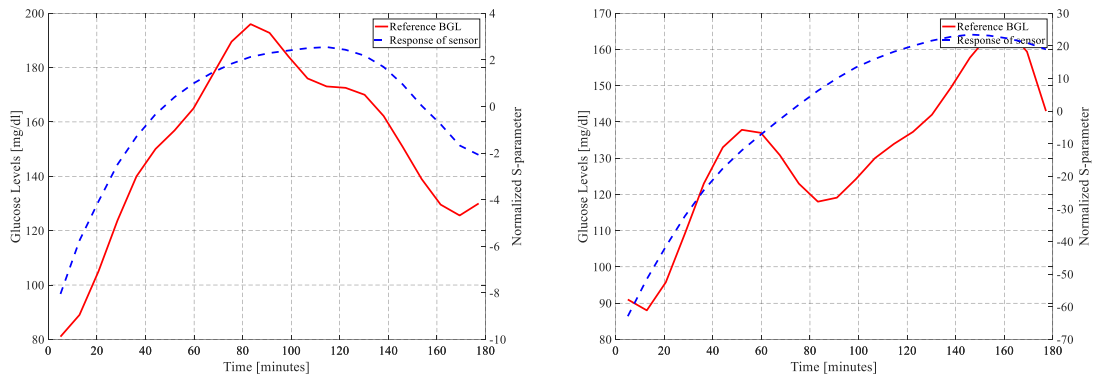
(b)

Figure 67: Correlation between the response of a. broad-band sensor, and b. octa-band sensor between two different OGTTs for the same subject and for the same frequency a) f=1.4 GHz and b) f=1.33 GHz.

7.3.4. Measurements Accuracy

In the presented experimentation, there exist several sources of error. For instance the position of the sensor might vary between the measurements. Furthermore, the data collected is always bounded to the accuracy of the underlying measurement tools both in terms of the utilized glucometer and the lab vector network analyzer.

88

7.3.4.1. Glucometer

The ACCU-CHEK Performa glucometer is a calibrated system used to measure blood glucose concentrations within the 10-600 mg/dL range [57]. However, the meter's accuracy depends upon a lot of physical and pharmacological factors in addition to the condition of the patient and the strips used. For the considered meter, the accuracy of the system is shown in Table 17.

Table 17: Accuracy of the ACCU-CHEK Performa glucometer [57].

Glucose Concentrations $< 100\ mg/dL$			Glucose Concentrations $\geq 100\ mg/dL$		
Within ± 5 mg/dL	Within ± 10 mg/dL	Within ± 15 mg/dL	Within $\pm 5\ mg/dL$	Within ± 10 mg/dL	Within $\pm 15\ mg/dL$
81.5%	97.0%	99.4%	59.3%	91.0%	99.1%

7.3.4.2. S-parameters

The accuracy of S-parameters measurements depends on the precision of the VNA, the calibration, in addition to the quality of the cables.

7.3.4.2.1. Vector Network Analyzer

Keysight FieldFox RF analyzer N9914A was used for the measurements. The S-parameter value for a given frequency may fluctuate around the correct one. We treated this as a random source of error, and to eliminate this randomness, ten readings of the signal were collected subsequently at a specific frequency. The averaged value was then considered for further analysis.

<u>7.3.4.2.2. Calibration</u>

A typical calibration will move the measurement reference planes to the very

ends of the test cables to account for the phase difference and losses in the cables.

However, when dealing with lengthy measurements as the ones presented in this work,

the quality of calibration deteriorates with time courtesy of large cables' movement and

bending. The collected data is therefore smoothed by applying a moving average filter.

7.4. Discussion

In this chapter, the previously designed RF sensors are tested using simulation

models and measurements. The responses of the proposed sensors showed good

correlation with the variations in the dielectric constant and glucose levels. The

collected data from the in-vitro and in-vivo studies will be used to develop and test

several regression models in chapter eight.

CHAPTER 8

DEVELOPMENT OF A REGRESSION MODEL

8.1. Introduction

This chapter addresses the development of a mathematical model for predicting

glucose levels from the data recorded by the proposed sensors. Particularly, several

linear and nonlinear methods are applied to the collected data to build the model. The

aim here is to assess the performance of these regression methods, and to find the best

prediction model.

8.2. Regression Analysis

Regression is the estimation of an output variable (blood glucose level in our

case) from a set of measured input variables (measured sensor device physical

parameters such as the S-parameters phase and magnitude at different frequencies). This

is performed by establishing a mathematical relation between the input and output

variables. In case of linear regression, the mathematical relation is a simple linear

equation that uses either one (univariate) or several (multivariate) explanatory variables

x to describe the behavior of the dependent variable y. For the case of k explanatory

variables, the linear function is denoted as in Eq. 31.

$$y = \beta_1 x_1 + \beta_2 x_2 + \cdots + \beta_k x_k + e(\beta_1, \ldots, \beta_k) \ (31)$$

Alternatively, assuming a sample of T observations, Eq. 31 can be expressed in

its general form as in Eq. 32. Each column of $\boldsymbol{X}$ contains T observations of an

explanatory variable x_k. $\boldsymbol{y}$ is the vector of responses, $e(\beta)$ is the vector of error terms, and β is the vector of unknown parameters to be estimated. The objective of regression is to find the most suitable values for β that minimize the resultant prediction error.

$$\boldsymbol{y} = \boldsymbol{X}\beta + e(\beta) \ (32)$$

$$\boldsymbol{y} = \begin{bmatrix} y_1 \\ y_2 \\ \vdots \\ y_T \end{bmatrix}, \qquad\qquad \boldsymbol{X} = \begin{bmatrix} x_{11} & \cdots & x_{1k} \\ \vdots & \ddots & \vdots \\ x_{T1} & \cdots & x_{Tk} \end{bmatrix}$$

For the case of ordinary least squares (OLS), the parameters are estimated by minimizing the residual sum of squares $||\boldsymbol{y} - \boldsymbol{X}\boldsymbol{\beta}||_2^2$. When the system is overdetermined and $\boldsymbol{X^T X}$ is nonsingular, and hence can be inverted, the unknown parameters vector β can then be obtained according to Eq. 33.

$$\widehat{\boldsymbol{\beta}} = (\boldsymbol{X^T X})^{-1} \boldsymbol{X^T y} \ (33)$$

For the case of glucose sensing, it is quite difficult to collect a large number of reference glucose points. Accordingly, while the number of covariates is high, the number observation points is quite low. This means that we are dealing with an undetermined system where K>>T. Consequently, OLS can't be used for prediction. To deal with this problem, sparse regression and/or feature selection methodologies are employed. We particularly focus on linear regression techniques such as partial least squares (PLS) [58], and the least absolute shrinkage and selection operator (LASSO) [59] method as well as non-linear regression methodologies such as the Gaussian processes (GP) [60]. Furthermore, dimensionality reduction methods such as principal component analysis can be employed [61].

The procedure used to develop the mathematical regression model is presented in the following. The main steps include preprocessing, dimensionality reduction processes, model generation, and model performance evaluation.

8.2.1. Preprocessing

Real measurements data may be inconsistent, incomplete, and containing measurement errors. The data preprocessing step assembles raw data and transforms it into a clear format for additional processing. Preprocessing includes multiple steps such as data collection, transformation and reduction. For purposes of measurement error, we rely on averaging and smoothing techniques to eliminate random sources of error.

In our case, measurements are performed over 201 frequencies taken over the operating regions of the sensors. These frequencies range between 0.5 GHz and 3.5 GHz for the broad-band filter, and between 1 GHz and 3 GHz for the octa-band filter. However, we noticed that neighboring frequencies have similar trends, and to eliminate redundancy, we sampled uniformly 20 frequencies over the operating ranges. This resulted in a total of 120 features corresponding to the magnitude and phase of the sensor S11, S21, S22 parameters at the different frequencies over the operating range of the device.

Sampled data is then normalized for consistency between the different feature vectors. The filter's measured data are scaled and shifted to [0 1]. This is performed for each measured physical parameter at a given frequency, by subtracting for each observation point the value of the physical parameter at that frequency from the

reference (fasting) glucose level of a specific OGTT at the same frequency. The value is then divided by the absolute maximum of the difference for all the observation points at that frequency.

8.2.2. Modeling Techniques

Several regression techniques like Partial Least Squares (PLS), Least Absolute Shrinkage and Selection Operator (LASSO) and Gaussian Processes (GP), were considered for prediction. Cross-validation methods were then employed to find the best model for purposes of prediction.

PLS aims to predict a set of dependent variables (target), from a set of independent variables (predictors). This is realized by extracting, from the predictors, a reduced set of orthogonal features while maximizing correlation with the dependent variable Y. These factors are linearly combined from the original variables, and are used for estimation [58]. A more advanced version of PLS is locally weighted PLS [62].

LASSO is a linear estimation method that uses the L_1 penalty as a regularization technique. This penalized regression process shrink the regression coefficients toward zero, introducing some bias to reduce variability. This is performed by adding a penalty term to the residual sum of squares as in Eq. 34. The tuning parameter λ controls the amount of shrinkage. Choosing the right λ is essential to minimize the error in prediction [59].

$$\hat{\beta} = argmin\{ ||y - X\beta||_2^2 + \sum_{j=1}^{P} J_\lambda |\beta_j| \}, \beta \in \mathbb{R}^P \ (34)$$

GP produces flexible, nonlinear, and nonparametric Bayesian models. Prediction using this method is probabilistic and is related to uncertainties. In contrast to traditional regression methods, GP does not regulate a unique function on the dataset, but rather produces a probabilistic distribution over a space of functions with respect to the dataset. To achieve this objective, the covariance function parameters are adjusted to maximize the likelihood of the observation points. Consider a GP function h(x), the goal is to predict its value for a random input vector x. A Gaussian process, like a Gaussian distribution, is completely specified by a mean and a covariance (kernel) function. Consequently, the predictive distribution is also Gaussian distributed with mean and variance [60].

8.2.3. Model and Features Selection

From section 8.2.1., it is obvious that we have a large number of features (120 features compared to 35-46 observations) and we have an undetermined system. Accordingly, to build a good model, we need to identify the critical features to build our model.

LASSO inherently identifies the critically features iteratively. For PLS and GP we rely respectively on feature extraction and selection methods such as the wrapper or the filter method (based on correlation significance for example. For all these methods, K-fold cross validation can be employed to identify the model, i.e., set of features (and kernel functions in case of GP) that result in the lowest error.

Feature extraction translates the features from the high-dimensional space into a lower dimensional space by a set of linear or nonlinear transformations. The most common linear feature extraction method is principal component analysis (PCA) [61].

Feature selection concentrates on selecting a small subset of features based on some predefined criteria. For this purpose, we rely on a wrapper method that identifies the next best feature for a given kernel function in case of GP. We then determine, based on cross-validation error, the minimum number of features and best kernel function that results in lowest cross-validation error and hence that determine the best model. Alternate feature selection methods include sorting the features based on their maximum correlation or maximum relevance and then performing cross-validation to find the best set of features. This is referred to as the filter method (not shown here.

8.2.4. K-fold Cross-validation

K-fold cross-validation divides the dataset D into K partitions (folds) of nearly equal size. For K iterations, K-1 folds are used to train the model, and the remaining fold is used for testing. During each iteration, the error of the testing fold is calculated. By averaging these values, the average error is used to help select the best model with minimum cross-validation error.

8.3. Results

8.3.1. Serum Measurements

The data collected from serum measurements using the rigid and flexible broad-band and octa-band filters were used for testing the different modeling techniques. Preliminary results showed that GP offers the best performance among the considered approaches. This is visualized in Fig. 68 where the estimated glucose levels are plotted versus the reference glucose levels using LW-PLS, GP and LASSO are presented. Moreover, the mean percentage error for the different modeling methods is shown in Table 18.

Table 18: Mean percentage error for the glucose levels estimated using LW-PLS, GP, and LASSO.

Sensor Type	LW-PLS	GP	LASSO
Broad-band Rigid	25.12	16.95	26.07
Broad-band Flexible	22.88	11.37	16.18
Octa-band Rigid	44.13	16.37	112.53
Octa-band Flexible	19.85	12.82	15.07
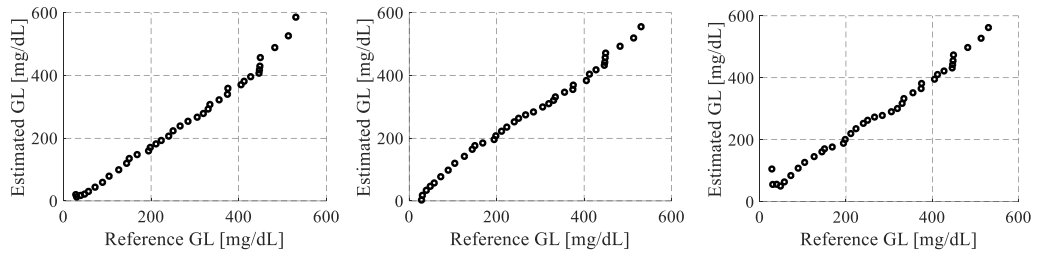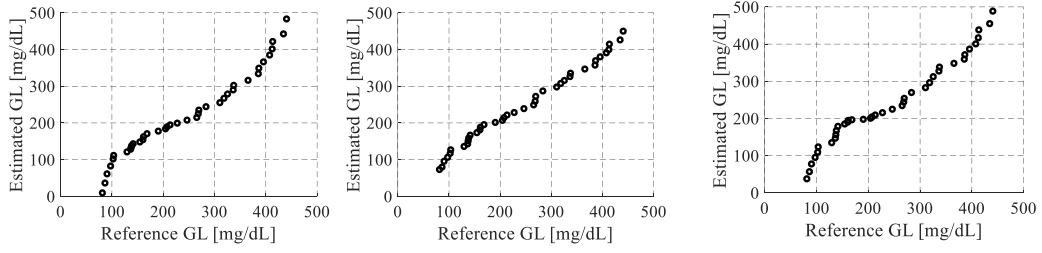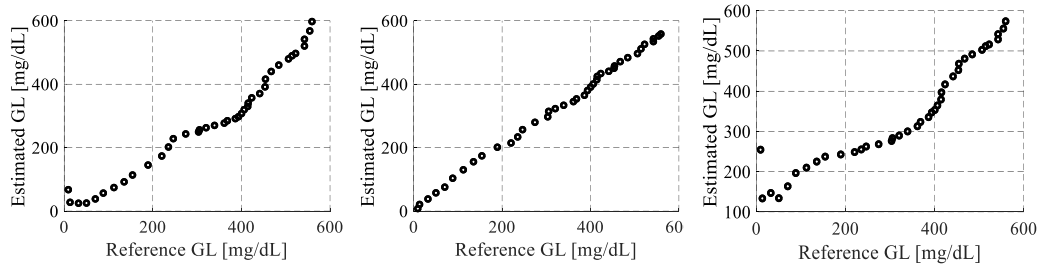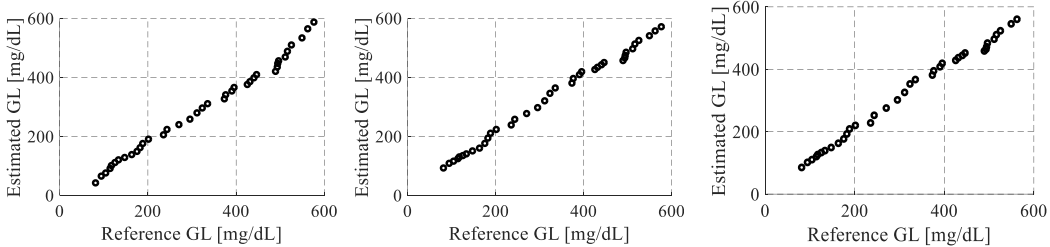
Figure 68: Estimated versus reference serum glucose levels using LW-PLS, GP and LASSO, a. rigid broad-band, b. flexible broad-band, c. rigid octa-band, and d. flexible octa-band.

8.3.2. Clinical Measurements

We developed a statistical prediction model using the sensor signals collected from in-vivo measurements during the two visits of the volunteers. The model considers the BGLs as the dependent variable. Without loss of generality in this initial implementation we do not consider the physical and physiological status of the patients. The number of observations per patient was quite small in comparison to the number of features (S-parameter magnitude and phase obtained at the different frequencies). We had a total of 23 observations per test. For the corresponding glucose levels obtained from the ACCU-Check glucometer, we have measured only 9 value points recorded corresponding to 9 out of the 23 observations. The remaining 14 reference glucose points are interpolated using cubic spline interpolation. The measured sensor data includes some fluctuations or ripples, courtesy of bending the RF cables for a long duration. The S-parameters are therefore smoothed by applying a moving average filter with a span equal to 5%.

We rely on the wrapper method and 10-fold cross-validation to determine the best features and best suitable kernel functions for a given patient in order to come up with the best model (lowest error). Five different kernel functions are considered in the simulations exponential, squared exponential, matern32, matern52, and rational quadratic. Around 8 to 15 critical features were identified for a given patient to build the model. To test the performance of the model, we randomly divide the observation points into 2/3 for training and 1/3 for testing. We report the test error for ten random data sets using the predetermined features and kernel functions. For this step, the data is initially

stratified into three homogeneous groups. This step is essential to make sure that each partition includes low, medium and high values of reference glucose levels. Following that, the data is randomly divided into two thirds (31 points) for training and one third (15) for testing. The 46 points correspond to two OGTT experiments. This step is repeated ten times to make sure that the majority of the data is used for both training and testing.

The results of the model for individual BGL profiles are shown in Fig. 69 and Fig. 70, plotted as function of time and compared with the reference blood glucose concentration. These profiles show two successive peaks corresponding to the two OGTT experiments. For each OGTT, we note a rapid increase in glucose values from the fasting level to a maximum value, and then a decrease. The solid lines are the invasively measured BGL, and the dashed lines are the estimated values using Gaussian Process; the dots correspond to the prediction using the different experiments. It is obvious that the estimated glucose concentration by the proposed sensor matches well the rate of increase and decrease of glucose concentration. It is also noted that there is no time delay between the two measurement systems. This proves that the proposed sensor directly interacts with blood. Furthermore, the mean average percentage error in prediction is noted to be 3.19% for the broad-band sensor and 1.83% for the case of the octa-band sensor.

Figure 69: BGL profiles of all the patients collected using the broad-band sensor and estimated using GP. Each plot includes the invasively measured BGL (solid lines), the estimated BGL using Gaussian Process (dashed lines) and the prediction using the different experiments (dots).
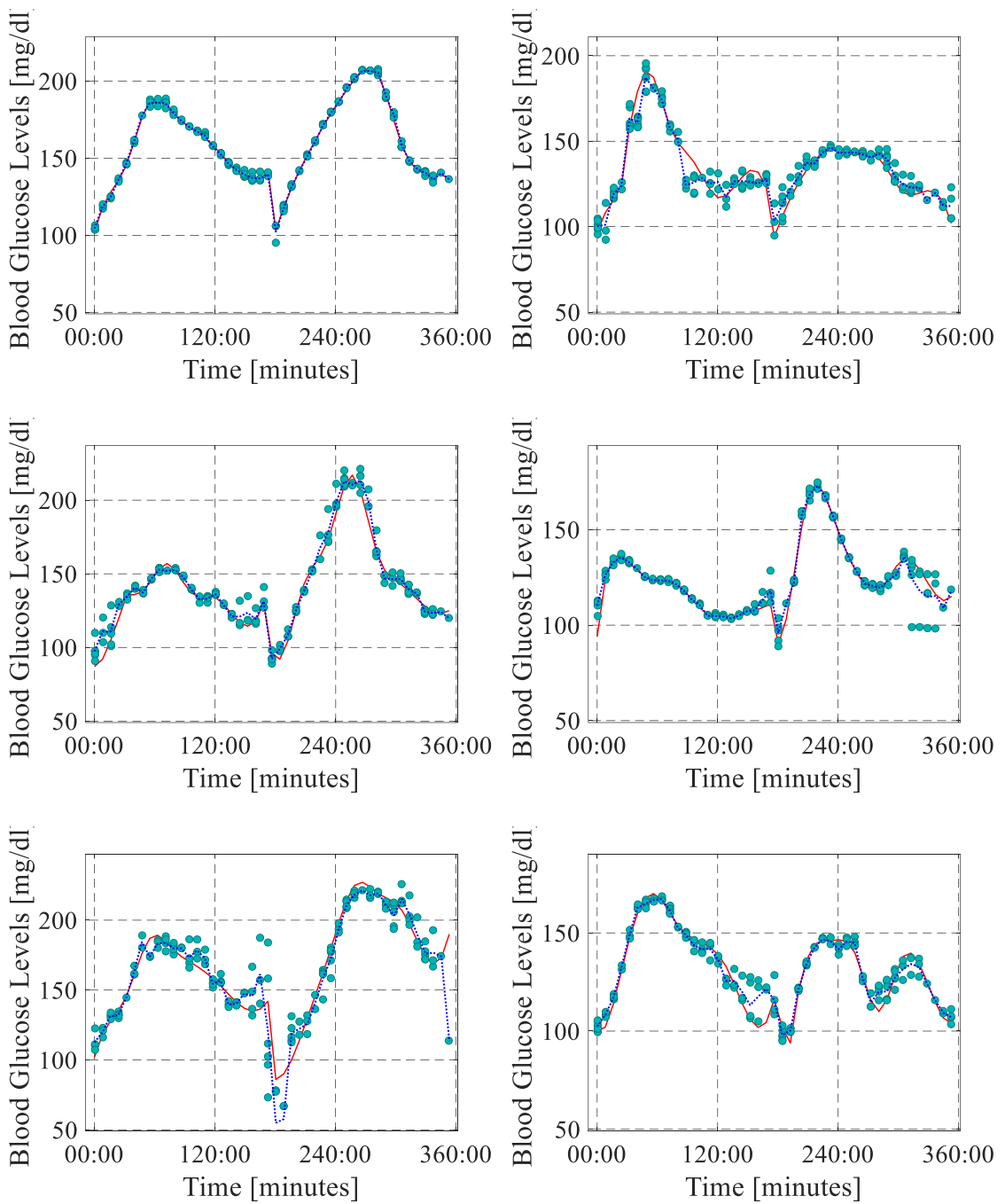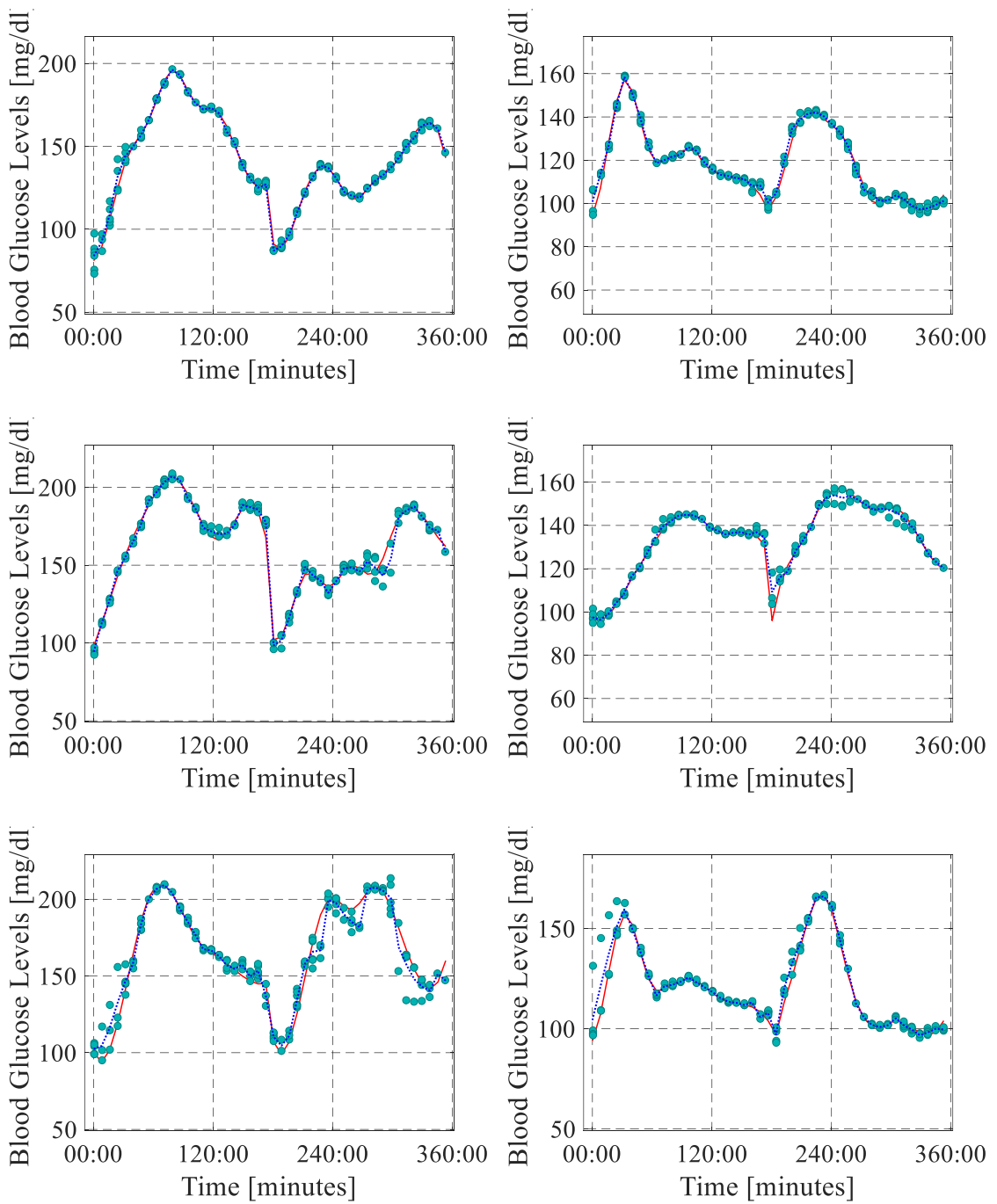
Figure 70: BGL profiles of all the patients collected using the octa-band sensor and estimated using GP. Each plot includes the invasively measured BGL (solid lines), the estimated BGL using Gaussian Process (dashed lines) and the prediction using the different experiments (dots).

To better assess the results, the Clarke Error Grid is considered [63]. This approach is used to evaluate the clinical significance of differences between a given glucose measurement technique under test (RF sensor in this case) and the intravenous blood glucose reference measurements. In this work, the reference measurements are considered to be those detected using the commercial glucometer. The Clarke Grid is a two-dimensional Cartesian illustration, where the reference values are displayed on the x-axis and the predicted values are presented on the y-axis. The points laying on the diagonal signify a perfect agreement between the reference and predicted values. The points below and above this line designate, respectively, overestimation and underestimation of the actual values. The grid is also divided into five zones. Points might lay within region A when the deviancy in the predicted values from the references doesn't exceed 20%, or when both the predicted and reference values are in the hypoglycemic range (<70 mg/dl). The values of this zone are labeled clinically exact, and are thus described by correct clinical treatment. Region B is linked to benign errors and is located around zone A. This area includes points that deviates by more than 20% from the reference values, but don't lead to inappropriate treatment. Points in region C lead to unnecessary treatment. Points in region D indicate failure in detecting hypoglycemia and or hyperglycemia (>180 mg/dl). Finally, points in region E are those that confuse the treatment of hypoglycemia for hyperglycemia or the other way around. Clinically, all the values within areas A and B are considered acceptable, whereas the values in zones C, D and E are potentially dangerous [63].

The generated Clarke grids using the data collected from the two sensors are shown in Fig. 71. For the broad-band log-periodic filter 89.5% of the data are lying in zone A and only 1.5% in zone B. For the octa-band filter, all the data are in zone A. These results show exceptional accuracy of the proposed measurement and prediction methods.
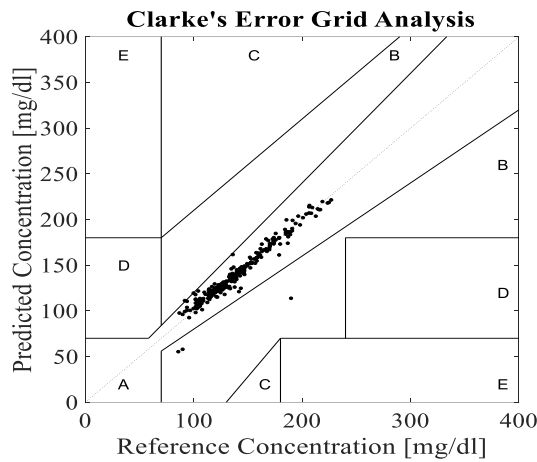
(a)
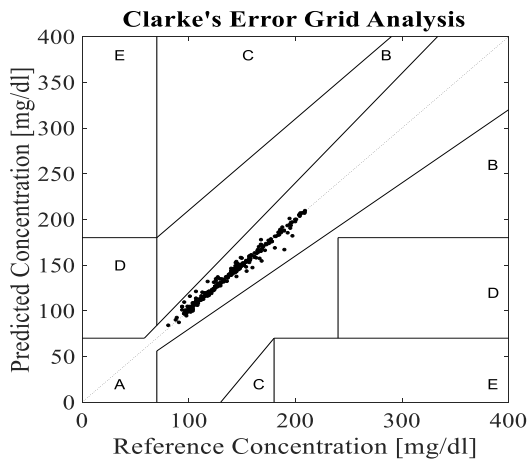
(b)

Figure 71: Clarke error grid for the data collected using a) broad-band sensor, and b) octa-band sensor.

8.4. Discussion

Several regression models were used in this chapter for estimation purposes. Gaussian process showed better abilities to predict the glucose levels, in comparison to LW-PLS and LASSO, based on in-vitro measurements. Furthermore, GP was applied on the data collected from the clinical trials. The Clarke error grid was used to assess the results. All the predicted points are clinically acceptable, proving the high sensitivity of the proposed sensors and the accuracy of GP as a modeling method.

CHAPTER 9

CONCLUSION AND FUTURE WORK

There is a need for a method of measuring blood glucose continuously and non-invasively. The ability of microwave devices to extract the electrical parameters of material accurately and without direct contact, makes them ideal for this application. In this thesis several microwave sensors are designed and tested: an SRR-based narrow band filter, a log-periodic based broad-band reject filter and a biologically inspired tunable octa-band reject filter. The behavior of the proposed RF circuits as glucose sensing systems is tested using simulation in addition to in-vitro, ex-vivo and in-vivo studies. A good correlation between the scattering parameters of proposed sensors and the variations in glucose levels is attained. Several regression models are also developed and applied on the collected data. In this context, Gaussian Processes helped achieved the lowest error in prediction. Examined results using the Clarke error grid demonstrate that for the broad-band and octa-band sensors 100% of the predicted glucose levels lay in the clinically acceptable regions.

For future work, the broad-band and reconfigurable octa-band sensors will be clinically tested on a larger number of volunteers. The regression model can also be developed further based on the newly collected data. Furthermore, a miniaturized mean to analyze the data and visualize glucose levels will be considered.

REFERENCES

[1] "WHO," 30 october 2018. [Online]. Available: http://www.who.int/mediacentre/factsheets/fs312/en/. [Accessed 29 March 2019].

[2] "Diabetes," [Online]. Available: https://www.diabetes.org.uk/Diabetes-the-basics. [Accessed 2019 March 2019].

[3] R. A. Gabbay, "New Developments in Home Glucose Monitoring: Minimizing the Pain," Canadian Journal of Diabetes, vol. 27, no. 3, pp. 271-276, 2003.

[4] U. Fischer, "Fundamentals of Glucose Sensors," Diabetic Medicine, vol. 8, no. 4, pp. 309-321, 1991.

[5] E. Wilkins and P. Atanasov, "Wilkins E, Atanasov P. Glucose monitoring: State of the art and future possibilities," Medical Engineering & Physics, vol. 18, no. 1, pp. 273-288, 1996.

[6] H. Choi, "Recent developments in minimally and truly non-invasive blood glucose monitoring techniques," in 2017 IEEE SENSORS, Glasgow, 2017.

[7] F. Barbon G. Vinci S. Lindner R. Weigel A. Koelpin "A six-port interferometer based micrometer-accuracy displacement and vibration measurement radar", IEEE MTT-S Int. Microwave Symp., 2012.

[8] S. Salman "Pulmonary edema monitoring sensor with integrated body-area network for remote medical sensing" IEEE Trans. Antennas Propag. vol. 62 no. 5 pp. 2787-2794 May 2014.

[9] H. Acikgoz and I. Turer, "A novel microwave coaxial slot antenna for liver tumor ablation", Advanced Electromagnetics, Vol. 3, No. 1, April 2014.

[10] Nikawa, Y., Michiyama, T., 'Non-invasive measurement of blood-sugar level by reflection of millimeter-waves'. Proc. Asia-Pacific Microwave Conf., 2006.

[11] Nikawa, Y., Someya, D., 'Application of millimeter waves to measure blood sugar level'. Microwave Conf., 2001. APMC 2001. Asia-Pacific, 2001, vol. 3, pp. 1303–1306.

[12] H. Cano-Garcia, P. Kosmas, I. Sotiriou, K. P. Ioannis, C. Parini, I. Gouzouasis, G. Palikara and E. Kallos, "Detection of glucose variability in saline solutions from transmission and reflection measurements using V-band waveguides," Measurement Science and Technology, vol. 26, no. 12, 2015.

[13] Siegel, P. H., L. Yoon, and V. Pikov, "Millimeter-wave non-invasive monitoring of glucose in anesthetized rats, "in Infrared, Millimeter, and Terahertz waves (IRMMWTHz), 2014 39th International Conference on, 2014, pp.1-2.

[14] H. Cano-Garcia, I. Gouzouasis, I. Sotiriou, S. Saha, G. Palikaras, P. Kosmas and E. Kallos, "Reflection and transmission measurements using 60 GHz patch antennas in the presence of animal tissue for noninvasive glucose sensing," in 2016 10th European Conference on Antennas and Propagation (EuCAP), 2016.

[15] S. Saha, H. Cano-Garcia, I. Sotiriou, O. Lipscombe, I. Gouzouasis, M. Koutsoupidou, G. Palikaras, R. Mackenzie, T. Reeve, P. Kosmas and E. Kallos, "A Glucose Sensing System Based on Transmission Measurements at Millimetre Waves using Micro strip Patch Antennas," Scientific Reports, vol. 7, no. 1, 2017.

[16] H. Choi, J. Nylon, S. Luzio, J. Beutler and A. Porch, "Design of continuous non-invasive blood glucose monitoring sensor based on a microwave split ring resonator," 2014 IEEE MTT-S International Microwave Workshop Series on RF and Wireless Technologies for Biomedical and Healthcare Applications (IMWS-Bio2014), London, 2014, pp. 1-3.

[17] H. Choi, J. Naylon, S. Luzio, J. Beutler, J. Birchall, C. Martin and A. Porch, "Design and In Vitro Interference Test of Microwave Noninvasive Blood Glucose Monitoring Sensor," in IEEE Transactions on Microwave Theory and Techniques, vol. 63, no. 10, pp. 3016-3025, Oct. 2015.

[18] H. Choi, S. Luzio, J. Beutler and A. Porch, "Microwave Noninvasive Blood Glucose Monitoring Sensor: Human Clinical Trial Results," 2017 IEEE MTT-S International Microwave Symposium (IMS), 2017.

[19] M. Sidley and J. Venkataraman, "Calibration for Real-time Noninvasive Blood Glucose Monitoring." Masters' Thesis, Department of Electrical and Microelectronic Engineering, Rochester Institute of Technology, 2013.

[20] M. Sidley and J. Venkataraman, "Feasibility of blood glucose estimation from real time monitoring," 2013 IEEE Antennas and Propagation Society International Symposium (APSURSI), Orlando, FL, 2013, pp.2055-2056.

[21] X. Xiao and Q. Li, "A Noninvasive Measurement of Blood Glucose Concentration by UWB Microwave Spectrum," in IEEE Antennas and Wireless Propagation Letters, vol. 16, pp. 1040-1043, 2017.

[22] Jean, B.R., Green, E.C., McClung, M.J.: 'A microwave frequency sensor for non-invasive blood-glucose measurement'. IEEE Sensors Appl. Symp., Atlanta, GA, 2008.

[23] Yilmaz, T., Hao, Y.: 'Electrical property characterization of blood glucose for on-body sensors'. Proc. 5th European Conf. on Antennas and Propagation (EUCAP), Bolivar, 2011, pp. 3659–3662.

[24] Schwerthoeffer, U., Weigel, R., and Kissinger D., "Highly Sensitive Microwave Resonant Near-Field Sensor for Precise Aqueous Glucose Detection in Microfluidic Medical Applications", I2MTC Proceedings, 2014.

[25] R. Baghbani, M. A. Rad and A. Pourziad, "Microwave sensor for noninvasive glucose measurements design and implementation of a novel linear," IET Wireless Sensor Systems, vol. 5, no. 2, pp. 51-57, 2015.

[26] "IEEE standard for safety levels with respect to human exposure to radio frequency electromagnetic fields, 3 kHz to 300 GHz," IEEE Std C95.1, 2005 Edition, 2005.

[27] O.G. Martinsen, S. Grimnes and H.P. Schwan, "Interface Phenomena and Dielectric Properties of Biological Tissue," in Encyclopedia of Surface and Colloid Science, Marcel Dekker, Inc., 2002, pp. 2643-2643-2652.

[28] Gabriel, C., Gabriel, S., and Corhout E. "The dielectric properties of biological tissues: I. Literature survey" Phys. Med. Biol. 41 2231–49, 1996.

[29] R. Pethig, "Dielectric properties of body tissues," Clinical Physics and Physiological Measurement, vol. 8, pp. 5-12, 1987.

[30] H.P. Schwan, "Interaction of Microwave and Radio Frequency Radiation with Biological Systems," Microwave Theory and Techniques, vol. 19, pp. 146-152, 1968.

[31] L.A. Geddes, and L.E. Baker. Principles of Applied Biomedical Instrumentation. 3rd ed. New York: Wiley, 1968.

[32] C. Furse, A. Douglas and C. H. Durney, Basic Introduction to Bioelectromagnetics. CRC Press, 2009.

[33] T. Karacolak, E. C. Moreland, and E. Topsakal, "Cole–Cole model for glucose-dependent dielectric properties of blood plasma for continuous glucose monitoring," Microwave Optical Technol. Lett., vol. 55, no. 5, pp. 1160–1164, 2013.

[34] S. Amendola, S. Milici, and G. Marrocco, "Performance of epidermal RFID dual-loop tag and on-skin retuning," IEEE Trans. Antennas Propag., vol. 63, no. 8, pp. 3672–3680, Aug. 2015.

[35] Mobashsher, A.T.; Abbosh, A.M., "Artificial Human Phantoms: Human Proxy in Testing Microwave Apparatuses That Have Electromagnetic Interaction with the Human Body," Microwave Magazine, IEEE, vol.16, no.6, pp.42, 62, July 2015.

[36] D. Pozar, Microwave Engineering, 4th ed. Hoboken, New Jersey: John Wiley & Sons, Inc., 2012.

[37] C.-S. Lee and C.-L. Yang, "Complementary split-ring resonators for measuring dielectric constants and loss tangents," IEEE Microwave Wireless Components. Letter, vol. 24, no. 8, pp. 563–565, Aug. 2014.

[38] Collin, R.E.: Foundation for Microwave Engineering, 2nd ed. McGraw-Hill, New York, 1992.

[39] Chen LF, Ong CK, Neo CP, Varadan VV, Varadan VK. Microwave electronics; measurement and materials characterization. West Sussex, England: John Wiley, 2004.

[40] He, Yusheng & Li, Chunguang. (2010). Superconducting Receiver Front-End and Its Application In Meteorological Radar. 10.5772/7189.

[41] K. Chang, Microwave Ring Circuits and Antennas, New York: John Wiley and Sons, 1996.

[42] M. S. Boybay and O. M. Ramahi, "Non-destructive thickness Measurement using quasi-static resonators," IEEE Microw. Wireless Compon. Lett., vol. 23, no. 4, pp. 217–219, Apr. 2013.

[43] C. Hsu, K. Chen, C. Lee and C. Yang, "Improved approach using multiple planar complementary split-ring resonators for accurate measurement of permittivity," 2016 IEEE MTT-S International Wireless Symposium (IWS), Shanghai, 2016, pp. 1-4.

[44] ANSYS, Inc. ANSYSS HFSS Features [Online].
 Available: http://www.ansoft.com/products/hf/hfss/new.cfm

[45] "ISO 15197:2013 In vitro diagnostic test systems -- Requirements for blood-glucose monitoring systems for self-testing in managing diabetes mellitus," International Organization for Standardization, 2013. [Online]. Available: https://www.iso.org/standard/54976.html.

[46] M. S. Boybay and O. M. Ramahi, "Material Characterization Using Complementary Split-Ring Resonators," in IEEE Transactions on Instrumentation and Measurement, vol. 61, no. 11, pp. 3039-3046, Nov. 2012.

[47] Houssam Ayad. Controle des performances des antennes par les metamateriaux. Universite de Grenoble, 2012. English.

[48] S. R. Choudhury, S. K. Parui and S. Das, "Design of a novel bandstop filter using log periodic based circular split ring slots," 2012 Students Conference on Engineering and Systems, Allahabad, Uttar Pradesh, 2012, pp. 1-4.

[49] C. Balanis, Antenna Theory and Design, 3rd ed. Hoboken, New Jersey: John Wiley & Sons, Inc., 2005, pp. 811-815.

[50] Ashraf T, Panhwar Z, Habib S, et al. Size of radial and ulnar artery in local population. J Pak Med Assoc 2010;60:817–819.

[51] C. Chen, "Design of a compact microstrip quint-band filter based on the tri-mode stub-loaded stepped-impedance resonators," IEEE Microw. Wireless Compon. Lett., vol. 22, no. 7, pp. 357–359, Jul. 2012.

[52] K. Hsu, W. Hung, and W. Tu, "Compact quint-band microstrip bandpass filter using double-layered substrate," in Proc. IEEE MTT-S, Int. Dig., Seattle, WA, USA, 2013, pp. 1–4.

[53] K. W. Hsu, J.-H. Lin, and W. H. Tu, "Compact sext-band bandpass filter with sharp rejection response," IEEE Microw. Wireless Compon. Lett., vol. 24, no. 9, pp. 593–595, Sep. 2014.

[54] J. Ai, Y. Zhang, K. D. Xu, D. Li and Y. Fan, "Miniaturized Quint-Band Bandpass Filter Based on Multi-Mode Resonator and $\lambda/4$ Resonators With Mixed Electric and Magnetic Coupling," in IEEE Microwave and Wireless Components Letters, vol. 26, no. 5, pp. 343-345, May 2016.

[55] W. H. Tu and K. W. Hsu, "Design of sext-band bandpass filter and sextaplexer using semi-lumped resonators for system in a package," IEEE Trans. Compon. Pack. Manuf. Techn., vol. 5, no. 2, pp. 265–273, Feb. 2015.

[56] Skyworks [online]. Available: http://www.skyworksinc.com/uploads/documents/SMV1705_Series_200076O.pdf

[57] Accu-Check PERFORMA [online]. Available: https://www.accu-chek.com

[58] Robins JA. Partial Least Squares Revisited. Long Range Planning. 2014 Jun;47(3):131.

[59] S. Lee, H. Lee, P. Abbeel, and A. Ng, "Efficient L1-regularized logistic regression," in proceedings of the national conference on artificial intelligence, vol. 21, no. 1, 2006, p. 401.

[60] Gaussian processes for machine learning. Cambridge, Mass: MIT Press; 2006.

[61] Abdi, Hervé and Lynne J. Williams. "Principal Component Analysis." *Encyclopedia of Biometrics* (2009).

[62] Alin A, Agostinelli C. Robust iteratively reweighted SIMPLS. Journal of Chemometrics. 2017 Mar;31(3):e2881.

[63] Clarke WL, Cox D, Gonder-Frederick LA, Carter W, Pohl SL. Evaluating clinical accuracy of systems for self-monitoring of blood glucose. Diabetes Care. 1987; 10(5):622-8.